NTNU – Trondheim
Norwegian University of
Science and Technology

Micromechanical Modelling of Strain Localization and Fracture in Aluminium

Vegard Martinsen

Master of Science in Product Design and Manufacturing
Submission date: June 2012
Supervisor: Odd Sture Hopperstad, KT
Co-supervisor: Marion Fourmeau, KT
Afaf Saai, Sintef
Stephane Dumoulin, Sintef

Norwegian University of Science and Technology
Department of Structural Engineering

Micromechanical Modelling of Strain Localization and Fracture in Aluminium

Vegard Martinsen

The Norwegian University
of Science and Technology
Trondheim 2012

Department of Structural Engineering

FAKULTY OF ENGINEERING SCIENCE AND TECHNOLOGY
NTNU – Norwegian University of Science and Technology

MASTER THESIS 2012

for

Vegard Martinsen

Micromechanical Modelling of Strain Localization and Fracture in Aluminium

Mikromekanisk modellering av tøyningslokalisering og brudd i aluminium

Aluminium alloys are used in safety components in cars. In a crash simulation, it is important to calculate how much energy that is absorbed in an aluminium component before failure occurs and how the crack propagates in the material. This problem can be studied using micro-mechanical models in which the microstructure of the material is modelled in detail. A finite element model of the material's grain structure is created based on microscopy images. The grains are modelled with elasto-plastic isoparametric elements, while grain boundaries may be modelled by cohesive elements. The task is to develop a micro-mechanical model for aluminium alloys, and then perform a parameter study to investigate the effects of the relative strength of grains and grain boundaries, grain orientation, and fracture toughness of the grains and grain boundaries. The simulations are performed with LS-DYNA.

The following activities are proposed:

- Literature study: The candidate shall carry out a literature survey on the following three topics: aluminium alloys' microstructure, crystal plasticity and cohesive elements.
- Numerical tools: The candidate shall learn how to use LS-DYNA and the numerical tools developed at SIMLab / Department of Structural Engineering and SINTEF Materials and Chemistry for micro-mechanical modelling of materials.
- Micro-mechanical model: The candidate shall establish a generic micro-mechanical finite element model for aluminium alloys consisting of grains, particles, precipitate free zones and grain boundaries.
- Numerical studies: The candidate shall perform parametric studies to examine how changes in the microstructure affect the material behaviour.
- Reporting: The candidate shall report the results of the work in the form of a scientific report.

Supervisors: Odd S. Hopperstad, Marion Fourmeau, Afaf Saai og Stephane Dumoulin.

The report should be written according to current guidelines and submitted to the Department of Structural Engineering, NTNU, by 11 June 2012.

NTNU, 16 January 2012

Odd Sture Hopperstad
Professor

Abstract

Aluminium is often treated as a homogeneous material. However, when investigated on a microscopic scale, a granular structure is observed. The mechanical properties of the constituents, together with the distribution of stresses and strains, determines the fracture toughness of the material.

The objective of this master thesis was to investigate strain localization and fracture in aluminium on a microscopic scale. Relevant literature regarding fracture mechanisms was studied in order to determine which parameters influence the fracture toughness of aluminium. The distribution of effective plastic strain together with the stress triaxiality ratio is thought to give a prediction of the initiation of ductile fracture.

A study of the microstructure of aluminium has been carried out. The aim of this study was to gain understanding of the mechanisms leading to the formation of a precipitate free zone (PFZ) near the grain boundary. Also the relation between the mechanical properties of the PFZ and the grain interior was studied. The literature study uncovered that the PFZ is expected to have a low yield stress and a high work hardening rate compared to the grain interior.

A simplified numerical model representing a heterogeneous microstructure was developed. The aim of this model was to investigate the effect of certain parameters on the distribution of stresses and strains. The yield stress and work hardening rate of the PFZ as well as the global stress triaxiality, were all variables in a parameter study. A clear tendency of strain concentration in the PFZ was observed, which is consistent with the literature. For low global stress triaxiality, the PFZ oriented at an angle with respect to the external load was found to be the most likely location for initiation of intergranular fracture. Increasing the yield stress and work hardening rate of the PFZ was found to favor transgranular fracture.

Due to long computational time, avoiding crystal plasticity analyses is of interest. Whether a material model using isotropic plasticity is able to give the same results as the crystal plasticity model has been investigated. The difference between the average effective plastic strain in the grain interior and in the PFZ was found to be lower using crystal plasticity than when using isotropic plasticity. Using crystal plasticity, the maximum effective plastic strain was found to be dependent of the crystallographic orientations of the grains. However, a more extensive study is required before conclusions regarding the consistency of the results are drawn.

Sammendrag

Aluminium blir ofte ansett for å være et homogent materiale. Når aluminium undersøkes på mikroskala-nivå, observeres imidlertid en kornstruktur. De mekaniske egenskapene til kornstrukturens bestanddeler, sammen med fordelingen av spenninger og tøyninger er med på å bestemme materialets bruddseighet.

Målet med denne masteroppgaven var å undersøke tøyningskonsentrasjon og brudd i aluminium på mikroskala-nivå. Relevant litteratur om bruddmekanismer ble studert for å fastslå hvilke mekaniske parametere som påvirker bruddseighet til aluminium. Fordelingen av plastiske tøyninger sammen med spenningstriaksialiteten antas å gi en prediksjon av duktilt brudd.

En studie av aluminiums mikrostruktur har blitt gjennomført. Målet var å avdekke hvilke mekanismer som fører til dannelsen av en utfellingsfri sone nær korngrensene. I tillegg omhandlet litteraturstudiet forholdet mellom de mekaniske egenskapene til den utfellingsfrie sonen og kjernen av kornet. Litteraturstudiet avdekket at den utfellingsfrie sonen forventes å ha en lav flytespenning og en høy fastning i forhold til kjernen av kornet.

En forenklet numerisk modell som representerer en heterogen mikrostruktur har blitt utviklet. Formålet med denne modellen var å undersøke effekten av noen utvalgte parametere på fordelingen av spenninger og tøyninger. Flytespenningen og fastningen til den utfellingsfrie sonen, samt den globale spenningstriaksialiteten var alle variabler i en parameterstudie. En klar tendens til konsentrasjon av plastisk tøyning i den utfellingsfrie sonen ble observert, hvilket samsvarer med litteraturen. Den utfellingsfrie sonen orientert i vinkel i forhold til ytre belastning, ble funnet til å være det mest sannsynlige stedet for initiering av intergranulært brudd ved lave globale spenningstriaksialiteter. Resultatene indikerer at økt flytespenning og fastning i den utfellingsfrie sonen vil favorisere transgranulært brudd.

På grunn av lang regnetid er det ønskelig å unngå analyser basert på krystallplastisitet. Det har blitt undersøkt hvorvidt en materialmodell med isotropisk plastisitet er i stand til å gi de samme resultatene som en modell med krystallplastisitet. Forskjellen mellom den gjennomsnittlige effektive plastiske tøyningen i den utfellingsfrie sonen og i kjernen av kornet var lavere ved bruk av krystallplastisitet enn ved bruk av isotropisk plastisitet. Den maksimale effektive plastiske tøyningen var avhengig av kornorienteringen ved bruk av krystallplastisitet. Før konklusjoner kan trekkes om hvorvidt resultatene oppnådd i dette arbeidet er representative, er imidlertid en mer omfattende studie påkrevet.

Preface

This master thesis was prepared in the 10^{th} semester at the Department of Structural Engineering at the Norwegian University of Science and Technology (NTNU). The work started in January of 2012 and ended in June the same year. The duration was 20 altogether weeks.

My background is from the previously mentioned department, where I have completed several courses on the Finite Element Method as well as continuum mechanics.

In accordance with the main supervisor Professor Odd Sture Hopperstad, some modification were done to the assignment.

- The finite element model will be limited to include grains and precipitate free zones near the grain boundaries. The geometry of the model will not determined based on microscopy images.
- Modelling of fracture with cohesive elements will not be carried out. However, a literature study of the cohesive element model will still be incorporated.
- A parameter study of the fracture toughness of the grains and grain boundaries will be excluded.
- A numerical study of how changes in microstructure will influence the material behavior will not be carried out. The geometry of the microstructure will be the same for all the numerical analyses.

The task was prepared by Professor Odd Sture Hopperstad at the Department of Structural Engineering and was weighted with 30 credits. I would like to thank him and the co-supervisors PhD candidate Marion Fourmeau, Dr. Afaf Saai and Dr. Stéphane Dumoulin for valuable guidance throughout the project work. Supervision was given through weekly meetings as well as additional hours when needed. In addition I would like to thank Dr. Torodd Berstad for guidance regarding LS-DYNA [1] and for providing the finite element mesh using LS-INGRID [2]. I would also like to thank co-student Sindre N. Olufsen for valuable discussions throughout the semester.

Trondheim 11.06.2012

Vegard Martinsen

Contents

List of Figures

List of Tables

Nomenclature

BCC	Body-Centered Cubic
FCC	Face-Centered Cubic
GP	Guinier-Preston
HCP	Hexagonal Closed Packed
LEFM	Linear Elastic Fracture Mechanics
LYP	Lower Yield Point
PFZ	Precipitate Free Zone
RVE	Representative Volume Element
ssss	Super saturated solid solution
TSLC	Traction-Separation Load Curve
UYP	Upper yield point
XFEM	eXtended Finite Element Method
A	Area [m^2]
a_0	The lattice constant [m]
α	The ratio between the yield stress in the PFZ and in the grain interior
$\boldsymbol{b}$	The Burgers vector [m]
β	The ratio between the work hardening rate in the PFZ and the grain interior
C_j	The concentration of alloying element j
D	The diameter of a grain [m]
D_{ij}^p	The plastic part of the strain rate tensor
$\mathrm{d}\varepsilon_{ij}^p$	The plastic strain increments

$\mathrm{d}l$	An increment of slip [m]
$\mathrm{d}s$	An increment of dislocation line [m]
$\mathrm{d}W$	The work required to move a dislocation of length $\mathrm{d}s$ an amount $\mathrm{d}l$ [Nm]
δ	The nominal separation
δ_{ij}	The Kronecker-δ
δ_n	The normal separation
δ_n^c	The critical normal separation
δ_t	The tangential separation
δ_t^c	The critical tangential separation
E	The Young's modulus [MPa]
ε_{eff}^p	The effective plastic strain
ε_L	The Lüders strain
F	The applied force per length of dislocation line [N/m]
$\boldsymbol{F}$	The vector of force components between dislocations [N]
$\bar{F}$	The mean obstacle strength [N]
f	The yield criterion [MPa]
f_a	The area fraction of grain boundary precipitates
$f(g)$	The orientation distribution function
$\bar{F}_i$	The mean obstacle strength for precipitates in size class i [N]
G	The shear modulus [Mpa]
g	The orientation of a grain
Γ	The line tension in a dislocation [N]
γ	Shear strain
Γ_0	The work of separation [Nm]
$\dot{\gamma}^\alpha$	The strain rate in slip system α
$\dot{\gamma}_0^\alpha$	The reference strain rate
γ_f	The shear strain to failure
K	The bulk modulus [MPa]

k'	The Hall-Petch constant [N/m$^{3/2}$]
k_j	The scale factor for alloying element j
L_s	The mean slip length of a dislocation
λ	The plastic multiplier
M	The Taylor factor
m	The Schmid factor
N_i	The density of particles in size class i [1/m^3]
P_1, P_2	Lattice planes
ϕ	The potential [Nm]
R	The radius of a dislocation line [m]
r_i	The mean radius of the particles in size class i [m]
r_c	The critical radius above which the particle become non-shearable [m]
R_W	The initial work hardening rate [MPa]
ρ	The dislocation density [1/m^3]
S_{ij}	The deviatoric stress tensor [MPa]
$\boldsymbol{\sigma}$	The matrix of stress components [MPa]
$\sigma*$	The stress triaxiality ratio
σ_{eq}	The von Mises equivalent stress [MPa]
σ_H	The hydrostatic stress [MPa]
σ_i	Friction stress [MPa]
σ_p	The increase in yield stress due to the hardening precipitates [MPa]
σ_{ss}	The increase in yield stress due to solid solution hardening [MPa]
σ_y	The yield stress [MPa]
$\boldsymbol{T}$	The vector of traction components [MPa]
$\boldsymbol{t}$	The tangential vector of a dislocation
t_c	The critical time step for an explicit analysis [s]
τ	Shear stress [MPa]
τ_0, τ_1, θ_1	The parameters of the Voce hardening law
τ^α	The resolved shear stress in slip system α

τ_c^α	The critical resolved shear stress in slip system α
τ_R	The resolved shear stress [MPa]
τ_y	The critical shear stress for slip in a perfect lattice [MPa]
θ	Angle [rad]
V	Volume [m^3]
v	The wave propagation velocity [m/s]
W_0	The width of the precipitate free zone

Chapter 1

Introduction

Influence of the microstructure on fracture toughness has been reported [3]. The objective of this thesis is to study how stresses and strains are distributed in the microstructure of aluminium.

The theory of crystal plasticity describes how plasticity occurs in a single crystal. A single crystal is generally anisotropic which may influence the distribution of stresses and strains in the microstructure. In chapter 2, a literature study of crystal plasticity presenting some of the micro-mechanical mechanisms responsible of plasticity will be given.

The mechanical properties of a metal are influenced by its microstructure. The microstructure of aluminium will be studied with emphasis on understanding how the mechanical properties can be manipulated. The microstructure of aluminium as well as some strengthening mechanisms are discussed in chapter 3.

Material failure by fracture may occur in a number of different ways. In chapter 4, the most important fracture mechanisms related to aluminium will be discussed. Understanding which parameters influence the fracture toughness is essential to the investigation of intergranular and transgranular fracture. Analysis of crack propagation will not be carried out. However, the cohesive element model will still be studied, as this model might be well suited for modelling fracture in aluminium. The cohesive element model will be presented in chapter 5.

A finite element model will be developed in order to investigate how the stresses and strains are distributed in a heterogeneous microstructure. Firstly, an isotropic plasticity model will be calibrated based on the findings from the literature study of the microstructure of aluminium. A parameter study will be carried out to investigate the effect of some material parameters. Then, using the same geometry, a crystal plasticity material model will be calibrated in order to its influence on the distribution of stresses and strains. The results from the simulations using the two material models will be compared. The finite element model along with a discussion of how the result apply to the competition between intergranular and transgranular fracture will be given in chapter 6.

Chapter 2

Crystal plasticity

The theory of crystal plasticity will determine the mechanical properties of each grain and make the metal anisotropic. However, if the number of grains is sufficient and the grains have random orientation, the macroscopic properties will still be isotropic. Nonetheless this effect might influence the fracture response of the material on a microscopic level and is therefore important to address.

The plastic behavior of a material is dependent on the micromechanical mechanisms. The theory of single crystal plasticity describes the mechanisms behind permanent deformations in a crystal. Deformations in a perfect crystal will be presented in section 2.2. However, perfect metallic crystals do not exist. Material faults have great influence on the plastic behavior of a metal. This chapter focuses on the physical mechanisms leading to plastic deformation and how these mechanisms are related to work hardening. Dislocation theory is discussed in section 2.3.

Although the microstructure of a metal can be manipulated such that it becomes a single crystal, commercial alloys are all polycrystals. The mechanisms responsible for plastic deformation in a single crystal are also active in a polycrystal and the material properties of a single crystal can be somehow used to predict the properties of a polycrystal. Polycrystal plasticity will be discussed in section 2.4.

This chapter is based on the book "Mechanical Metallurgy" by George E. Dieter [4] if no other reference is stated.

2.1 Lattice structure

The atoms in a metal are arranged in a crystal structure. One of the three most common crystal arrangements related to metals is the body-centered cubic (BCC) (see figure 2.1). Some examples of BCC structured metals are lithium, chromium and tungsten. They are all known as hard metals due to a number of factors including the low packing factor of the BCC structure. The packing factor is defined as the volume of atoms in a cell per volume of the cell. Another crystal structure common in metals is the face-centered cubic (FCC) (see figure 2.1). Among many other metals, aluminium, copper and gold have a

FCC crystal structure. All these metals are known as somewhat softer than the previous mentioned. The last of the three most common crystal structures is the hexagonal close packed (HCP) (see figure 2.1). Some examples of metals which have a HCP crystal structure are beryllium, magnesium and titanium. The packing factor is the same as for the FCC cell.

The main difference between FCC and HCP is the stacking sequence. The FCC structure has a cubic ABAB stacking which means that the orientation of the lattice plane is repeated every other layer. The HCP structure has a hexagonal ABCABC stacking pattern. The HCP contains three different orientations of the lattice plane.

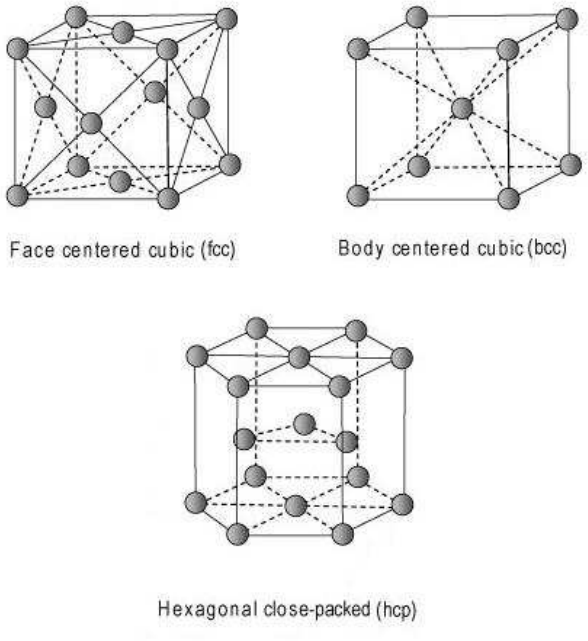

Figure 2.1: *Different crystal structures [5].*

2.2 Deformations in a perfect crystal

Deformation of a perfect crystal occurs by gliding of the atomic planes relative to each other. Figure 2.2(a) illustrates the case where all atoms in a glide plane shift at the same time.

Figure 2.2(b) illustrates a section of a crystalline structure. Only the two planes involved in the slip mechanism are shown. Prior to deformation, the crystalline structure is in its equilibrium state. When the planes move relative to each other, the distance between atom A and B will change while the distance between A and C remain constant. The resistance to slip is assumed to follow a curve close to a sinus function as illustrated in figure 2.3 [6]. The resistance against deformation will increase until the distance AB and BC are equal. At this state the attractive forces in each direction are equal and hence

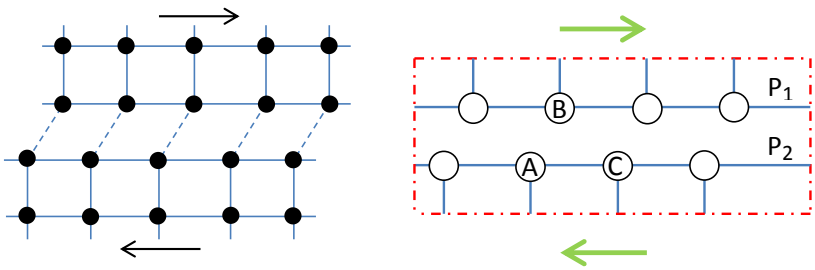

Figure 2.2: *The process of deformation in a perfect crystal.*

the resistance against slip is zero. Up until this point all the deformation is elastic. The planes will now glide until they reach a new equilibrium position where the upper plane of atoms is shifted one atom layer relative to the lower plane of atoms. The material has now been deformed plastically without the aid of any material faults. The important point is that when an external load is applied, the bindings between the atoms across the glide plane will all induce the same force resisting slip.

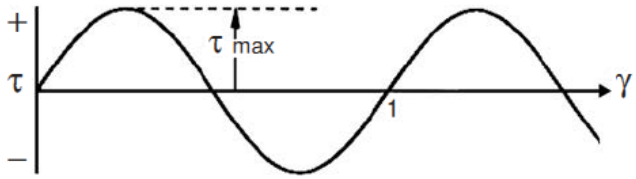

Figure 2.3: *Resistance against slip as a function of shear strain γ [6].*

The theoretical strength of a perfect crystal may be derived from continuum theory. The shape of the resistance curve can be assumed sinusoidal and given by:

$$\tau(x) = \tau_{max} sin\left(\frac{2\pi x}{a_0}\right). \tag{2.1}$$

where a_0 is the inter-atomic distance. Hook's law will apply at small strains and gives:

$$\tau = G\gamma, \tag{2.2}$$

where τ is the shear stress, G is the shear modulus and $\gamma = x/a_0$ is the shear strain.

Using the mathematical approximation given in equation (2.3) on equation (2.1), the resistance curve can be simplified (2.4).

$$\lim_{\theta \to 0} sin(\theta) = \theta \tag{2.3}$$

$$\tau(x) = \tau_{max} \frac{2\pi x}{a_0}. \tag{2.4}$$

Combination of (2.2) and (2.4) gives:

$$\tau_{max} = \frac{G}{2\pi} \tag{2.5}$$

For a commercially pure aluminium like aluminium 1050-O, the yield stress σ_y is approximately 28MPa and the shear modulus G is 26GPa [7]. The relation between the yield stress σ_y and the critical shear stress τ_y for a polycrystal is given by the Taylor factor. The Taylor factor for FCC, assuming isotropic material, is $M \approx 3.1$.

$$\tau_y = \frac{\sigma_y}{M} \tag{2.6}$$

$$\tau_y \approx 9\,MPa \tag{2.7}$$

$$\approx \frac{G}{2.9 \cdot 10^3} \tag{2.8}$$

So the yield stress observed in experiments on a polycrystal $\tau_y \approx 10^{-3}G$ is much lower than the value obtained by the presented theory ($\approx 10^{-1}G$). This supports that other mechanisms must be responsible for plastic deformation in a real crystal.

2.3 Dislocations

In this section some important mechanisms regarding crystal plasticity and dislocation theory will be explained. The same mechanisms are active both in a single and a polycrystal. Polycrystal plasticity is discussed in section 2.4.

2.3.1 Plastic deformation

In order to explain the large difference between the theoretical strength and the physical strength of a metal, the concept of dislocations was introduced. A dislocation is an irregularity in the lattice which causes local concentration of stress upon loading. Some dislocations can be visualized as an atomic plane ending abruptly in the lattice.

The process of dislocation glide is illustrated in figure 2.4. When a sufficient shear stress is applied to the crystal, the dislocation will move in the direction of slip and push the next atom plane out of its minimum energy state. This new plane now becomes the dislocated one. Only the atoms in the vicinity of the dislocation will be pushed out of their minimum energy positions. Slip by this process hence requires less energy than plastic deformation of a perfect crystal as discussed in section 2.2. The slip resistance curve have approximately the same shape as for deformation of a perfect crystal shown in figure 2.3, only the magnitude is smaller.

Plasticity is however not as straight forward as presented here due to numerous interactions between the irregularities in the lattice. Among them, the interaction between different dislocations and between dislocations and second phase particles.

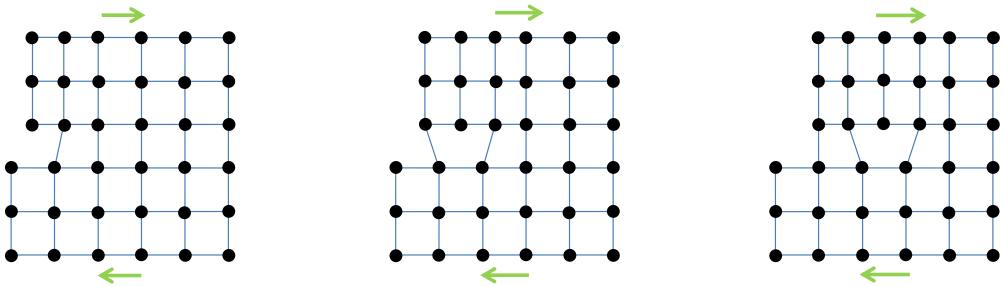

(a) (b) (c)

Figure 2.4: *Deformation process by dislocation glide. The green arrow represent the applied shear stress.*

The magnitude of slip is defined by the density of dislocations ρ and the mean slip length L_s. If the dislocations somehow are pinned which means that they are restricted against movement, the production of more dislocations is required to induce deformation of the same magnitude. This is the essence of work hardening of a metal. The subsequent sections present some processes which participate in plastic deformation of a metal.

2.3.2 Burgers vector

The Burgers vector $\boldsymbol{b}$ defines both the direction and the magnitude of slip. This vector can be found by constructing a Burgers circuit around the dislocation. The Burgers circuit is found by counting either clockwise or counter clockwise an equal amount of atomic distances in each direction starting from a random atom. When the circuit encloses a dislocation, it will not be closed (see figure 2.5). The gap in the Burgers circuit defines the Burgers vector. Consistency is important when relating the direction of the Burgers vector to the counting direction. For example, let the head of the vector be located where the counting started and the tail where it ended.

However, this definition leaves an ambiguity of the direction of the Burgers vector with respect to the dislocation line. This ambiguity is resolved by the tangent vector $\boldsymbol{t}$, which is parallel to the dislocation line. The direction of this vector is determined by weather the inserted plane is located above or below the glide plane. Dislocations with a tangential vector $\boldsymbol{t}$ pointing in a positive direction with respect to the global coordinate system is called a positive dislocations. These are often chosen to be the dislocations with inserted planes above the glide plane. Hence, dislocations with a negative vector $\boldsymbol{t}$ are the dislocation with extra inserted plane below the glide plane. The nature of a positive and a negative dislocation is equal. The definition of the vector $\boldsymbol{t}$ must therefore be used with consistency when multiple dislocations are to be considered. The vector $\boldsymbol{t}$ is important with respect to annihilation of dislocations and dislocation pile up which will be discussed later.

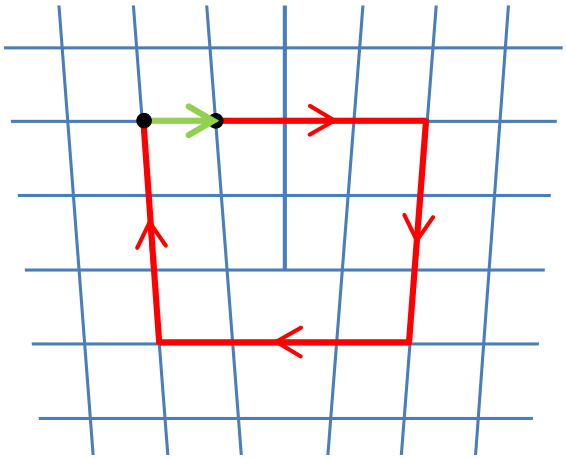

Figure 2.5: *The Burgers circuit (red line) around a dislocation and the Burgers vector (green).*

2.3.3 Two dimensional dislocations

There are mainly two different types of two dimensional dislocations. The simplest one is the edge dislocation which is essentially an extra inserted half lattice plane. The edge of the half plane is the boundary between the slipped and un-slipped part of the crystal and is called the dislocation line (see figure 2.6). The Burgers vector of an edge dislocation is perpendicular to the dislocation line and parallel to the normal of the inserted plane. This indicates that the movement of the dislocation will be perpendicular to its dislocation line. The glide plane of an edge dislocation is the plane spanned by the Burgers vector $\boldsymbol{b}$ and the tangential vector $\boldsymbol{t}$. The deformation created by an edge dislocation traveling through a crystal is equal to the relative translation of one Burgers vector of the upper half crystal compared to the lower half crystal.

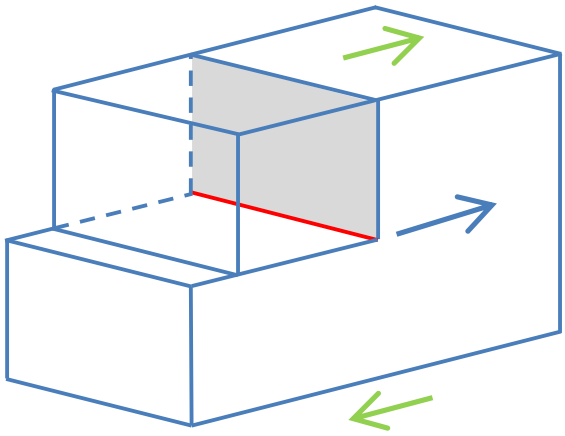

Figure 2.6: *Edge dislocation. The blue arrow represent the Burgers vector and the green arrows represent the external load. The grey area illustrated the extra inserted plane.*

The second type of dislocation is the screw dislocation. A screw dislocation is no extra inserted plane but only a cut through the lattice (see figure 2.7). The slip process zone is only a few atomic distances wide, which is important with respect to the resistance to deformation as discussed in section 2.3.1. The Burgers vector of a screw dislocation is parallel to the dislocation line. This means that slip occur by shifting the upper half of the crystal one Burgers vector relative to the lower part of the crystal in a direction parallel to the dislocation line.

The Burgers circuit of a screw dislocation forms a screw around the dislocation line, as illustrated by an orange dotted line in figure 2.7. The slip plane of a screw dislocation is not uniquely defined. All planes containing the dislocation line are possible slip planes. The slip caused by a screw and an edge dislocation are identical.

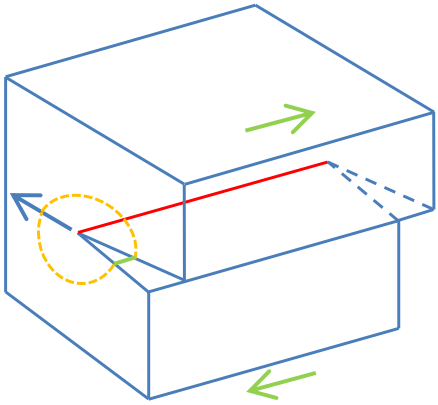

Figure 2.7: *Screw dislocation. The Burgers circuit is the orange dotted line.*

Normally a dislocation is neither a pure screw nor a pure edge, but a mix between the two. The Burgers vector does not change along a dislocation. This means that if the dislocation line is not straight the angle between the dislocation line and the Burgers vector, and hence the screw and edge component of the dislocation.

2.3.4 Forces on dislocations

The slip driving force per unit length of dislocation line F [N/m] is related to the applied shear stress τ. If τ is uniform the driving force acting on the dislocation causing slip is given by $F = \tau b$. This relation can be derived from the work required to displace a segment ds of the dislocation line by a magnitude dl in the direction of the Burgers vector b. The force in the slip direction created from the applied shear stress is τA, where A is the area of the glide plane. The global deformation is the fraction of displaced area by the total area of the glide plane, times the Burgers vector. If the dislocation had slipped all the way through the glide plane, the magnitude of the deformation would have been equal to one Burgers vector. The work required to move the dislocation by an amount dl in given in equation (2.9).

$$\mathrm{d}W = \tau A \left(\frac{\mathrm{d}s\, \mathrm{d}l}{A} \right) b. \tag{2.9}$$

The force acting on the dislocation line [N/m] will be the work divided by the slip length $\mathrm{d}l$ and the line length $\mathrm{d}s$.

$$F = \frac{\mathrm{d}W}{\mathrm{d}l\, \mathrm{d}s} = \tau b \tag{2.10}$$

An important issue related to sources of dislocation is bow out of the dislocation line between two pinning point (dislocation sources will be discussed in section 2.3.13). Figure 2.8 illustrates a segment of a dislocation line.

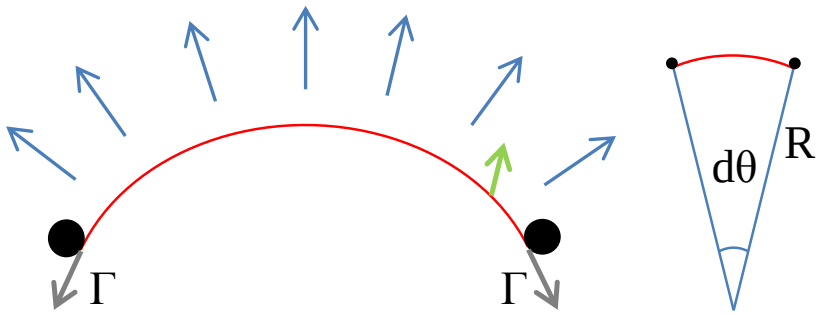

Figure 2.8: *Bow out of a dislocation between two pinning points. The green arrow illustrates the Burgers vector and the blue arrows illustrate the shear stress.* Γ *is the line tension.*

The line tension can be approximated by equation (2.11). This is the force opposing bow out, trying to keep the dislocation line as short as possible.

$$\Gamma \approx \frac{Gb^2}{2} \tag{2.11}$$

The sum of the forces in the y-direction will be:

$$\sum F_y = 0 = -2\Gamma \left(\frac{\mathrm{d}\theta}{2} \right) + \tau b (R \mathrm{d}\theta), \tag{2.12}$$

where R and $\mathrm{d}\theta$ are illustrated in figure 2.8.

The shear stress required to cause a bow out with a radius R between two pinning points can be found by solving for τ in equation (2.12).

$$\tau \approx \frac{Gb}{L}, \tag{2.13}$$

where the distance between the pinning points is L. For this relation to apply, it is assumed that the radius of the pinning points is small compared to the distance L.

2.3.5 Forces between dislocations

A dislocation will distort the lattice and create a local stress field. The stress fields of different dislocations will interact with each other and the result is attractive or repulsive forces between the dislocations.

Consider an edge dislocation, from the definition of the sign of a dislocation presented in section 2.3.2, the strain field of a positive edge dislocation will be compressive above the dislocation line and tensile below. If two dislocations of the same sign are close to each other on the same glide plane, the compressive parts of the stress fields will repel each other. The stress fields of two opposite dislocations are complementary and will cancel if located at the same place. If two dislocations of opposite sign are close, attractive forces will contribute to their annihilation which is further discussed in section 2.3.8.

The interaction between the stress fields of two dislocations was investigated by Peach *et al.* (1950) [8]. They developed a relation to describe the forces between dislocations called Peach-Koehler:

$$\boldsymbol{F} = -(\boldsymbol{\sigma} \cdot \boldsymbol{b}) \times \boldsymbol{t} \tag{2.14}$$

where $\boldsymbol{t}$ is the tangent vector of the dislocation line, $\boldsymbol{b}$ is the Burgers vector and $\boldsymbol{\sigma}$ is the stress field set up by the dislocation.

Consider the case where two edge dislocations with equal Burgers vectors are located in the vicinity of each other, as illustrated in figure 2.9. Each component of the matrix $\boldsymbol{\sigma}$ (2.15) can be found from examining the energy field around the edge dislocation (details will not be covered in this thesis).

$$\boldsymbol{\sigma} = \begin{bmatrix} \sigma_{11} & \sigma_{12} & \sigma_{13} \\ \sigma_{21} & \sigma_{22} & \sigma_{23} \\ \sigma_{31} & \sigma_{32} & \sigma_{33} \end{bmatrix} \tag{2.15}$$

As an example the Burgers vector and the tangent vector of the edge dislocations are:

$$\boldsymbol{b} = \begin{bmatrix} b_x \\ b_y \\ b_z \end{bmatrix} = \begin{bmatrix} 1 \\ 0 \\ 0 \end{bmatrix}, \qquad \boldsymbol{t} = \begin{bmatrix} t_x \\ t_y \\ t_z \end{bmatrix} = \begin{bmatrix} 0 \\ 0 \\ 1 \end{bmatrix}. \tag{2.16}$$

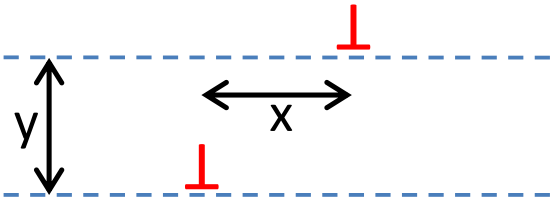

Figure 2.9: *Two equal edge dislocations located in different glide planes.*

The forces between the two edge dislocations can be found by applying the Peach-Koehler relation (2.14). The result is shown in equation (2.17) and (2.18) [9].

$$F_x = \frac{Gb^2}{2\pi(1-\nu)} \cdot \frac{x\cdot(x^2-y^2)}{(x^2+y^2)^2} \tag{2.17}$$

$$F_y = \frac{Gb^2}{2\pi(1-\nu)} \cdot \frac{y\cdot(3x^2+y^2)}{(x^2+y^2)^2} \tag{2.18}$$

Since the burgers vectors of the dislocations are equal, this force is repelling.

2.3.6 Slip systems

In a crystal structure, slip occurs on the most densely packed crystallographic planes. In a FCC structure, the family of {111} planes[1] are the glide planes. This family contain eight different planes parallel two by two (see figure 2.10). This means that a FCC cube has four unique glide planes.

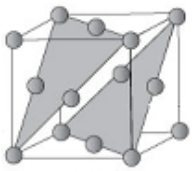

Figure 2.10: *The slip planes in a FCC cube [10].*

The direction of slip is limited to the most densely packed directions in the glide planes. In a FCC unit cell, each glide plane contains three slip directions from the family of <110> directions. The Burgers vector does not need to be parallel to the slip direction.

A slip system is a combination of a glide plane and a slip direction. In the FCC cube there are "4 glide planes · 3 slip directions = 12 slip systems" in total. Which slip system is active is determined by the direction of the external load (discussed further in section 2.3.7). Since the direction of slip is not totally random, anisotropic behavior is expected from a single crystal. How this anisotropy will influence the mechanical properties of a polycrystal will be discussed in section 2.4.

2.3.7 The Schmid factor

The Schmid factor is an useful tool to identify which slip system is critical for a given external load [11]. The slip system with the highest Schmid factor will have the highest resolved shear stress and therefore be the first to slip. By resolved shear stress is meant the shear stress at a given glide plane in a given slip direction.

In order to find the resolved shear stress, the external load have to be decomposed [4]. The angles α and β are defined in figure 2.11. The relation between the external load σ and the resolved shear stress τ_R is given in equation (2.19).

[1] Miller indices see e.g. "Mechanical Metallurgy" by G.E. Dieter [4].

$$\tau_R = \frac{F \cdot cos(\beta)}{A/cos(\alpha)} = \sigma \, cos(\alpha) \, cos(\beta), \tag{2.19}$$

where A is the area of the glide plane and F is the external load.

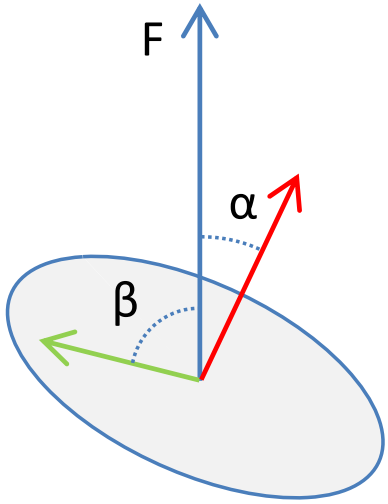

Figure 2.11: *Illustration of how the angles α and β are related to the external load F and the glide plane.*

The Schmid factor m is defined as [11]:

$$m = cos(\alpha) \, cos(\beta). \tag{2.20}$$

The angles α and β are complementary only when the external load vector is in the plane spanned by the slip direction and the normal to the glide plane.

The maximum value of the Schmid factor is reached when the external loading is in the plane spanned by the slip direction and a vector normal to the glide plane, and the plane is at an angle of 45° with the external load. This angle is known from continuum theory to be the direction of the maximum shear stress.

$$m_{max} = cos(45°) \, cos(45°) = 0.5 \tag{2.21}$$

2.3.8 Material response of a FCC single crystal

Figure 2.12 illustrates the stress-strain curve of a single FCC crystal. The crystal is loaded in a direction so that only one slip system will be active for low plastic strains.

In stage I, also called easy glide, only one slip system is active namely the one with the highest resolved shear stress. In this stage, the dislocations can move nearly without interruption and the strain hardening is therefore relatively low. A low strain hardening

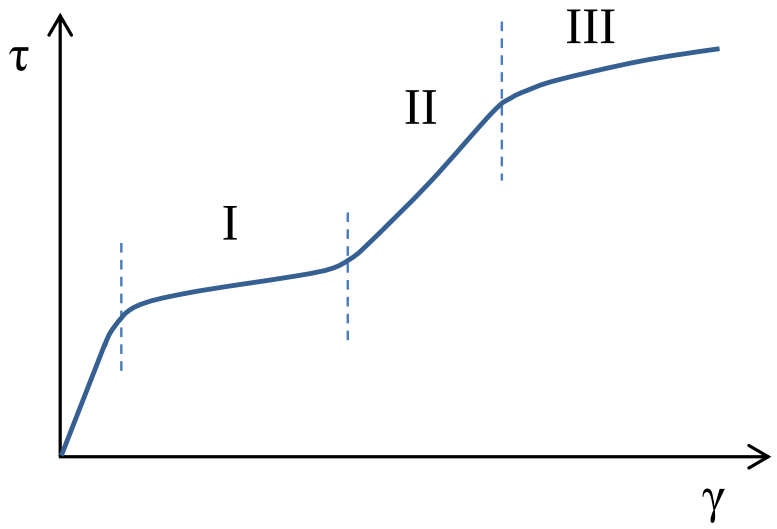

Figure 2.12: *Stress strain curve for a single FCC crystal [4].*

means that only a few new dislocations are initiated. Since only one slip system is active, intersection between dislocations moving on different glide planes are almost non-existing. Intersection of dislocations is important with respect to the hardening rate (further discussed in section 2.3.9). Stage I is both strain rate and temperature sensitive due to dependence on diffusion controlled processes such as dislocation climb (further discussed in section 2.3.11).

Eventually the resolved shear stress on other planes reach a critical value and slip occur in more than one slip system which is the case in stage II. The hardening rate in stage II is higher than in stage I. This increase is mainly due to intersection of dislocations from different slip systems which may lead to pinning. At room temperature, the hardening rate in stage II has shown to be independent of the strain rate in contrast to stage I.

In the last stage, stage III, the hardening rate will be lower than in stage II. At this strain level, the concentration of dislocations is very high. When dislocations of opposite sign meet they will cancel. Annihilation requires that the dislocations are located on the same glide plane. Although the density of dislocations is high, the probability that opposite dislocations coexist close enough in the same glide plane is rather low. Dislocations on different glide planes will therefore change glide plane by processes such as cross slip and dislocation climb in order to annihilate. Climb have to be thermally activated which lead to a thermal dependency in the rate of annihilation. Secondary, this thermal dependency effects the dislocation density. Hence the hardening rate in stage III will be temperature dependent. The transition point between stage II and III is influenced by the resistance to mechanisms such as climb and will thus also be temperature dependent.

If a FCC crystal is loaded in a direction such that more than one slip system is critical upon first slip, the shape of the stress-strain curve will be different [6] (see figure 2.13). Indeed the shape will basically be the same as for a polycrystal (further discussed in section 2.4). The mechanisms active during the hardening are a combination between

stage II and III (see figure 2.12). Note that the slope of the hardening is much steeper at first yielding when the crystal is loaded such that there are no easy glide.

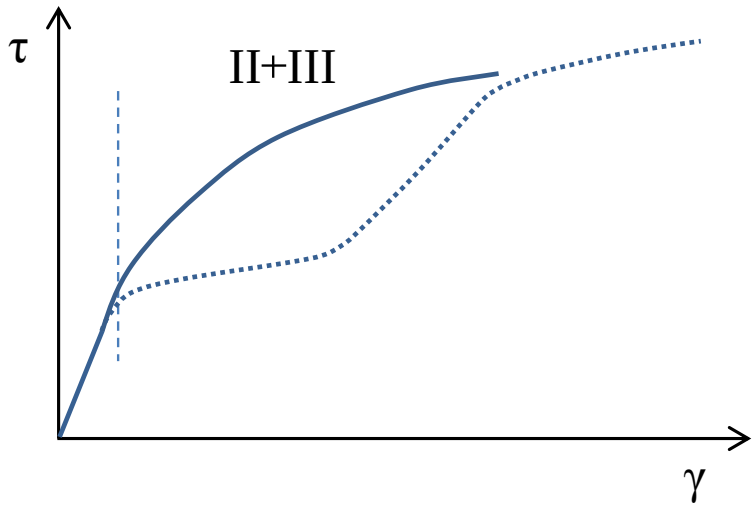

Figure 2.13: *Material response of a FCC crystal loaded such that multiple slip systems are active [6].*

2.3.9 Intersection of dislocations

Intersection of dislocations is important with respect to the plastic behavior of a material. As mentioned in section 2.3.8, intersecting dislocations will contribute to increase the hardening rate significantly. When the two dislocations A and B intersect, the dislocation line of A will be displaced by an amount and direction defined by the Burgers vector of B and vice versa (see figure 2.14).

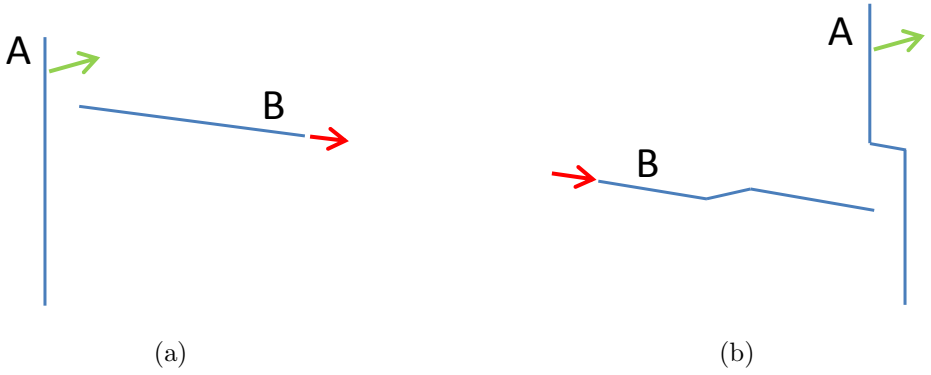

Figure 2.14: *Two orthogonal dislocations A and B (a) prior to intersection and (b) subsequent to intersection.*

The results of the cutting reactions are divided into three groups. At the point of intersection, depending on the type of dislocation and the direction of the Burgers vector, the

dislocation line will either be elongated or get a sharp step between two lattice planes. The step may either be a kink or a jog. A kink is a sharp step of the dislocation line within the glide plane and a jog is a sharp step of the dislocation line into another glide plane. Kinks are unstable since the dislocation can glide such that the dislocation line once again will be straight. Jogs are stable since "non-conservative" mechanisms must be present in order for it to annihilate. By "non-conservative" mechanisms are meant dislocation movement which cannot be replicated by normal slip along glide planes.

In figure 2.14, dislocation A gets a jog of edge character. The reason is because the step is out of its original glide plane and the Burgers vector of dislocation A is perpendicular to the dislocation line in the jog. Dislocation B gets a kink of edge character since the step is in its original glide plane and the Burgers vector is perpendicular to the dislocation line in the kink.

The kink and jog in figure 2.14 do not restrict the movement of dislocation A and B. However, this is not the case for all sharp steps along the dislocation line. Consider the intersection of two orthogonal screw dislocations. The result will be a jog of edge character as illustrated in figure 2.15. This jog can only glide in the plane spanned by the Burgers vector and the dislocation line BB', which is not possible for the screw dislocation AB and B'C'. When the segments AB and B'C' continue to glide towards DE and E'F' respectively, the jog BB' will be pinned. The only way the jog can move towards EE' is by a "non-conservative" process such as climb (further discussed in section 2.3.11). Since climb is thermally activated, the jog will be restricted against movement at lower temperatures. This will contribute to increase the hardening of the material.

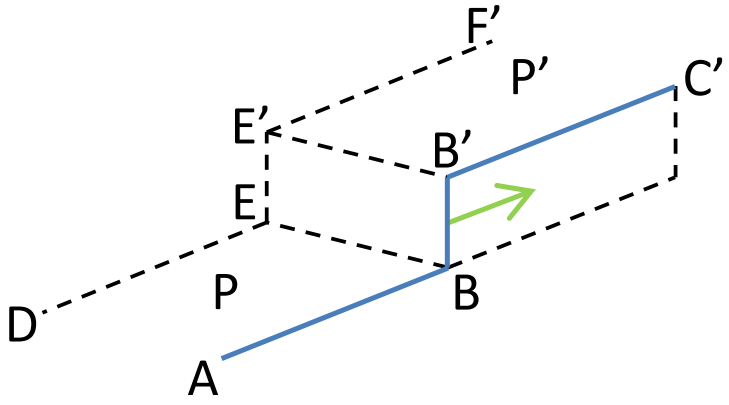

Figure 2.15: *A jog in a screw dislocation.*

2.3.10 Cross slip

As discussed earlier, the glide plane of a screw dislocation is not uniquely defined. In essence, all planes containing the Burgers vector are possible glide planes. This means that the glide plane can change at all intersections of densely packed planes parallel to the dislocation line of the screw dislocation. An edge dislocation is unable to cross slip

because its glide plane is uniquely defined by the Burgers vector and the dislocation line. However, other mechanisms will enable an edge dislocation to change glide plane. One of these mechanisms is dislocation climb which will be discussed in section 2.3.11. For a mixed dislocation, only the screw component is able to cross slip. Figure 2.16 illustrates cross slip of a dislocation. Note that both the Burgers vector and the dislocation line are parallel to the intersection of the two planes before cross slip take place.

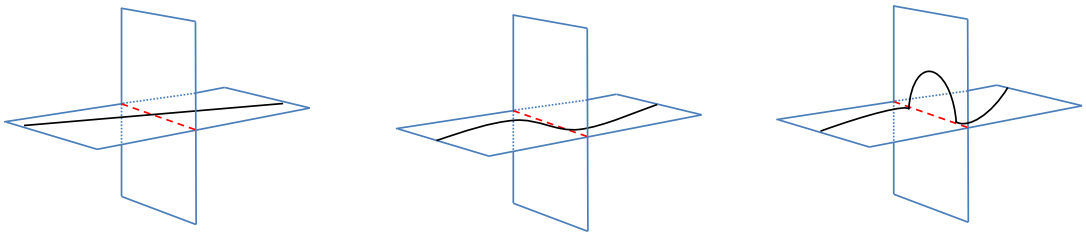

(a) (b) (c)

Figure 2.16: *The process of cross slip.*

Cross slip influences the mechanical properties of the material. The dislocations which cross slip are able to intersect dislocations on another glide planes which may contribute to work hardening. However, cross slip also enables dislocations to escape obstacles such as second phase particles (see section 2.3.12) or pile ups (see section 2.3.14). The latter will contribute to softening the material by avoiding pinning of the dislocations.

2.3.11 Dislocation climb

The mechanism of climb enables edge dislocations to change glide plane, which contribute to annihilation and to avoid pinning at particles. As discussed in section 2.3.10, a screw dislocation can slip into a new glide plane by cross slip.

Dislocation climb occurs by diffusion of vacancies. The diffusion velocity dictates the rate of the climb. Since diffusion is a thermally activated process, dislocation climb will be temperature dependent. Above a threshold temperature under which climb is impossible, the diffusion velocity tends to increase with increasing temperature. This means that climb occur more easily at high temperature. Vacancies diffuse to or away from the tip of the extra inserted half plane which makes the edge dislocation. The extent of the half plane will increase or decrease by one atom per vacancy (see figure 2.17). If an atom is subtracted from the half plane, the climb is defined as positive.

When a vacancy or a cluster of vacancies migrate to the dislocation, it will climb at small intervals along the dislocation line. After climb, the dislocation line will contain a number of jogs due to the fact that climb along the entire dislocation line at once is seldom. As discussed in section 2.3.9, a jog will not restrict the movement of the edge dislocation. Further climb will be governed by the formation and elimination of jogs along the dislocation line.

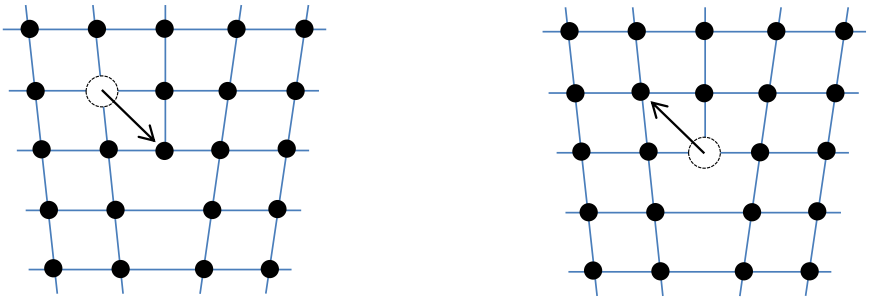

(a) Positive climb (b) Negative climb

Figure 2.17: *The difference between positive and negative climb.*

2.3.12 Shearable and non-shearable particles

The interaction between dislocations and particles is important to the mechanical properties of a metal. One of the main factors which determine the influence on the strength properties is the coherency between the particle and the surrounding matrix. Some particles consist of alloying atoms which differs in size from the atoms of the base material. The misfit of the alloying atoms induces a stress field in the crystalline lattice. When the alloying atoms group into high concentration zones, the magnitude of the stress field increase. As the zones grow, the stress field at the interface between the zone and the matrix approaches the elastic limit of the material. The crystal structure of the particles are the same as for the matrix, however the spacing between the atoms and the size of the atoms are different.

When the size of the zone is such that the stress field around it has a magnitude below the yield strength of the matrix, the zone is fully coherent with the matrix (see figure 2.18(a)). Such zones are called weak particles. When the magnitude of the stress field exceeds the elastic limit of the matrix, dislocations will be formed at the interface between the particle and the matrix to compensate for the high stresses (see figure 2.18(b)). As the particle continues to grow, the stress field will once again reach the elastic limit of the matrix and more dislocations will be initiated at the particle matrix interface. This is the process of break down of coherency. Under special treatment (discussed in section 3.1.3), this process will continue until the particle is completely non-coherent with the matrix (see figure 2.19). A fully non-coherent particle is called a strong particle.

A weak or fully coherent particle can be cut by a dislocation and will not act as a source of dislocations. The weak particle will therefore not contribute to work hardening. However, since the cutting reaction requires extra energy, the weak particles will contribute to increasing the yield stress.

As the particle become more and more non-coherent with the matrix, cutting becomes increasingly difficult. Particles which are non-coherent with the matrix cannot be cut by a dislocation since there are no continuous glide planes in the particle matrix interface. The dislocations will try to find a way to bypass these particles. If this is not possible, the dislocation may spiral around the particle which leads to formation of new dislocations

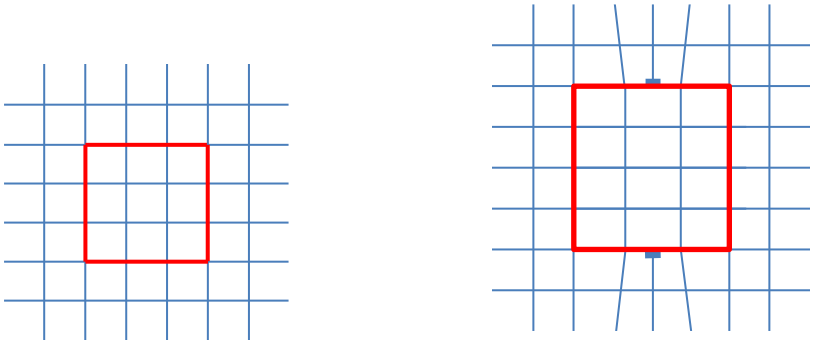

(a) (b)

Figure 2.18: *Illustrates gradual break down of coherency.*

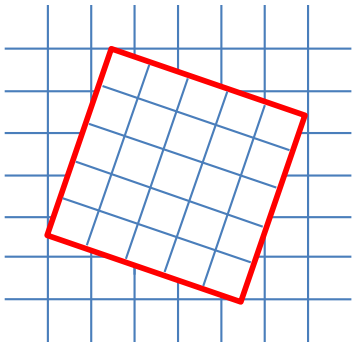

Figure 2.19: *A fully non-coherent particle.*

and hence higher work hardening (further discussed in section 2.3.13).

A model which predicts the contribution from the particles on the macroscopic yield stress of the metal was proposed by Deschamps *et al.* (1999) [12]. This model assumes that the precipitates are evenly distributed throughout the crystal and that the size of the particles have a distribution $f(r)$. It is assumed that the dislocation line has to pass all obstacles in its glide plane in order to cause macroscopic strain. In this particular formulation of the model, the precipitates are assumed to be spheres. Deschamps *et al.* argue that the increase in the macroscopic yield stress σ_p due to the hardening precipitates can be written as:

$$\sigma_p = \frac{M\bar{F}}{bL}, \tag{2.22}$$

where

- M is the Taylor factor.
- $\bar{F}$ is the mean obstacle strength.
- b is the magnitude of the Burgers vector.
- L is the average distance between precipitates along the dislocation line.

The mean obstacle strength $\bar{F}$ is the average strength of all precipitates in the material. If the size of the precipitates is divided into classes defined by particle radius r_i and the density of particles in each class is denoted N_i, the mean obstacle strength can be written as [13]:

$$\bar{F} = \frac{\sum_i N_i \bar{F}_i}{\sum_i N_i}, \tag{2.23}$$

where $\bar{F}_i$ denotes the mean obstacle strength for precipitates in size class i. For weak particles, the strength of the particle depends on the particle radius r_i in the following way [13]:

$$\bar{F}_i = 2\beta G b^2 \left(\frac{r_i}{r_c}\right), \tag{2.24}$$

where r_c is the critical radius above which the particle becomes non-shearable and β is a constant close to 1/2. For particles with radius $r_i > r_c$ the obstacle strength will be independent of the particle radius. The strength of large particles is given by [13]:

$$\bar{F}_i = 2\beta G b^2. \tag{2.25}$$

The macroscopic yield stress will be the sum of the yield stress of the pure material σ_i and the increase due to the strong and weak particles σ_p:

$$\sigma_y = \sigma_i + \sigma_p. \tag{2.26}$$

Manipulation of aluminium to get particles with certain properties will be discussed in section 3.1.3.

2.3.13 Sources of dislocations

In single crystals, the material surface is a source of dislocations. Dislocations can initiate from small steps or surface defects. The density of dislocations initiated this way is at its highest near the surface of the material. However, in polycrystalline materials the effect of nucleation of dislocations at the surface is believed to have a minor contribution. This is due to the limited number of grain in contact with the material surface. Another possible source of dislocations is by homogeneous nucleation. This requires breaking of bonds along a line in the crystalline lattice, creating two half planes. As discussed in section 2.2, the stress required to break bonds in a perfect lattice is high. However, homogeneous nucleation is still possible if a sufficient stress concentration is present. This might be the case at the interface between the matrix and a second phase particle, as discussed in section 2.3.12.

A much more common source of dislocations is the multiplication of existing dislocations. Such a mechanism was investigated by Frank *et al.* [14]. The Frank-Read source is based on a dislocation which is pinned at two points A and B (see figure 2.20). Between these points, the dislocation starts to bow out as discussed in section 2.3.4 (see figure 2.20(b)). Further stress is required until the radius of curvature of the dislocation is at its minimum. At this point the mechanism becomes unstable and the dislocation starts to spiral around the pinning points if the stress is not relaxed (see figure 2.20(c)). When the dislocation line meets itself, it annihilates. A segment of the dislocation between the two pinning points will return to original position and the rest will be a loop around the source as illustrated in figure 2.20(d). Upon further loading, the radius of the loop increases and the process is repeated.

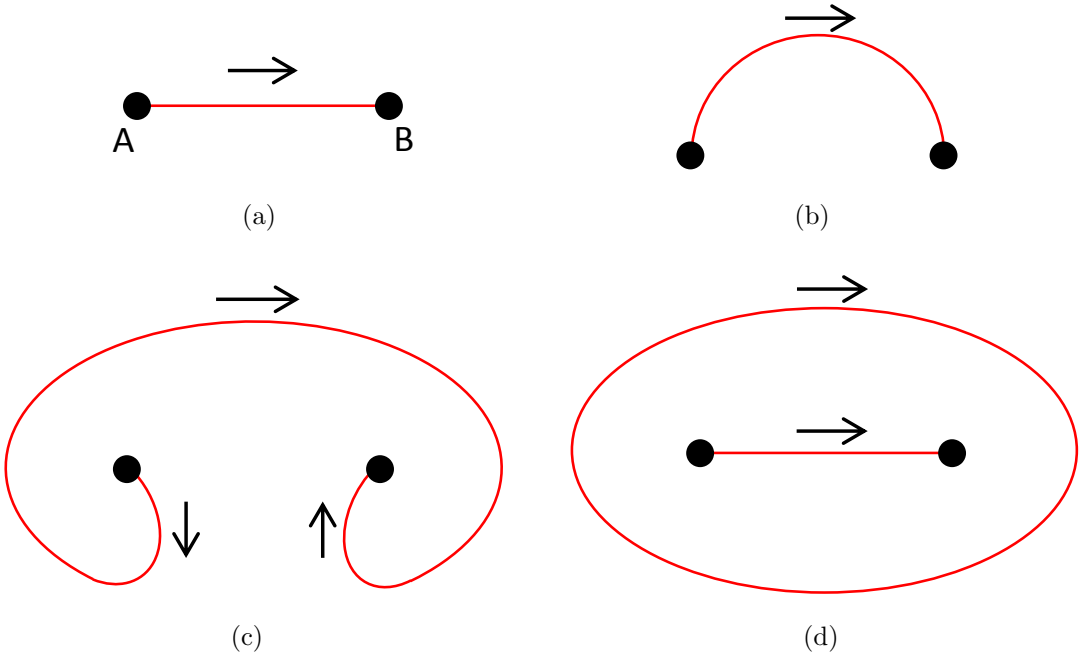

Figure 2.20: *Four stages in a Frank-Read source. The tangent vector* $\mathbf{t}$ *is illustrated by the black arrow.*

The resolved shear stress required to operate a Frank-Read source can be found using equation (2.13) for dislocation bow out between pinning points under applied shear stress. The critical configuration is when the radius of curvature of the dislocation line is at its minimum $L = 2R$. By inserting this into equation (2.13) the following is obtained:

$$\tau_{max} = \alpha \frac{Gb}{2R}, \tag{2.27}$$

where α is a constant approximately equal to unity.

The critical resolved shear stress for slip will be the sum of the friction stress τ_i required to move an un-pinned dislocation and the stress required to operate the Frank-Read source see equation (2.28).

$$\tau_c = \tau_i + \alpha \frac{Gb}{2R} \tag{2.28}$$

Pinning of dislocations will increase the required resolved shear stress for slip and be a source for new dislocations which is the essence of work hardening. When the slip length of the dislocations is limited, more dislocations are needed to produce deformation of the same magnitude. The rate of change in the dislocation density is directly linked to the slip length L_s:

$$\frac{\mathrm{d}\rho}{\mathrm{d}\gamma} = \frac{2}{bL_s}, \tag{2.29}$$

where ρ is the dislocation density and γ is the shear strain.

2.3.14 Dislocation pile up

As discussed earlier the dislocations move along certain glide planes. The free movement of the dislocations is dependent on a flawless glide plane. However, in a heterogeneous material, there are a number of obstacles and distortions of the glide planes. Such distortions might for instance be due to second phase particles or grain boundaries. The movement of the dislocations will be prohibited by these barriers which, in term, will lead to a pile up (see figure 2.21).

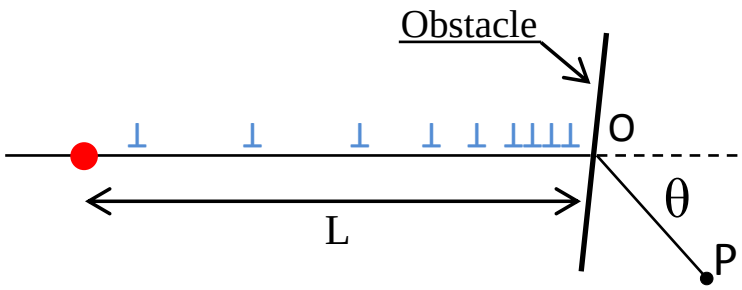

Figure 2.21: *Dislocations pile up towards an obstacle. The red dot symbolizes the source [4].*

The resolved shear stress τ_R acting on the leading dislocation in the pile up will increase with number of dislocations in the pile up. As the number of dislocations n increases, the stress field acting on the leading dislocation will eventually be sufficient to either break the barrier or for the dislocations to bypass it through e.g. cross slip. At a distance, the stress field induced by the pile up is the same as if a single dislocation with Burgers vector nb was located at a distance $3L/4$ from the dislocation source (see figure 2.21). The slip

due to the pile up is equivalent to a single dislocation traveling a distance of $3L/4$. The stress field around the pile up will interact with approaching dislocations of the same sign, making it harder for them to move. This will lead to an increased hardening of the material since again more dislocations are needed to produce the same deformation.

Stroh [15] investigated the nature of the stress field in front of a pile up. He developed the following model to describe the stress field:

$$\sigma = \frac{3}{2}\left(\frac{L}{r}\right)^{1/2} \tau_R sin\theta cos\frac{\theta}{2}, \tag{2.30}$$

where

- τ_R is the resolved shear stress acting on the leading dislocation in the pile up.
- L is the distance from the source to the barrier.
- (r, θ) is the coordinates illustrated in figure 2.21.

The model is related to the coordinate system in front of the pile up of edge dislocations as illustrated in figure 2.21. The maximum tensile stress can be found by differentiation of equation (2.30). The maximum stress σ_{max} occurs normal to a plane at an angle $\theta = 70,5°$ with the pile up slip plane.

$$\sigma_{max} = \frac{2}{\sqrt{3}}\left(\frac{L}{r}\right)^{1/2} \tau_R \tag{2.31}$$

The shear stress on the plane OP for $\theta = 70,5°$ is given by:

$$\tau = \beta\tau_R \left(\frac{L}{r}\right)^{1/2}, \tag{2.32}$$

where the parameter β is dependent on the orientation of the plane OP, but generally approximately equal to unity.

The mechanisms discussed earlier such as cross slip and dislocation climb could resolve the pile up when the stress at the tip of the pile up is sufficient. In the case where the barrier is a grain boundary the stress induced by the pile up may in term be sufficient for decohesion to occur. This can eventually lead to the formation of a crack, which will create more space for the dislocations in the pile up and the stress field will therefore be reduced.

2.4 Polycrystal plasticity

The micro-mechanical mechanisms discussed in section 2.3 are also active in a polycrystal. The mechanical properties of a polycrystal are dependent on the properties and the orientation of each crystal. The stress-strain curve of a polycrystal is similar to the one for a single crystal loaded such that more than one slip system is active (see figure 2.13). Since the crystals are all oriented differently, it is almost impossible to trigger only one slip system at a time.

A single crystal is in general anisotropic because slip occurs preferably in certain directions on certain planes. A polycrystal may still be considered isotropic due to the spread in grain orientation. However, under certain circumstances the grains can have a preferred orientation, meaning that the distribution of orientations is not random. Then, the material is said to have a texture and may be anisotropic [16]. How "sharp" the texture is can be quantified by looking at the distribution of the grain orientations. The orientation distribution function presented in section 2.4.2 is a tool frequently used for this purpose.

The reduced slip length caused by the grain boundaries is important to the yield stress of a polycrystal. Dislocations can normally not go through the grain boundaries which leads to pile ups. This causes local concentration of stresses, as discussed in section 2.3.14. The pile ups continue to grow until the stress concentration is sufficient to cause slip in an adjacent grain. The strengthening due to grain boundaries will be discussed in section 3.1.1.

2.4.1 Crystallographic texture

Large plastic deformations, induced by e.g. rolling, tend to leave the microstructure with grains oriented in certain directions compared to the rolling direction [17]. Fiber texture is one example of a texture resulting from large plastic deformations. The grains in a fiber texture are typically long and thin.

After large deformations, a lot of residual stresses remain in the material. Due to the high level of potential energy, the microstructure may recrystallize [18]. New stress free grains starts to grow when sufficient thermal energy is applied to the material. The stress free grains continue to grow until they cover the whole matrix and will eventually eliminate the residual stresses in the material. Cube texture may result from recrystallization where the grains are arranged as cubes with a crystallographic orientation parallel to the global frame [17]. However, recrystallization does not always lead to change in texture, especially when a large amount of second phase particles are present in the microstructure [19].

2.4.2 Orientation distribution function

The orientation distribution function $f(g)$ describes the level of randomness in the distribution of the crystallographic orientations of the grains:

$$f(g) = \frac{1}{dg}\frac{dV(g)}{V}, \tag{2.33}$$

where

- g denotes the orientation of a grain. This is often defined by the Euler angles which is three angles defining the orientation of a specific crystal with respect to the global coordinate system of the specimen [20].
- dg is an interval around g.
- $\frac{dV(g)}{V}$ is the volume fraction of the polycrystal which has an orientation which deviates less than dg from g.

A narrow peak in the orientation distribution function means that the grain orientations are very concentrated and the texture is sharp.

Chapter 3

The microstructure of aluminium

In this section, the microstructure of aluminium will be presented. Emphasis will be put on investigating the mechanical properties of the constituents of the microstructure as this is important with respect to the distribution of stresses and strains. Different fracture mechanisms will be discussed in chapter 4.

The microstructure of metals consists of grains. Within each grain, the orientations of the lattice planes are uniform. The process of solidification is rather complex, but essentially it initiates at impurities as a metal is cooled down from its liquid phase. When the temperature is further decreased, the grains grow from these impurities until all the material is solid. Since the atoms at the grain boundaries are not closely packed, the energy at the grain boundary is higher than in the grain interior. When a material rests at an elevated temperature, the grains will grow by absorbing smaller neighboring grains even after the material is solid [21]. The result will be a relatively uniform grain size. The mechanical properties of the metal will be influenced by the grain size which will be discussed in section 3.1.1.

The mechanical properties of aluminium can be manipulated through strengthening techniques. Some of the most common strengthening mechanisms are discussed in section 3.1. The level of homogeneity of the mechanical properties within the microstructure is important for the fracture toughness of a metal. A special attention will be given the formation of a weak zone near the grain boundary during precipitation hardening.

3.1 Strengthening mechanisms

The mechanical properties of a pure metal are rather poor for most structural commercial use. In this section, three different strengthening mechanisms will be presented namely *grain size hardening, solid solution hardening* and *precipitation hardening*. The strengthening mechanisms are closely tied to the theory or crystal plasticity.

3.1.1 Grain size hardening

A model connecting the grain size and the yield stress was developed by Hall and Petch [22]. Their model is built on the assumption that the movement of dislocations is restricted by grain boundaries due to the mismatch in the orientation of the crystallographic planes in different grains. Dislocation pile up as discussed in section 2.3.14 will form at the grain boundaries. The shear stress required for the dislocations to overcome the grain boundary barrier τ_c is given below:

$$\tau_c = n\tau_s = \frac{\pi\tau_s^2 D}{4Gb}, \tag{3.1}$$

where

- n is the number of dislocations in the pile up.
- τ_s is the resolved shear stress required for a dislocation to move past the grain boundary.
- D is the grain diameter.
- G is the shear modulus.
- b is the magnitude of the Burgers vector.

The resolved shear stress is assumed to be equal to the applied stress τ minus the friction stress preventing dislocation movement τ_i: $\tau_s = \tau - \tau_i$. When this is combined with equation (3.1) the following is obtained:

$$\begin{aligned} \tau_c &= \frac{\pi(\tau - \tau_i)^2 D}{4Gb} \\ \tau &= \tau_i + \left(\frac{\tau_c 4Gb}{\pi D}\right)^{1/2} \\ \tau &= \tau_i + kD^{-1/2} \end{aligned} \tag{3.2}$$

Equation (3.2) is simply the Hall-Petch relation expressed in terms of shear stresses [4]. The Hall-Petch relation is [22]:

$$\sigma_y = \sigma_i + k'D^{-1/2}, \tag{3.3}$$

where k' is the Hall-Petch constant.

Figure 3.1 illustrates grain boundary strengthening by showing the influence of the average grain size D on the yield stress σ_y.

As discussed in section 2.3.14, thermally activated processes will resolve the pile up effectively. The effect of grain size hardening is therefore limited [4].

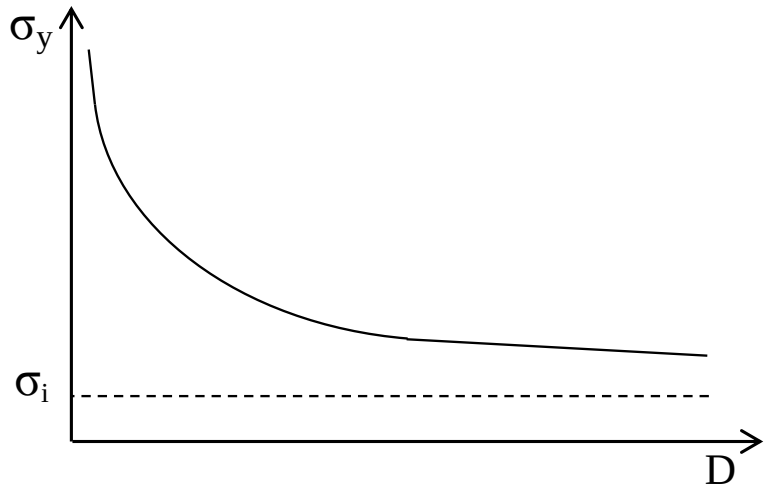

Figure 3.1: *The effect of grain size on the yield stress [4].*

3.1.2 Solid solution hardening

The process of solid solution hardening can be used to manipulate the mechanical properties of a pure metal. The base material will be added alloying elements and put through heat treatment [4]. The metal is heated to a temperature just below the eutectic temperature which enables diffusion of the solute atoms. It is important not to heat the solid solution above the eutectic temperature to avoid the formation of liquid zones, which may lead to heterogeneities in composition and microstructure during quenching.

The solute atoms will enter the lattice in one of two ways [23]. First solute atoms may enter the lattice of the base material interstitially, i.e. between the atoms of the base material. This will typically happen if the size of the solute atoms are significantly different from the atoms of the solvent. Carbon in iron is one example of an interstitial solid solution. Alternatively, the solute atoms may replace atoms of the base material or enter a vacant position in the lattice. This is called substitutional solid solution and is the most common for aluminium. The size of the solute atoms have to be approximately the same as the atoms of the base material. The crystal structure of the pure solute and the pure solvent has to be equal.

The strengthening mechanisms are related to a number of factors including the elastic stress fields introduced by the misfit of the solute atoms [4]. For an interstitially solid solution, these fields are always compressive. For a substitutional solid solution, the nature of these fields is determined by the misfit of the alloying atoms. If the solute atoms are larger than the solvent atoms, the elastic field will be compressive and tensile vice versa.

As discussed in section 2.3.5, a dislocation will induce a stress field which is partially compressive and partially tensile. The stress field of the solute atoms will interact with the field around the dislocation line and lower the elastic energy of this field. Upon further slip, the dislocation require extra external load to retain the lost elastic energy. This will contribute to increasing the yield stress of the material.

A model describing the increase in yield stress due to the solute atoms is given by equation (3.4), assuming that the contribution from each alloying element is additive [13, 24].

$$\sigma_{ss} = \sum_j k_j C_j^{2/3} \tag{3.4}$$

where the concentration of the alloying element j is denoted C_j. The factor k_j is the scale factor for alloying element j and indicates how effective the alloying element is.

The yield stress will be the sum of the contribution form the weak particles, as discussed in section 2.3.12, and the solute atoms [13].

$$\sigma_y = \sigma_i + \sigma_p + \sigma_{ss} \tag{3.5}$$

When the alloyed material rests after quenching, some of the solute atoms will migrate to a dislocation. This is due to the reduction in elastic energy of the field around the dislocation [4]. After a certain time, the originally homogeneous material with concentration C_0 of the solute atoms will consist of two zones, one still with concentration C_0 and one around the dislocations with a higher concentration C. This high concentration zone is described by Cottrell and is named Cottrell atmosphere [26]. He was investigating iron, but the same phenomenon is present in aluminium (see e.g. Kubin *et al.* [27]). The total strain energy is lower when the solute atoms are arranged in Cottrell atmospheres than if they were spread homogeneously in the material. Since the energy required to move a dislocation increases as the concentration of solute atoms increases, the required external load to initiate yielding will be higher after the formation of the Cottrell atmospheres than prior to. Upon yielding, a dislocation will feel extra resistance to slip before it has distant itself from the Cottrell atmosphere. This gives rise to some important yield point phenomenon. In this thesis, static and dynamic strain ageing will be presented.

Upon yielding, the dislocations have to fight through the high concentration zones in order to move. In material testing this phenomenon can be observed as a yield plateau. The process which results in this plateau is called static strain ageing (see e.g. Kubin *et al.* [25] and Ananthakrishna [28]). Figure 3.2 illustrates the yield plateau.

If the specimen is loaded beyond yielding and then unloaded and reloaded without time to rest, there will be no yield plateau because the solute atoms need time to diffuse in order to form new Cottrell atmospheres. To restore the yield plateau, the specimen must rest for a period of time.

At the initiation of yielding a so called Lüders band will be formed (see e.g. Ananthakrishna [28]). This band is a local zone with plastic deformation traveling along the specimen. The formation of the Lüders band will lead to relaxation in the rest of the specimen. This can be observed on the stress-strain curve in figure 3.2 as the drop in the yield stress from the upper yield point (UYP) to the lower yield point (LYP). The Lüders band will propagate over the specimen until it is has uniform strain denoted Lüders strain ε_L. When the Lüders strain is reached, the material will start to harden uniformly.

Another important yield point phenomenon is dynamic strain ageing (see e.g. Kubin *et al.* [27] and Ananthakrishna [28]). At a certain strain rate and temperature, a discon-

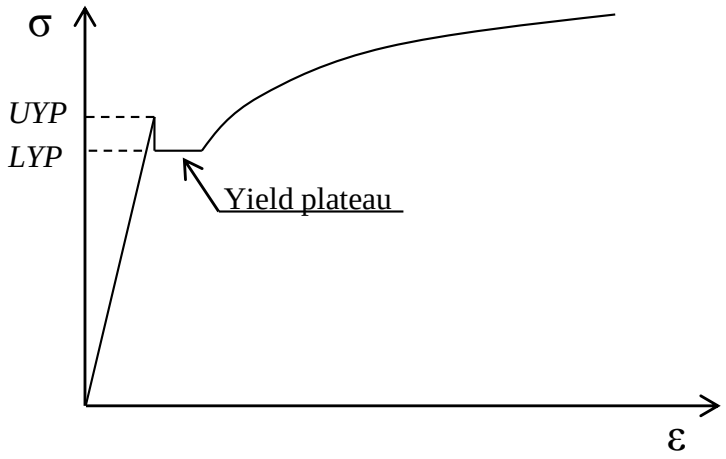

Figure 3.2: *The yield plateau resulting from static strain ageing.*

tinuous stress-strain relationship might be observed. The specimen experience repetitive relaxation as it is loaded beyond yielding. This is called serrated yielding or Portevin le Chatelier effect. A schematic illustration of serrated yielding is given in figure 3.3. After ageing the dislocations are located in zones with high concentration of solute atoms. When yielding occurs the dislocations will move out of this high concentration zones and consequently the specimen will relax because the dislocations are able to move more freely. The diffusion velocity of the solute atoms is faster than the speed of the moving dislocation which enables them to pin the dislocation after it has exited the zone packed with solute atoms.

This sequence will be repeated over, and over and will be observed as a non-smooth stress strain curve like schematically illustrated in figure 3.3. In the regions where the stress drops, a band of localized plastic strain spreads out in the specimen. This is called the Portevin le Chatelier band (see e.g. Ananthakrishna [28]). The diffusion rate will increase with increasing temperature. This implies that serrated yielding will occur only for a certain temperature interval. Figure 3.3 illustrate how the material response changes with temperature.

In low carbon steels, normal volume diffusion of solute atoms has shown to be a reasonable explanation to serrated yielding (see e.g. Dieter [4]). This means substitutional atoms diffuse through movement of vacancies and interstitial solute atoms can diffuse through the space between the solvent atoms [4]. However, in aluminium, volume diffusion is far too slow to be responsible for the Portevin le Chatelier effect [29]. The average resting time for the dislocations at an obstacle is to short for the solute atoms to be able to pin the dislocation. Some have argued that another diffusion mechanism called pipe diffusion play a role [4]. The theory of pipe diffusion basically states that the solute can move more easily along the dislocation line since the distortion of the lattice results in more free space in this region [30]. However, atomistic modelling has shown that even this diffusion mechanism is too slow [31]. The exact explanation of the diffusion mechanism is still a topic for research and discussion.

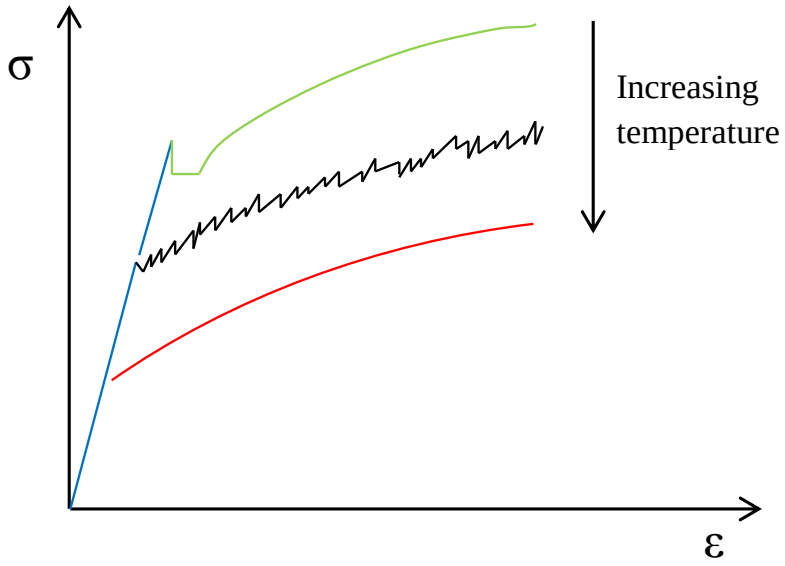

Figure 3.3: *Illustration of how the yield point phenomena are dependent on temperature [4]. The black curve illustrates serrated yielding.*

3.1.3 Precipitation hardening

Another important strengthening mechanism is precipitation hardening also called age hardening. This process consists of three main steps: *heating*, *quenching* and *ageing* [4]. The two first steps are basically similar to the process of solid solution hardening. The goal of particle hardening is to create strong and weak particles like discussed in the section 2.3.12, which will contribute to hardening by restricting the movement of dislocations.

The main difference is the solubility of the solute at room temperature. A high solubility of the solute atoms at room temperature was required for an efficient solid solution hardening process. In the process of precipitation hardening however, a super saturated solid solution (ssss) at room temperature is required [23]. A large decrease in the solubility from the eutectic temperature to room temperature is favorable. The phase diagram for aluminium-copper is given in figure 3.4. The maximum solubility of copper is about 5.7% at eutectic temperature. The phase diagram illustrates that a $5.7wt\%$ aluminium-copper alloy will consist of pure aluminium FCC plus intermetallic zones with Al_2Cu at room temperature. In other words solid solution of this weight percentage Al-Cu is super saturated at room temperature.

The instability of the super saturated solution is the key to particle hardening. The energy state of the solute atoms in solid solution is not at its minimum, which will lead to transformations in the crystalline lattice. The transformation process happens through ageing. For some alloys, ageing can even happen when the material rests at room temperature. This is called natural ageing [4]. Other alloys remains in the super saturated solid solution state at room temperature due to high activation energy for the precipitation process, and will require additional heat treatment to form particles.

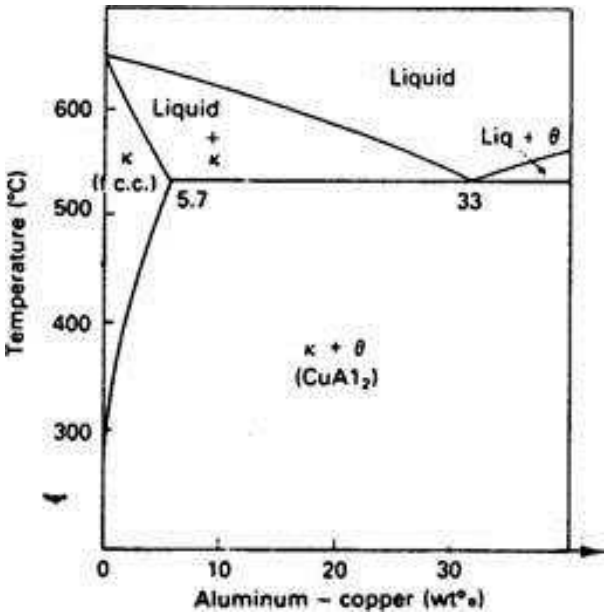

Figure 3.4: *Phase diagram for aluminium-copper alloys [32].*

This is called artificial ageing. Even if the ageing mechanisms will be active at room temperature, heat is normally applied in order to speed up the process. As a general rule, a fast quenching rate will contribute to accelerating the subsequent ageing, due to the large amount of vacancies preserved in the crystalline lattice. The diffusion of substitutional solute atoms requires the presence of vacancies, as mentioned in section 3.1.2.

During the process of ageing, the microstructure of the alloy goes through a sequence of precipitation stages. Normally, the material is metastable at each stage due to the activation energy required to drive the precipitation reactions. The metastable stages explained below are related to ageing of an aluminium-copper alloy. This alloy has a relatively complicated precipitation process and is therefore used as an example.

The first precipitates which are formed are the Guinier-Preston (GP) zones or in the case of Al-Cu alloys also called GP-I zones (see e.g. Morris [33]). These are zones where the solute atoms group to form a thin layer, one or two atom layers thick and 20 to 30 atoms wide. Within these zones, the concentration of solute atoms is higher than in the matrix. The difference in size of the solute and the solvent atoms will result in elastic stress fields around the GP-I zones. These stress fields will interact with the dislocations as discussed in section 2.3.12. The GP-I zone will act as a weak particle when it comes to being cut by a dislocation, and the yield stress will therefore increase. The lattice of the GP-I zones are fully coherent with the matrix.

In the next stage, the GP-I zones acts as nucleation sites for larger, but still coherent zones of the solute copper atoms (see e.g. Morris [33]). These zones are called GP-II zones and often denoted θ''. The GP-II zones are also normally fully coherent with the crystalline lattice of the matrix and can therefore not be called second phase particles [23]. The average composition of the GP-II zones is different from GP-I zones, which

manifests that they are not just large GP-I zones. The elastic field around these zones is stronger than for the GP-I zones and the yield stress of the material is therefore further increased.

In the third metastable stage, the precipitates consist of platelets [4]. These platelets are normally coherent with the matrix. However break down of coherency start to occur. At this stage, often denoted θ', the stress field approaches the elastic limit of the material at the boundary of the precipitates. Dislocations start to from at the boundary due to the magnitude of the stress field induced from the misfit of the solute atoms. As the precipitates get more non-coherent with the matrix, they act as strong particles, as discussed in section 2.3.12.

The last stage in the precipitation process is the equilibrium stage [4]. At this stage, the precipitates are completely non-coherent with the matrix. These particles are strong particles often denoted θ-particles. Further ageing will increase the size of the particles, reducing the yield stress.

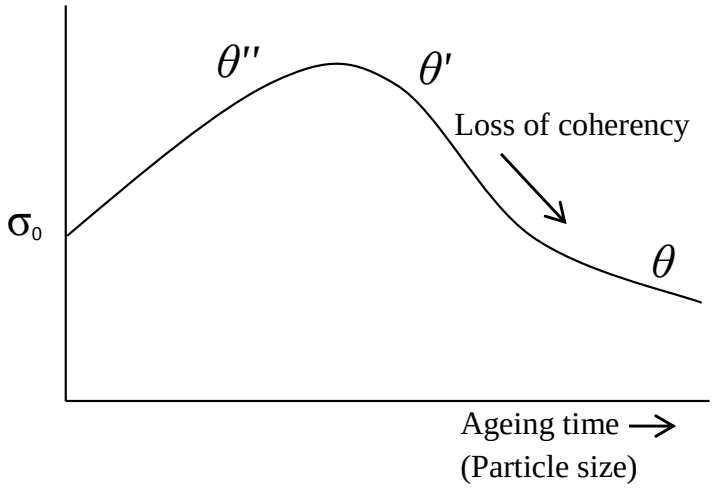

Figure 3.5: *Illustration of the yield stress evolution during the precipitation process [4].*

As indicated in figure 3.5, when the material has maximum strength, both precipitates in the θ'' and the θ' stage are present.

The precipitation process for Al-Cu is quite complex. For other alloys this process may be simpler if they have less metastable stages before reaching the equilibrium phase. However, the general mechanism of the formation of small coherent particles and subsequent formation of larger non-coherent particles is quite common [4].

3.1.4 Precipitate free zone

Strength contribution from the precipitates is significant. Ideally, the distribution of precipitates should be uniform in order to avoid concentration of stresses and strains. In some cases, the distribution of precipitates is not uniform and the vicinity of the grain

boundaries can have very low precipitate concentration. This is called the precipitate free zone (PFZ). Two important mechanisms which leads to the formation of the PFZ will be presented here.

The mismatch in the orientation of the lattice planes in different grains may lead to locally low density of solvent atoms at the grain boundary. For this reason, solute atoms tend to migrate to the grain boundary and form large precipitates or second phase particles [34]. This migration will deplete the vicinity of the grain boundary of solute atoms.

When the quenching rate is slow, the vacancies in the vicinity of the grain boundary tend to migrate to the grain boundary, which also result in a PFZ. In most aluminium alloys, the solute atoms are substitutional. As mentioned earlier, diffusion of substitutional atoms require the presence of vacancies and will therefore be prohibited in the volume surrounding the grain boundary. If this process is dominant, the zone around the grain boundary may be highly supersaturated with solute atoms [34]. Figure 3.6 is an image of a precipitate free zone.

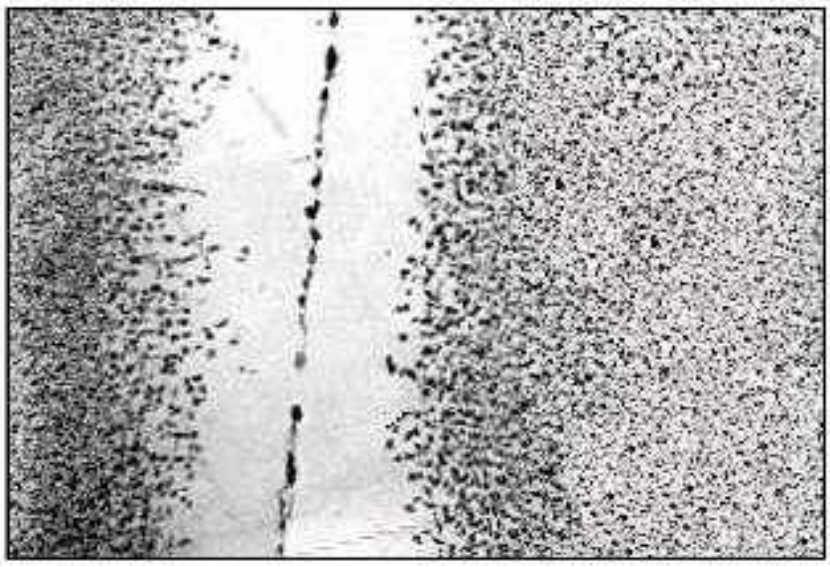

Figure 3.6: *An image of the precipitate free zone. Darker colors are the precipitates and lighter areas are precipitate free [23].*

The width and the properties of the precipitate free zone influence the fracture behavior of aluminium [35, 36, 3]. One of the most important factors that determines the width of the PFZ is the overall concentration of vacancies [23]. If the concentration of vacancies is high the PFZ will be narrow. The concentration of vacancies preserved in the vicinity of the grain boundary is strongly dependent on the quenching rate. When the quenching rate is high the vacancies are locked in the crystalline lattice and unable to migrate to the grain boundary. A high quenching rate will therefore result in a narrow PFZ. The ageing temperature will also influence the width of the PFZ as the concentration of vacancies needed for nucleation of precipitates is reduced at lower temperatures. The reason for the reduction might be that when the ageing temperature is low, the ageing time is high and the required diffusion velocity for nucleation of precipitates is reduced. Also, the solution heating temperature influences the width of the PFZ [23]. A high solution

heating temperature results in a narrow PFZ. This might be because a higher solution heating temperature preserves a higher concentration of vacancies.

The mechanical properties of the PFZ are different from the grain interior. The yield stress of the PFZ is lower than in the grain interior [37]. The yield stress is effected by a number of factors including the presence of coherent particles as discussed in section 2.3.12. Hornbogen *et al.* (1977) [36] suggested that in alloys which formed large grain boundary precipitates from depleting the vicinity of the grain boundary of solute atoms, the yield stress and the work hardening rate of the PFZ will be closer to pure aluminium than to the grain interior. They also argue that the strain concentration at the PFZ will increase as the difference between the yield stresses in the PFZ and grain interior increase.

Precipitates will lower the work hardening rate in the grain interior [37, 38]. If the ageing process is such that the PFZ is a highly super saturated solid solution, the hardening rate in this zone may be higher than for a pure aluminium [38].

Abe *et al.* (1973) [39] suggested a model for the relationship between the hardening in the early stage of deformation and the width of the PFZ (see equation (3.6)). They found that for a narrow PFZ, the initial work hardening rate of the material is higher. At the early stage of deformation, the plastic strain was found to be localized in the PFZ. Hence the PFZ was responsible for the high work hardening rate.

$$R_W = aW_0^{-1} + b \tag{3.6}$$

where

- a and b are constants.
- W_0 is the PFZ width.
- R_W is the initial work hardening rate, i.e. before extensive plasticity within the grain interior.

They explain the initially high work hardening rate by the dislocation slip length in the PFZ. As the width of the PFZ decreases, the slip length decreases due to dislocation pile up towards the PFZ matrix interface. The stress to resolve a pile up is related to the initiation of cross slip. As discussed in section 2.3.13, when the slip length decreases more dislocations are required to produce the same deformation hence higher work hardening. However, the number of dislocations in this pile up is believed to be relatively constant as the leading dislocation in the pile up will escape when the stress is sufficient. This might indicate that the work hardening in the PFZ will be quickly saturated.

Chapter 4

Fracture mechanisms

In this section the fracture mechanisms most relevant to aluminium will be discussed. Three of the most common fracture mechanisms in metals are: *ductile fracture*, *cleavage* and *intergranular fracture*. In aluminium, ductile fracture may happen both intergranular and transgranular.

4.1 Ductile fracture

4.1.1 Stress triaxiality

Ductile fracture happen through growth and coalescence of voids [40]. A material without voids will not experience plasticity under hydrostatic stresses due to the law of conservation of volume. However, when a material containing voids is subjected to hydrostatic stresses, large plastic strain may take place.

In a finite element simulation using the von Mises yield criterion, material faults are not taken into account and plasticity is only dependent on the deviatoric part of the stress tensor [41]. In order to determine whether the material is likely to fail by ductile fracture, the hydrostatic stress must be taken into account [40]. The stress triaxiality factor is the ratio between the hydrostatic and the deviatoric part of the stress tensor. The stress triaxiality together with the effective plastic strain will therefore give a prediction of how susceptible the material is to void growth (see section 4.1.2).

The stress tensor is symmetric and given by:

$$\sigma_{ij} = \begin{bmatrix} \sigma_{11} & \sigma_{12} & \sigma_{13} \\ \sigma_{12} & \sigma_{22} & \sigma_{23} \\ \sigma_{13} & \sigma_{23} & \sigma_{33} \end{bmatrix} \tag{4.1}$$

The deviatoric stress tensor S_{ij} is given by [41]:

$$S_{ij} = \sigma_{ij} - \frac{\sigma_{kk}}{3}\delta_{ij} \tag{4.2}$$

The term $\frac{\sigma_{kk}}{3}$ in (4.2) is the hydrostatic part of the stress tensor:

$$\frac{\sigma_{kk}}{3} = \sigma_H = \frac{\sigma_{11} + \sigma_{22} + \sigma_{33}}{3}. \tag{4.3}$$

The Kronecker-δ, δ_{ij} is defined as:

$$\delta_{ij} = \begin{cases} 1 & \text{if } i = j \\ 0 & \text{else} \end{cases} \tag{4.4}$$

The second invariant of the deviatoric stress tensor is given as [41]:

$$J_2 = \frac{1}{2} S_{ij} S_{ij} \tag{4.5}$$

The von Mises equivalent stress is is related to the second invariant by [41]:

$$\sigma_{eq} = \sqrt{3J_2} \tag{4.6}$$

$$\sigma_{eq} = \frac{1}{\sqrt{2}} \left[(\sigma_{11} - \sigma_{22})^2 + (\sigma_{11} - \sigma_{33})^2 + (\sigma_{22} - \sigma_{33})^2 + 6(\sigma_{12}^2 + \sigma_{23}^2 + \sigma_{13}^2) \right]^{1/2} \tag{4.7}$$

The stress triaxiality ratio is defined as the ratio between the hydrostatic stress and the von Mises equivalent stress [41]:

$$\sigma* = \frac{\sigma_H}{\sigma_{eq}} \tag{4.8}$$

The von Mises equivalent stress is directly linked to the plastic strain through the associated flow rule [41]:

$$d\varepsilon_{ij}^p = d\lambda \frac{\partial f}{\partial \sigma_{ij}} \tag{4.9}$$

where $f = \sigma_{eq} - \sigma_0 = 0$ is the yield criterion and $d\lambda$ is the plastic multiplier.

4.1.2 Void growth and coalescence

As mentioned earlier, ductile fracture in metals happen through the formation, growth, and coalescence of voids. Large plastic deformations take place, dissipating a lot of energy. Voids can nucleate from inclusions, second phase particles or other material faults [40]. The growth and coalescence of voids in front of a crack tip is illustrated in figure 4.1.

Numerous models are proposed for the formation of a void, one which is widely recognized is the continuum model proposed by Argon *et al.* [42]. This model only considers void formation by separation in the particle matrix interface. It applies to particles with a size $r > 1\mu m$. Argon *et al.* suggested that the formation of a void is dependent on both the deviatoric and the hydrostatic stress. The critical stress, the decohesion stress, is the stress required for the nucleation of a void. The decohesion stress is given next.

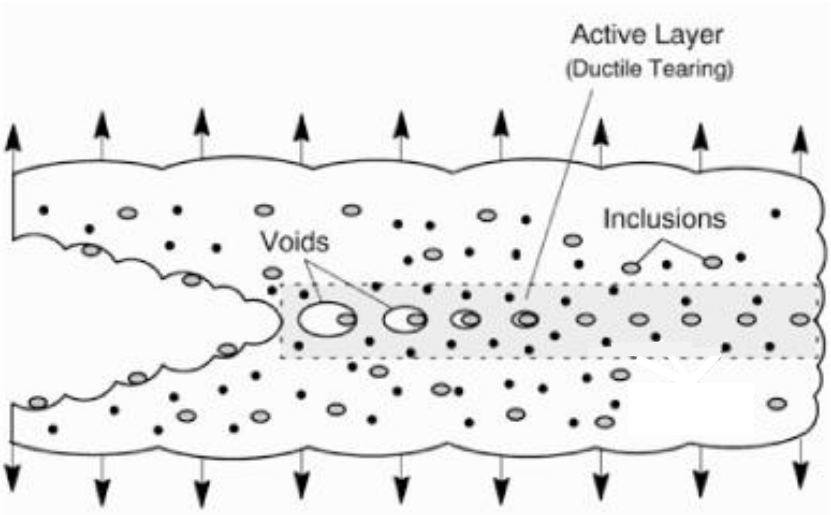

Figure 4.1: *The process of ductile fracture [43].*

$$\sigma_c = \sigma_{eq} + \sigma_H \tag{4.10}$$

where σ_{eq} is the von Mises equivalent stress and σ_H is the hydrostatic stress defined in equation (4.7) and (4.3) respectively. Note that the hydrostatic stress has the same influence as the deviatoric stress.

The nucleation strain decreases as the stress triaxiality ratio increase, which means that when a material is subjected to a high tensile hydrostatic stress it is more susceptible to void growth. This also implies that for negative stress triaxiality ratio, void growth is suppressed. This is consistent with observations from physical experiments [40].

Further, this model suggests that the decohesion stress is independent of the size of the second phase particle which later has been shown not to be physical. That is, the critical stress for nucleation of voids decrease as the size of the particle increase [44]. Research which suggests that the yield stress of the material as well as the direction of the loading influence the critical nucleation stress was carried out for steels by Beremin *et al.* [45].

Another approach developed for sub-micron particles ($r < 1\mu$m) was proposed by Goods *et al.* [46]. This model states that the critical stress for void nucleation is dependent on the maximum principal stress and the elevated stress at the interface of the particle induced by the dislocations piling up in this region.

$$\sigma_c = \sigma_1 + \Delta\sigma_d \tag{4.11}$$

where

$$\Delta\sigma_d = 5.4\alpha\nu\sqrt{\frac{\varepsilon_1 b}{r}} \tag{4.12}$$

Subsequent to void nucleation is growth and coalescence of the voids [40]. When the voids are small and represent a low volume fraction of the material they grow without

any major interaction. Void growth is driven by increased hydrostatic stress and plastic strain. As the size of the voids increase, the plastic strain will be concentrated at bands with high concentration of voids which in term will lead to local necking instabilities between the voids. Upon further plastic strain, the voids will start to coalesce, which is the definition of crack propagation. This will typically happen in a finite region in front of the crack, the fracture process zone.

4.2 Cleavage

Another important fracture mechanism related to metals is cleavage [40]. The crack propagation is more rapid during cleavage than for ductile fracture and the crack tend to follow certain crystallographic planes. Under certain conditions, cleavage can be both ductile and brittle. The crack propagates through the grains of the metal, and the propagation direction in each grain is determined by which plane is most favorable with regards to lattice orientation. The crack propagates through breaking of the bonds between the atoms in front of the crack tip. The initiation of cleavage is dependent on the existence of a dislocation in front of the crack tip that will lower the required stress to break the bonds. As discussed in section 2.3.1, the presence of dislocations will significantly lower the strength of the metal. However, it is more common that the cleavage initiates from a micro-crack or an inclusion as these defects introduce higher stress concentrations than the dislocations [40]. Brittle fracture is most common in crystalline structures where the number of slip systems is limited such as in α-iron, which normally has a BCC crystal structure [4]. Pure aluminium has a FCC crystalline structure which, as discussed in section 2.3.6, has a lot of possible slip systems. This is one of the reasons why aluminium is not likely to fail by cleavage unless the temperature is very low [4].

4.3 Intergranular fracture

Intergranular fracture means fracture along the grain boundaries [40]. A number of factors will increase the risk for crack propagation along the grain boundaries. One of the most important is the formation of second phase particles at the grain boundaries. As discussed in section 3.1.4, solute atoms in the vicinity of the grain boundary tend to migrate to the grain boundary under certain circumstances. These atoms may form large precipitates at the grain boundary (see e.g. Pardoen *et al.* [3]). Separation in the particle matrix interface will lead to void growth.

Some aluminium alloys are especially susceptible to intergranular fracture due to the precipitate free zone near the grain boundary. Damage in the PFZ may lead to failure before any large plastic strain develops inside the grain. The width of the PFZ along with its mechanical properties relative to the grain interior are important factors with respect to intergranular fracture (see e.g. Pardoen *et al.* [3] or Scheylvaerts [35]). The competition between intergranular and transgranular fracture influence the overall toughness of the material [35]. This competition is further discussed in section 6.8.

Chapter 5

The cohesive element model

The cohesive element model is a method used in computational fracture mechanics among other methods such as Linear Elastic Fracture Mechanics (LEFM) [40], the eXtended Finite Element Method (XFEM) [47, 48] and element erosion.

The cohesive zone model which is the base of cohesive elements was first introduced by Dugdale (1960) [49] with the aim of predicting the extent of the plastic zone in front of a sharp notch in a sheet of metal. Then the concept of cohesive elements was introduced by Hilleborg (1976) [50] to simulate the formation and propagation of cracks in concrete. This method is widely used and rather straight forward to implement, hence it is implemented in many finite element codes. The finite element software LS-DYNA [1] will be used for the analysis in this thesis, therefore, emphasize will be put on explaining the cohesive element model as implemented in this program.

The cohesive zone model assume that crack propagation is a gradual process that take place over a finite zone in front of the crack tip, called a cohesive zone [49]. In aluminium, a common fracture mechanism is ductile fracture by growth and coalescence of voids initiated from inclusions. As the voids grow in the fracture process zone in front of the crack, the traction capacity will decrease gradually [40]. The process of void growth was discussed in section 4.1. Fracture analysis will not be carried out in this thesis. However, the cohesive element model will still be studied, as this model might be well suited for modelling fracture in aluminium.

5.1 Damage modelling with continuum elements

In an article by René de Borst [51], a simple bar loaded in uniaxial tension meshed with one element over the cross section was used to address the strong mesh sensitivity that arise when normal continuum elements are assigned a material with a softening branch to simulate damage. Figure 5.1 gives an example of such a material model. If one of the elements is given a slightly lower yield stress than the rest, which will be the case due to numerical inaccuracy, this element will yield before the other elements. Since the material strength is monotonically decreasing after yielding, failure will occur in this

element while the rest of the elements will unload elastically. The strain in the bar when loaded beyond maximum capacity is given in equation (5.2). It will be an average of the damaged element and the elements in the elastic regime.

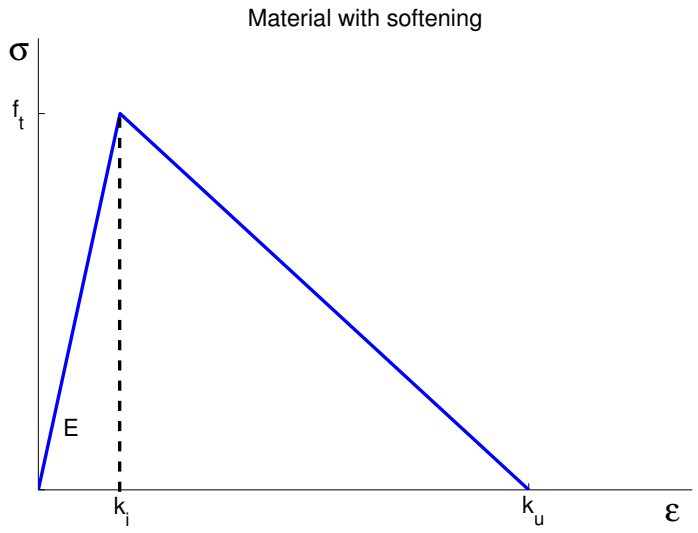

Figure 5.1: *Material response with softening branch [51].*

The slope of the softening branch h is not dependent on the number of finite elements in the bar and is expressed as:

$$h = -\frac{f_t}{k_u - k_i} \tag{5.1}$$

$$\bar{\varepsilon} = \overbrace{\frac{\sigma}{E}}^{Elastic} + \frac{\overbrace{n(f_t - \sigma)}^{Softening}}{mE}, \tag{5.2}$$

where

- $\bar{\varepsilon}$ is the average strain in the bar.
- E is the Young's modulus.
- σ denotes the uniaxial stress in the bar.
- n is a parameter related to the slope of the softening branch $n = \frac{k_u}{k_i}$.
- m is the number of elements along the bar.
- f_t is the peak stress.

The average strain in the bar $\bar{\varepsilon}$ is in other words dependent on the number of elements m. The energy dissipation from the plasticity surrounding the damage area is what prevents unstable crack growth [40]. When the number of finite elements is increased towards infinity, the volume of the damaged element as well as the area under the material response curve will approach zero. Hence there will be no resistance to crack growth after initiation. Such a material response to fracture is clearly not physical and mesh sensitive.

5.2 Cohesive elements

Instead of using a stress based failure criteria (section 5.1) the cohesive element model is based on the work of separation [50]: $G_c = \int_0^\infty \sigma(\delta)\, d\delta$. Using this failure criteria the slope h of the softening part of the stress-strain curve (see previous section) will be inversely proportional to the number of elements [51].

The average strain in the bar will now be written as:

$$\bar{\varepsilon} = \frac{\sigma}{E} - \frac{2G_c(\sigma - f_t)}{Lf_t^2}, \tag{5.3}$$

where L is the length of the bar. The average strain will no longer be dependent on the number of elements m. Consequently the cohesive element model is not mesh dependent. This is only true to some extent, as will be discussed in section 5.2.3.

Cohesive elements are placed at the interface between the continuum elements. Usually the cohesive elements are assigned zero thickness and can handle overlap of the continuum elements without becoming unstable [52]. In that sense, these elements behave more like non-linear springs than normal finite elements. The cohesive elements are responsible for transferring traction between the continuum elements. A three dimensional cohesive element has only three traction components, one normal and two shear components, in contrast to the continuum elements which have six.

Many different implementations of the cohesive element model exist for various applications. The work by Tvergaard and Hutchinson [53, 54, 55, 56] is widely recognized and their model is implemented in LS-DYNA [57]. In the following, the cohesive element model will be explained through the implementation by Tvergaard and Hutchinson.

5.2.1 Traction-separation load curve

The deformation of the cohesive element is defined through the relative displacement of the adjacent continuum elements [58]. In the reference configuration prior to loading, $\boldsymbol{X}^A$ and $\boldsymbol{X}^B$ are two coinciding points on the boundary of two different continuum elements which means that $\boldsymbol{X}^A = \boldsymbol{X}^B$. During separation the same points have position vectors $\boldsymbol{x}^A$ and $\boldsymbol{x}^B$. The displacement of the two points will be given by the following vectors:

$$\boldsymbol{u}^A = \boldsymbol{x}^A - \boldsymbol{X}^A, \tag{5.4}$$

$$\boldsymbol{u}^B = \boldsymbol{x}^B - \boldsymbol{X}^B. \tag{5.5}$$

The relative displacement of the two points is what will determine the separation of the cohesive element.

$$\Delta\boldsymbol{u}^{AB} = \boldsymbol{u}^A - \boldsymbol{u}^B = \boldsymbol{x}^A - \boldsymbol{x}^B \tag{5.6}$$

The relative displacement vector $\Delta \boldsymbol{u}^{AB}$ is decomposed into a tangential and a normal component by scalar product with $\boldsymbol{n}^0$ and $\boldsymbol{t}^0$ which are the unit vector in the normal and tangential direction, relative to the undeformed interface, respectively.

$$\delta_n = \Delta \boldsymbol{u}^{AB} \cdot \boldsymbol{n}^0 \tag{5.7}$$
$$\delta_t = \Delta \boldsymbol{u}^{AB} \cdot \boldsymbol{t}^0 \tag{5.8}$$

The nominal traction $\boldsymbol{T}$ is split into a normal and a shear component by projection on $\boldsymbol{n}^0$ and $\boldsymbol{t}^0$ respectively.

$$T_n = \boldsymbol{T} \cdot \boldsymbol{n}^0 \tag{5.9}$$
$$T_t = \boldsymbol{T} \cdot \boldsymbol{t}^0 \tag{5.10}$$

In the cohesive element model the material response during failure is described by a traction-separation law [53]. This law gives the relationship between the cohesive traction σ and the effective separation δ. The relation between the cohesive traction σ and the nominal traction $\boldsymbol{T}$ will be discussed later in this section. In general the effective separation is a function of both the normal separation δ_n and the tangential (shear) separation δ_t [54]. Figure 5.2 is taken from the LS-DYNA keyword user's manual [57] and describes how the mixed mode behavior will influence the load bearing capacity in the normal and tangential mode upon mixed mode loading. The figure illustrates that damage in one mode will reduce the capacity in the other mode.

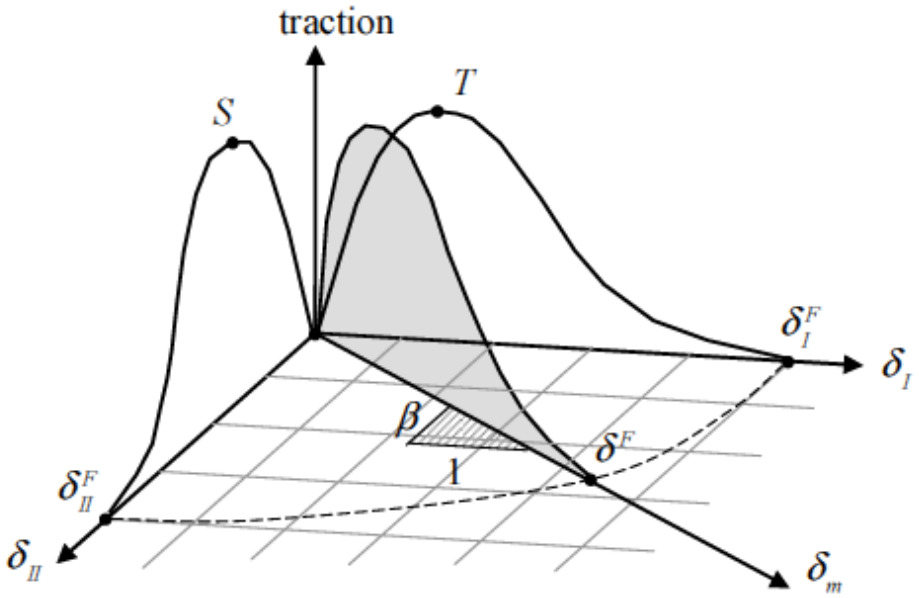

Figure 5.2: *Mixed mode behavior [57].*

An effective opening δ could be defined like shown in the equation below [54]:

$$\delta = \left(\left(\frac{\delta_n}{\delta_n^c} \right)^2 + \left(\frac{\delta_t}{\delta_t^c} \right) \right)^{1/2}, \tag{5.11}$$

where δ_n^c and δ_t^c are the failure separation normal and tangential to the undeformed surface respectively.

The traction-separation load curve (TSLC) is a representation of the traction separation law [53]. The shape of this curve might depend on the material and the implementation of the model. However, some important features are the peak cohesive stress which describes the initiation of failure and the softening branch which describes the material response during failure [59]. The shape of this curve can be determined experimentally. However, Tvergaard and Hutchinson [55] argue that the shape of the TSLC is less important. Emphasis should be put on calibrating the work of separation parameter Γ_0 and peak traction $\hat{\sigma}$. The work of separation is defined as the total area under the TSLC and can be interpreted as the external energy required for crack extension by one unit area [59]. The area under the TSLC is given by [54]:

$$\phi(\delta_n, \delta_t) = \delta_n^c \int_0^\delta \sigma(\delta)\, \mathrm{d}\delta \tag{5.12}$$

where $\sigma(\delta)$ is the cohesive traction at an effective separation δ and $\hat{\sigma}$ is the maximum traction in the cohesive element. This relation only applies if the nominal traction $\boldsymbol{T}$ and the normal and tangential separation δ_n, δ_t is given with respect to the undeformed configuration as shown in the previous section. Figure 5.3 shows the trapezoidal TSLC used by Tvergaard *et al.* [53].

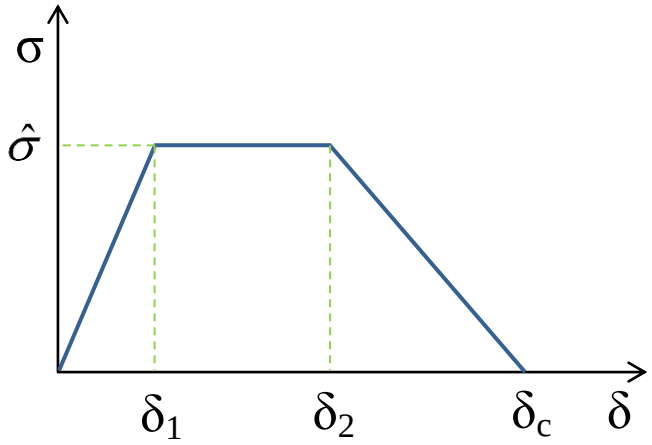

Figure 5.3: *A trapezoidal traction separation load curve [53].*

The work of separation per unit undeformed area Γ_0 is equal to $\phi(\delta_n, \delta_t)$ when $\delta = 1$, i.e. the total area under the TSLC. The nominal traction components in the cohesive element are related to the potential $\phi(u_n, u_t)$ and the cohesive traction σ as given in equation (5.13) and (5.14) [54].

$$T_n = \frac{\partial \phi}{\partial \delta_n} = \frac{\sigma(\delta)}{\delta}\frac{\delta_n}{\delta_n^c}, \tag{5.13}$$

$$T_t = \frac{\partial \phi}{\partial \delta_t} = \frac{\sigma(\delta)}{\delta}\frac{\delta_t}{\delta_t^c}\frac{\delta_n^c}{\delta_t^c}. \tag{5.14}$$

The discrete equation for the solution of the cohesive element model will not be given here, see e.g. the article by Chowdhury *et al.* (2000) [58].

5.2.2 Unloading behavior

For cases where the loading is reversed, unloading of the cohesive element must be taken into account. Unloading of a cohesive element can be done in different manners. Some account for reduced capacity in the element upon reloading and some do not. Three different approaches will be presented here.

First is the model by Tvergaard and Hutchinson [53]. In this implementation of the cohesive element model, the element will retain its full capacity after unloading. The response of the cohesive element will follow the same TSLC during loading and unloading as illustrated in figure 5.4. In other words, when the element is fully unloaded the separation is equal to zero and the separation history do not influence the capacity of the element.

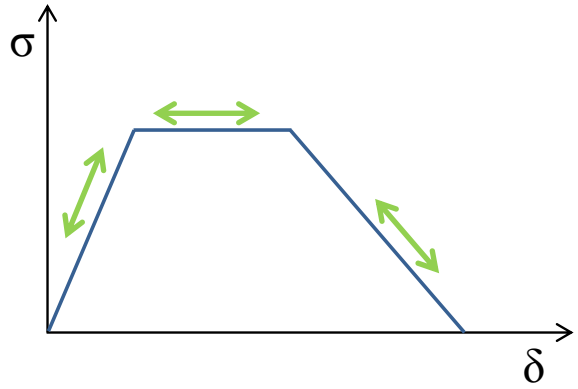

Figure 5.4: *Unloading behavior of cohesive element proposed by Tvergaard et al. [53].*

A different approach proposed by Camacho *et al.* in (1996) [60] is to unload along a line straight towards the origin in the TSLC coordinate system (see figure 5.5). Similar to the model by Tvergaard *et al.* this implementation will result in zero separation after the element is fully unloaded. However, when reloading the element its response will not follow the original TSLC, but follow the previous unloading path. This will result in a reduced area under the TSLC and consequently a reduction of the cohesive element capacity. Hence, the separation history determines the response of the cohesive element.

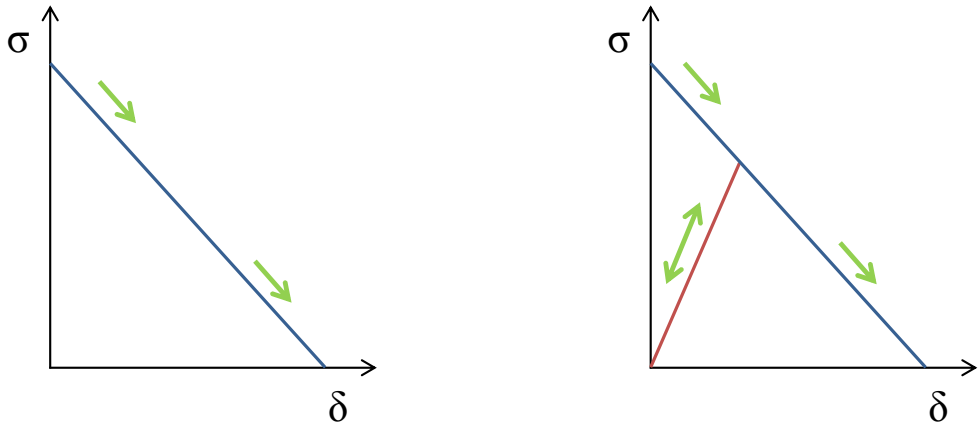

(a) (b)

Figure 5.5: *Unloading behavior proposed by Camacho et al. [60].*

The last approach is unloading along a slope equal to the initial slope upon loading (see figure 5.6). Such a model was proposed by Roe *et al.* (2003) [61] for the modelling of fatigue crack growth. Cyclic loading is essential to fatigue and the unloading behavior of the cohesive element is therefore important. When the cohesive element is loaded beyond a critical value, the separation will be irreversible. Upon further loading, the critical value for accumulation of separation will decrease as illustrated in figure 5.6(a). Unloading and reverse separation in shear needs extra attention as the capacity of the cohesive element will decrease also during reverse separation as illustrated in figure 5.6(b).

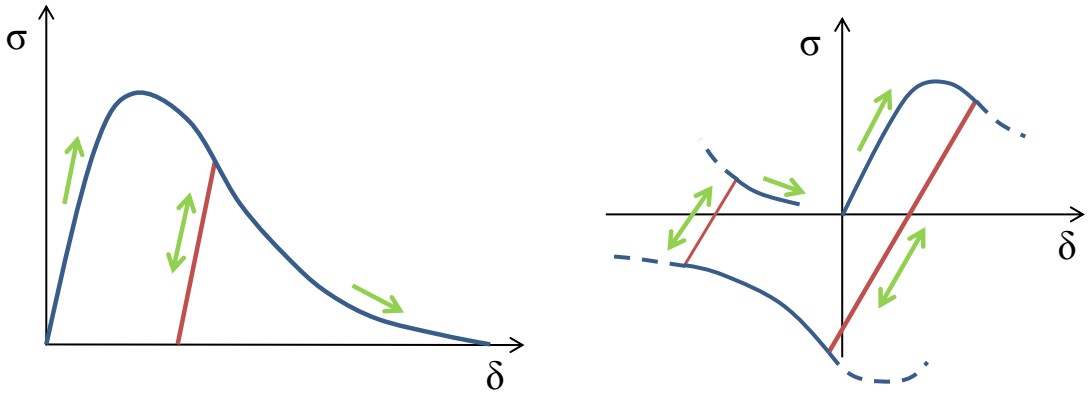

(a) (b)

Figure 5.6: *Unloading behavior of a cohesive element as proposed by Roe et al. [61].*

5.2.3 Mesh dependency

The mesh dependency of cohesive elements is a huge topic, but it will only be discussed briefly here. As mentioned earlier, the cohesive elements are located at the interface between continuum elements. The mesh dependency in the cohesive element model is

partly due to the limited number of possible crack propagation directions. Since crack propagation is limited to a finite number of prescribed directions, the solution will be mesh dependent for problems where the crack propagation path is unknown.

Normal h-refinement of the mesh will reduce the mesh dependency simply due to the increased number of opportunities the crack will have to change direction [62]. Generally an irregular mesh will better address the issues related to mesh dependency. In an irregular mesh, the crack propagation will be forced to change direction which will eliminate favoring of certain propagation directions. However, an irregular mesh might challenge the convergence of the model.

Another technic is to use triangular instead of quadrilateral bulk elements. This will increase the number of possible propagation directions from three to seven (see figure 5.7).

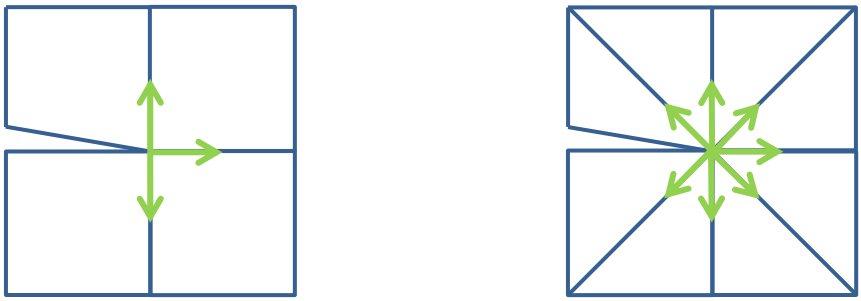

(a) (b)

Figure 5.7: *The different possible propagation directions in a mesh of quadrilateral elements (a) and triangular elements (b).*

Since crack propagation is limited to one whole element at a time, it is important that the element size is significantly smaller than cohesive zone [63]. Tvergaard *et al.* [53] found that the ratio between the element length and the critical separation had a great influence on the required size of the refined region around the crack tip.

Chapter 6

Modelling of microstructure

The aim of this study is to explore numerically the competition between intergranular and transgranular fracture in aluminium. This is carried out by investigating the distribution of stresses and strains in a microstructure consisting of grains, grain boundaries and precipitate free zones. A small sample of a microstructure will be subjected to various loading conditions and the distribution of effective plastic strain as well as the stress triaxiality will be given special attention.

The literature study in chapter 2 revealed that a crystal is anisotropic. On a microscopic scale, this might influence the distribution of stresses and strains. In this thesis, both a model using isotropic plasticity and one using crystal plasticity will be subjected to analysis in order to study the effect of anisotropy. A number of different realization of the crystal plasticity model will be used in the simulations, to see whether the crystallographic orientations of the grains influence the result.

6.1 Representative Volume Element

In modelling of microstructure, the use of a representative volume element (RVE) significantly reduce the required CPU time [64]. A RVE is a certain volume V which is chosen such that it represents the effective parameters of the material with a given accuracy. Whether it is possible to model a problem as a RVE is dependent on a number of factors including the material response. For instance, materials which exhibit softening might not be possible to represent with a RVE. Most success has been encountered in modelling of linear elastic materials as RVEs. The boundary conditions of a RVE do not need to be periodic. However, periodicity will enable a smaller RVE size [65].

The number of grains in the model used in this thesis is low, it is therefore reasonable to assume that it cannot be considered representative for any given microstructure. Extensive analysis to determine whether the geometry used here is a representative volume element will not be carried out.

6.2 The model

The geometry is not made to replicate any specific aluminium alloy, but to investigate how stresses and strains are distributed in a heterogeneous microstructure. The chosen dimensions might therefore not be physical. The model is similar to what is used in the work by Scheylvaerts [35]. In this thesis the model is composed by one complete hexagonal grain and parts of the six surrounding grains (see figure 6.1). The only feature that makes this model not periodic is the grain boundaries on the top and bottom of model which are not included. The total dimensions of the model are $L_x \times L_y = 12 \times 16\,[\text{mm}]$ and the width of the PFZ is 0.2 mm. A figure giving the dimensions of the model is available in appendix A. The LS-DYNA keyword files are included on the attached CD.

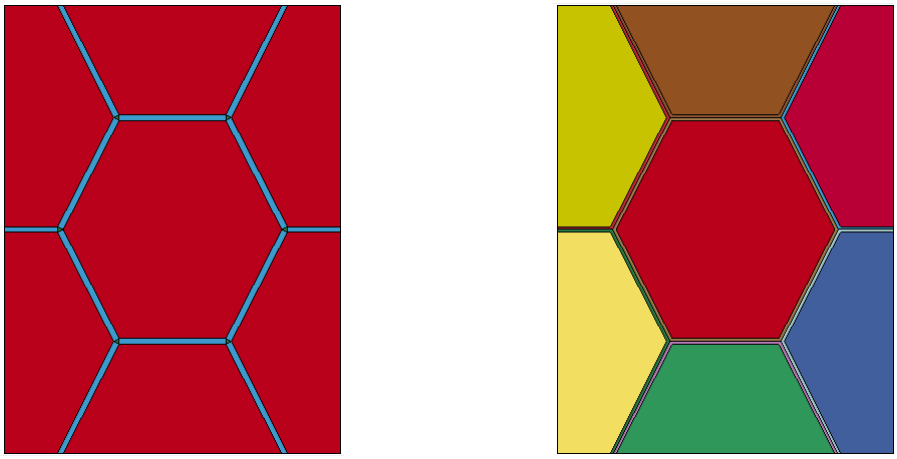

(a) (b)

Figure 6.1: *The geometry for (a) the model using isotropic plasticity and (b) for the model using crystal plasticity.*

The width of the PFZ is thought to influence the competition between intergranular and transgranular fracture [35], however this will not be investigated in this thesis and will be of further work. The effect of different grain shapes will also not be studied in this thesis although it is expected to influence the fracture toughness [35].

To account for different material properties in the grain interior and in the PFZ, these regions will be meshed separately. In the model using crystal plasticity, the PFZ is divided in two along its length axis in order to assign the same crystallographic orientation in a grain and its associated PFZ. The grain boundary is assumed to be located in the middle of the PFZ. All the grains will be assigned different crystallographic orientations randomly generated to represent a cube texture with a spread of $\pm 15°$. However, since the number of grains in this model is limited, it is not thought to be representative for any texture.

6.3 Materials

Two material models are compared, an isotropic plasticity model and a crystal plasticity model. For simplicity, it is assumed that both materials will have an elastic-linear plastic response. The crystal plasticity model will be calibrated using a single element model. This element will be assigned a random orientation drawn from a cube texture with orientations within $\pm 15°$. The material model will be calibrated such that this single element will have a response to uniaxial loading equal to the isotropic model. Details on how the calibration is carried out are presented in section 6.3.2.

6.3.1 Isotropic plasticity

The mechanical properties in the model using isotropic plasticity will be divided in two sections: the grain interior and the PFZ. The mechanical properties within all the grains will be equal. The material parameters for the isotropic plasticity model are shown in table 6.1. The material card used in LS-DYNA is called:
*MAT_ISOTROPIC_ELASTIC_PLASTIC [57].

Table 6.1: *Material parameters for isotropic plasticity model.*

	Grain interior	PFZ
Poisson's ratio	0.33	0.33
Mass density ρ	20.00 kg/mm^3	20.00 kg/mm^3
Young's modulus	70000 MPa	70000 MPa
Shear modulus G	26300 MPa	26300 MPa
Yield stress σ_y	200 MPa	-
Bulk modulus K	68600 MPa	68600 MPa
Tangent modulus E_t	40 MPa	-

The aim of this study is to see the effect of the ratio between the material parameters in the grain interior and in the PFZ. The material parameters used in these analyses are therefore not calibrated to match any specific alloy. However, they are all within the range of what could be expected for an aluminium alloy. The yield stress for an age hardened aluminium-copper alloy (aluminium 2036-T4) is approximately 200MPa [66].

The material parameters for the PFZ are not straight forward to determine. However, it is reasonable to assume that the elastic parameters are the same as for the grain interior since the effect of the ageing treatment on the elastic properties is only minor [4]. The plastic parameters of the PFZ will be subjects to a parameter study and will be further discussed in section 6.4.2. As a benchmark material, the PFZ is given a yield stress of 100 MPa and a tangent modulus of 120 MPa.

To reduce the computational time, the mass density was set as high as possible (20 kg/mm^3). The kinetic energy was monitored to ensure that oscillations are avoided. The critical time step of an explicit analysis is given in equation (6.1).

$$t_c \propto L/v \tag{6.1}$$

where

- L is the characteristic element length.
- $v = \sqrt{\frac{E}{\rho}}$ is the wave velocity.

The kinetic and internal energy for an uniaxial tension test are shown in figure 6.2 (the mesh used here will be further discussed in section 6.5). The kinetic energy is low compared to the internal energy even for low global strains. The definition of the global average effective plastic strain will be given in section 6.4.

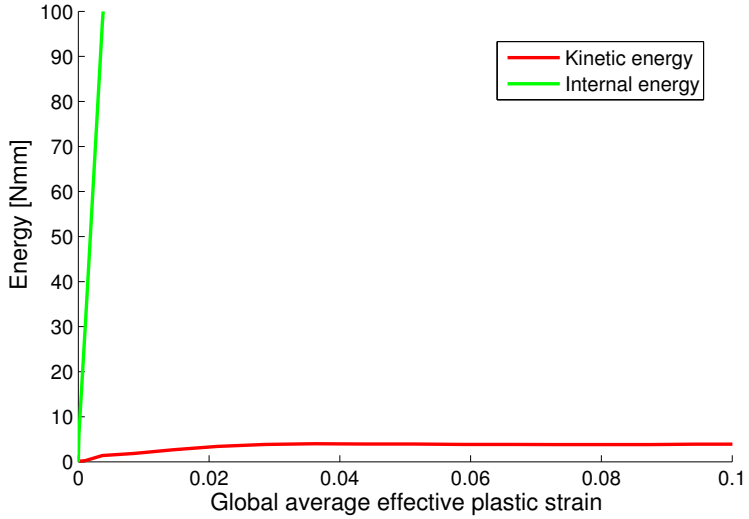

Figure 6.2: *Kinetic and internal energy for the isotropic plasticity model assigned the benchmark material and loaded in uniaxial tension.*

6.3.2 Crystal plasticity

The crystallographic orientations are picked randomly from a cube texture with a spread of $\pm 15°$. Cube texture is thought to be a good choice since the hexagonal grains are nearly equiaxes. Each grain along with its corresponding PFZ is assigned a unique orientation. Since the model consists of only seven grains it cannot be considered representative for any texture, but only as a small sample. Three different realizations of the grain orientations have been tested.

The LS-DYNA material card *MAT_USER_DEFINED_MATERIAL_MODELS [57] was used to model the crystal plasticity. This card allows for a tailor made material model which simulates the behavior of FCC crystals. The material card is shown next.

```
*MAT_USER_DEFINED_MATERIAL_MODELS
$      mid        ro        mt       lmc       nhv    iortho     ibulk        ig
        xx      2.00        41        24        68         0        23        24
$    ivect     ifail    itherm    ihyper      ieos
         0         0         0         1         0
$      c11       c12       c44     Alpha     Euler angles         ->      Tdot
1.0643E+5   60350.0   28210.0     0.000      Phi1       PSI      Phi2      0.00
$ Texture    Int Pt   Int Sch   Tex out   Max Wp   EltType    SC mod         N
         0         1        12       0.0      0.0         2         5         1
$#  Constants of the SC model                                    ->      Bulk     Shear
     0.001     0.005       1.4      tau0    theta1      tau1   68600.0   26300.0
```

The angles `phi1`, `PSI` and `phi2` are the Euler angles defining the crystallographic orientation of the grain (see e.g. Kocks *et al.* [20]). The mass density (`ro`) was set to 2.00kg/m^3, which is 10% of the density for the isotropic model, to avoid oscillations. The reason why the crystal plasticity model required a lower mass density might be due to the sudden change in stiffness as new slip systems become active.

The parameters `c11`, `c12` and `c44` are the constants of the material stiffness matrix $\boldsymbol{C}$ as shown in equation (6.5) (see e.g. Dumoulin *et al.* (2009) [67]). The values for $c11$, $c12$ and $c44$ have been determined for pure aluminium by Thomas (1968) [68]. Equivalent values for precipitation hardened aluminium have not been obtained.

$$\boldsymbol{\sigma} = \boldsymbol{C}\boldsymbol{\varepsilon} \tag{6.2}$$

Using the Voigt notation [41] the stress and strain matrices can be written as:

$$\begin{bmatrix} \sigma_{xx} & \sigma_{yy} & \sigma_{zz} & \sigma_{xy} & \sigma_{yz} & \sigma_{xz} \end{bmatrix} = \begin{bmatrix} \sigma_1 & \sigma_2 & \sigma_3 & \sigma_4 & \sigma_5 & \sigma_6 \end{bmatrix} \tag{6.3}$$

$$\begin{bmatrix} \varepsilon_{xx} & \varepsilon_{yy} & \varepsilon_{zz} & \varepsilon_{xy} & \varepsilon_{yz} & \varepsilon_{xz} \end{bmatrix} = \begin{bmatrix} \varepsilon_1 & \varepsilon_2 & \varepsilon_3 & \varepsilon_4 & \varepsilon_5 & \varepsilon_6 \end{bmatrix}. \tag{6.4}$$

$$\begin{bmatrix} \sigma_1 \\ \sigma_2 \\ \sigma_3 \\ \sigma_4 \\ \sigma_5 \\ \sigma_6 \end{bmatrix} = \begin{bmatrix} C_{11} & C_{12} & C_{12} & 0 & 0 & 0 \\ & C_{11} & C_{12} & 0 & 0 & 0 \\ & & C_{11} & 0 & 0 & 0 \\ & & & C_{44} & 0 & 0 \\ & & & & C_{44} & 0 \\ & \text{sym.} & & & & C_{44} \end{bmatrix} \begin{bmatrix} \varepsilon_1 \\ \varepsilon_2 \\ \varepsilon_3 \\ 2\varepsilon_4 \\ 2\varepsilon_5 \\ 2\varepsilon_6 \end{bmatrix} \tag{6.5}$$

Similar to the isotropic plasticity model, the material response for the crystal plasticity model is chosen to be elasto-plastic with linear hardening. For small strains, the elastic linear plastic response can be reproduced by manipulation of the coefficients in a Voce hardening law. The Voce hardening law is `SC model` number 5.

In `SC model` number 5, the plastic parameter γ is an accumulation of the slip in all slip systems α_i (see equation (6.6)).

$$\gamma = \sum_{\alpha_i} |\gamma^{\alpha_i}| \tag{6.6}$$

Further, the condition for slip is:

$$\dot{\gamma}^{\alpha} = \dot{\gamma}_0 \left| \frac{\tau^{\alpha}}{\tau_c^{\alpha}} \right|^{\frac{1}{m}} sgn(\tau^{\alpha}) \tag{6.7}$$

where

- $\dot{\gamma}^{\alpha}$ is the strain rate in slip system α.
- $\dot{\gamma}_0^{\alpha}$ is the reference strain rate.
- τ^{α} denotes the resolved shear stress in slip system α.
- τ_c^{α} is the critical resolved shear stress in slip system α.

The critical resolved shear stress in glide plane α is given by:

$$\tau_c^{\alpha}(\gamma) = \tau_0 + \tau_1 \left(1 - exp\left(-\frac{\theta_1}{\tau_1} \cdot \gamma \right) \right), \tag{6.8}$$

where τ_0 can be interpreted as the critical resolved shear stress for slip and τ_1 as the total hardening capacity (see equation (6.9)).

$$\lim_{\gamma \to \infty} \tau_c^{\alpha}(\gamma) = \tau_0 + \tau_1 \tag{6.9}$$

The aim is to simulate a linear plastic behavior. This can be obtained by selecting a high number for τ_1. The slope of the stress-strain curve will then be approximately constant over a small strain interval.

The parameter θ_1 in equation (6.8) corresponds to the slope of the stress-strain curve directly after yielding. This can be shown by differentiation of (6.8).

$$\frac{d\tau_c^{\alpha}(\gamma)}{d\gamma} = \tau_1 \left(-exp\left(-\frac{\theta_1}{\tau_1} \cdot \gamma \right) \right) \cdot - \left(\frac{\theta_1}{\tau_1} \right) \tag{6.10}$$

$$\lim_{\gamma \to 0^+} \frac{d\tau_c^{\alpha}(\gamma)}{d\gamma} = \theta_1 \tag{6.11}$$

In order to determine the three parameters τ_0, τ_1 and θ_1, a model using one 3D solid element loaded in uniaxial tension was used. The keyword file for this model is given on the attached CD. The parameters are fitted such that the response of the element to uniaxial tension replicates the stress-strain curve of the benchmark material for the isotropic material model. The material for the grain interior was calibrated to have a yield stress of 200 MPa and a tangent modulus of 40 MPa. The PFZ material was calibrated to have a yield stress of 100 MPa and a tangent modulus of 120 MPa (see figure 6.3). Once appropriate parameters were obtained, four different crystallographic

orientations was tested both for the grain interior and the PFZ material (see table 6.2). These orientations were drawn randomly from a cube texture with orientations within 15°.

Table 6.2: *Crystallographic orientations used for calibration of material model.*

Test nr.	Phi1	PSI	Phi2
1	88.80	83.83	93.90
2	89.08	91.28	88.27
3	-94.87	94.24	85.70
4	-85.13	94.24	94.30

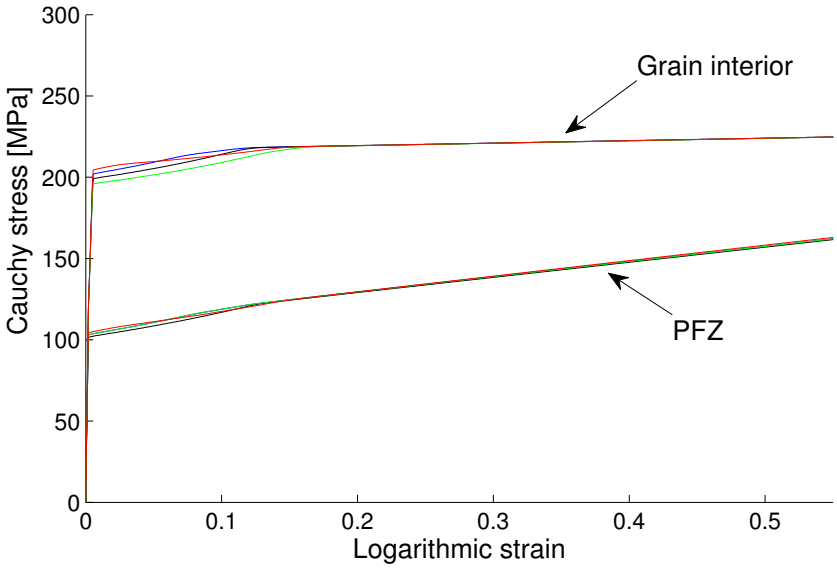

Figure 6.3: *Cauchy stress versus logarithmic strain for the single element model.*

The slopes of the stress-strain curves change at a logarithmic strain of 0.12. The reason is probably the activation of more slip systems at this strain. The strains in each individual slip system for test number 1 are plotted in figure 6.4. Around a global strain of approximately 0.12, six slip systems become active. The two slip systems active from the beginning get a reduced slope at a strain of 0.12, which indicate that the element deforms differently subsequent to the activation of new slip systems. The reason why all the tests have similar result is probably that the difference between the orientations is small. It might be expected a larger spread in the result for a wider range of crystallographic orientation. However, this will not be investigated in this thesis.

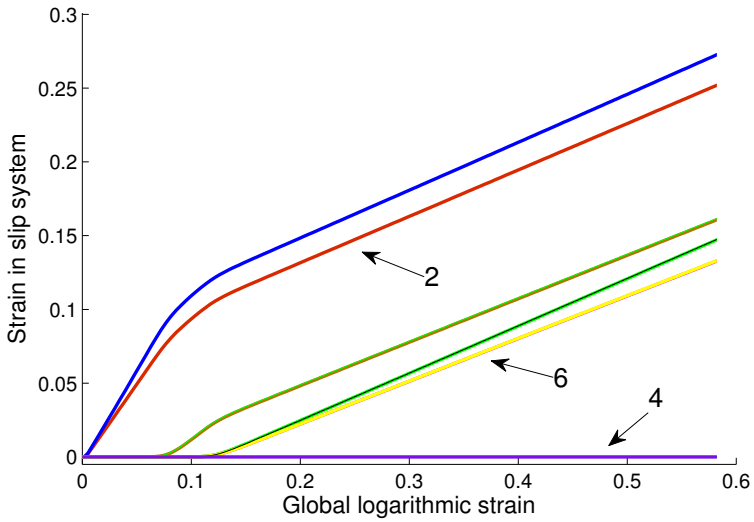

Figure 6.4: *Strain γ^{α_i} in each slip system α_i versus logarithmic strain in x-direction. There are altogether 12 independent slip systems in the FCC cube.*

Based on this study, the parameters given in table 6.3 were found to give a reasonable approximation of the material model.

Table 6.3: *Material parameters for the crystal plasticity model.*

	Grain interior	PFZ
τ_0	88	45
θ_1	2	12

The parameter τ_1 was set to 10 000 for both the grain interior and the PFZ. The relative error in stress will increase as the strain increase (see equation (6.12)). This choice of τ_1 will give a relative error of the stress at a logarithmic strain $\varepsilon = 1.5$ of $Err < 1e-3$.

$$Err = \frac{\sigma_{lin} - \sigma_{Voce}}{\sigma_{lin}}, \tag{6.12}$$

where σ_{lin} and σ_{Voce} is the stress calculated with an elastic-linear plastic and a Voce hardening law respectively, given the material parameters chosen for the crystal plasticity model.

Three different realizations of the grain orientations where used in the analyses. Figure 6.5 illustrates how the grains are numbered. The realizations are given in table 6.4.

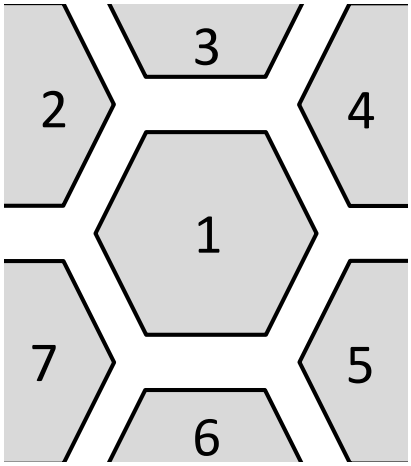

Figure 6.5: *Illustration of how the grains are numbered.*

Table 6.4: *Realizations of the crystallographic orientations.*

Grain nr.	Phi1	PSI	Phi2
Realization 1			
1	88.80	83.83	93.90
2	-88.80	83.83	86.10
3	-91.20	83.83	93.90
4	91.20	83.83	86.10
5	90.13	97.55	88.76
6	-90.13	97.55	91.24
7	-89.87	97.55	88.76
Realization 2			
1	89.08	91.28	88.27
2	-89.08	91.28	91.73
3	-90.92	91.28	88.27
4	90.92	91.28	91.73
5	92.36	82.88	88.28
6	-92.36	82.88	91.72
7	-87.64	82.88	88.28
Realization 3			
1	89.74	93.46	93.36
2	-89.74	93.46	86.64
3	-90.26	93.46	93.36
4	90.26	93.46	86.64
5	94.64	87.87	84.21
6	-94.64	87.87	95.79
7	-85.36	87.87	84.21

6.4 Method

6.4.1 Loading and boundary conditions

To see the effect of the global stress triaxiality ratio on the distribution of stresses and strains, three different loading modes will be investigated. Figure 6.6 illustrates how the boundary conditions are applied. The boundary on the left side was constrained against displacement in the x-direction and the boundary at the bottom was constrained against displacement in the y-direction. The magnitudes of the displacements are set so the maximum effective plastic strain in the PFZ was at least equal to 1.00. The modes are imposed the same way both when using isotropic plasticity and when using crystal plasticity.

The first mode is uniaxial tension. For this mode, a displacement of 15mm is applied in the positive x-direction to the boundary on the right side of the model (see figure 6.6). In order to obtain symmetry, the node set on the top of the model should be horizontal. This was enforced through defining the vertical velocity of all the nodes on the top of the model to be equal.

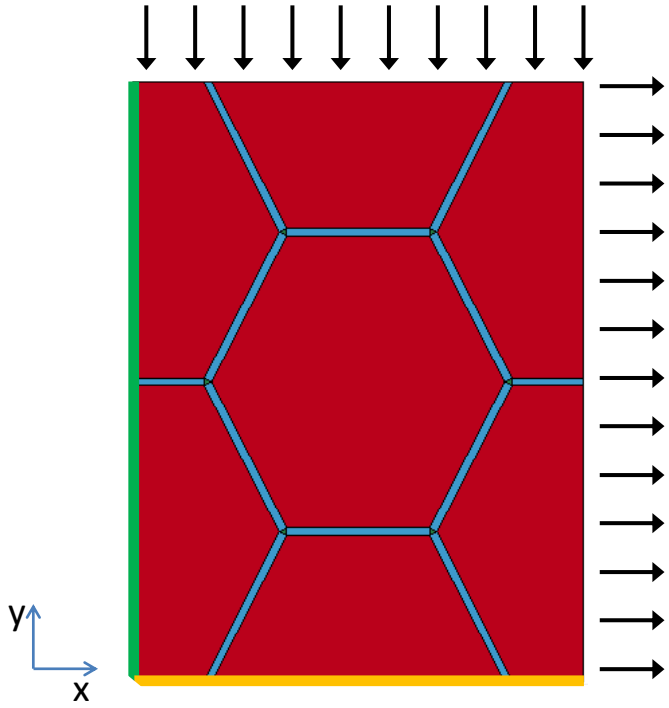

Figure 6.6: *Numerical model with boundary conditions. The green line represent the node set constrained against displacement in the x-direction. The yellow line represent the node set constrained against displacement in the y-direction. The arrows illustrate the applied displacements.*

The second mode will be called shear. This is imposed through a displacement of the right hand side of the model in the positive x-direction and a displacement in the negative

y-direction of the top of the model as illustrated in figure 6.6. The magnitude of the x-displacement is 9mm and the magnitude of the y-displacement is $(L_y/L_x)\cdot 9\text{mm} = 12\text{mm}$. Pure shear will have a global stress triaxiality ratio of zero. However, since plane strain formulation is used and the geometry is not a square, the triaxiality is expected to increase as the strain increase due to conservation of volume.

The last mode will be called biaxial tension. The relative displacement in the x-direction is twice the relative displacement in the y-direction. The right hand side of the model is imposed a displacement in the positive x-direction of 14mm and the top is imposed a displacement in the negative y-direction of $(L_y/2L_x)\cdot 14\text{mm} = 9.33\text{mm}$.

6.4.2 Parameter study

The elastic parameters (Young's modulus and Poisson's ratio) are almost independent of the heat treatment [4] and are therefore set to be equal for all the analyses. Then, the elasto-plastic model with linear hardening allows for the variation of two parameters: the yield stress and the tangent modulus. As mentioned in section 6.3, the material properties for the grain interior will be held constant while the properties for the PFZ will vary. This parameter study will be carried out using isotropic plasticity only.

Based on the literature study of the microstructure of aluminium (see chapter 3) the PFZ was found to have a low yield stress and a high work hardening rate compared to the grain interior. The yield stress of the PFZ is assumed to be in between the value for pure aluminium and for the age hardened grain interior. The yield stress of a commercially pure aluminium is about 20 MPa [7] and the grain interior was given a yield stress of 200 MPa.

The ratios between the parameters of the grain interior and the PFZ are defined by α and β as stated in the equations below.

$$\alpha = \frac{\sigma_0^{PFZ}}{\sigma_o^g} \tag{6.13}$$

$$\beta = \frac{E_t^{PFZ}}{E_t^g} \tag{6.14}$$

where

- σ_0^{PFZ} and σ_o^g is the yield stress for the PFZ and the grain interior respectively.
- E_t^{PFZ} and E_t^g is the tangent modulus for the PFZ and the grain interior respectively.

The following sets of values are chosen for α and β:

$$\alpha = \{0.25, 0.50, 0.75\} \tag{6.15}$$

$$\beta = \{2, 3, 4\} \tag{6.16}$$

Combination of α and β will give a total of nine analysis per loading mode. The different combinations are illustrated in figure 6.7.

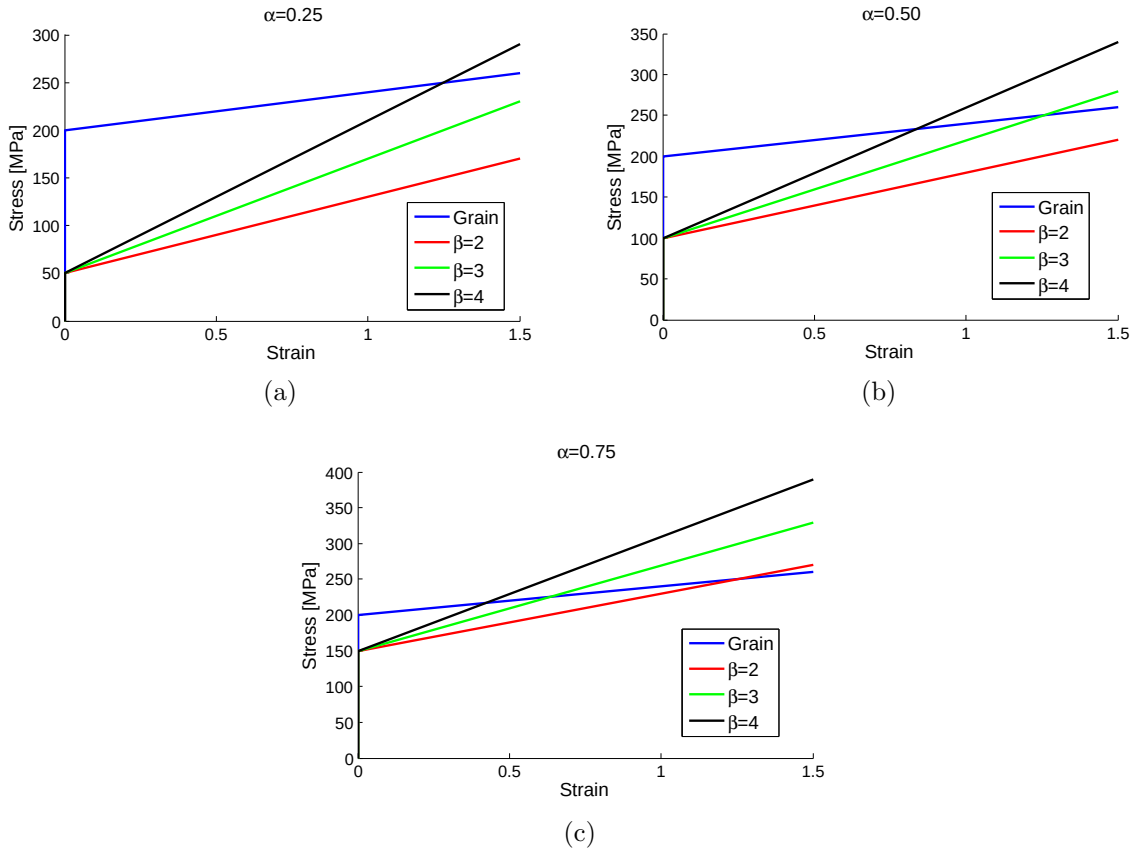

Figure 6.7: *The combinations of materials in PFZ and grain interior.*

The study of the distribution of stresses and strains was carried out in detail for the benchmark material, which is $\alpha = 0.5$ and $\beta = 3$. The literature study of fracture mechanisms uncovered that the effective plastic strain and the stress triaxiality ratio were important with respect to ductile fracture (see chapter 4). These parameters will therefore be the main focus.

The stress triaxiality ratio was discussed in section 4.1.1. The effective plastic strain is calculated from the plastic part of the strain rate tensor D^p_{ij} [69]:

$$\varepsilon^p_{eff} = \int_t \left[\frac{2}{3}(D^p_{ij} \cdot D^p_{ij})\right] \, \mathrm{d}t. \tag{6.17}$$

The maximum and average effective plastic strains are widely used terms in the subsequent sections. The maximum effective plastic strain is the maximum of all the element values in a part and the average effective plastic strain is the arithmetic average of the effective plastic strains of all the elements in a part. The global average effective plastic strain is the arithmetic average of all the elements of the model.

6.4.3 Crystal plasticity model

A number of analyses will be carried out using crystal plasticity in order to see if this influences the distribution of stresses and strains in the microstructure. The three realizations given in table 6.4 will be used for the three loading modes discussed in section 6.4.1. This will give a total of nine analyses which will be compared to the results obtained using isotropic plasticity. All the analyses are carried out using the material properties of the benchmark material as discussed in section 6.3.

6.5 Mesh

6.5.1 Mesh geometry

The model was meshed using quadrilateral plane strain shell elements, with one through thickness-integration point. The generation of the mesh was carried out using LS-INGRID [2]. Having a high resolution across the PFZ in order to capture possible gradients was emphasized. The mesh is illustrated in figure 6.8(a) and a detailed view of the junction between the grain boundaries is shown in figure 6.8(b). Different mesh densities were tested to ensure convergence and the results are presented in section 6.5.2.

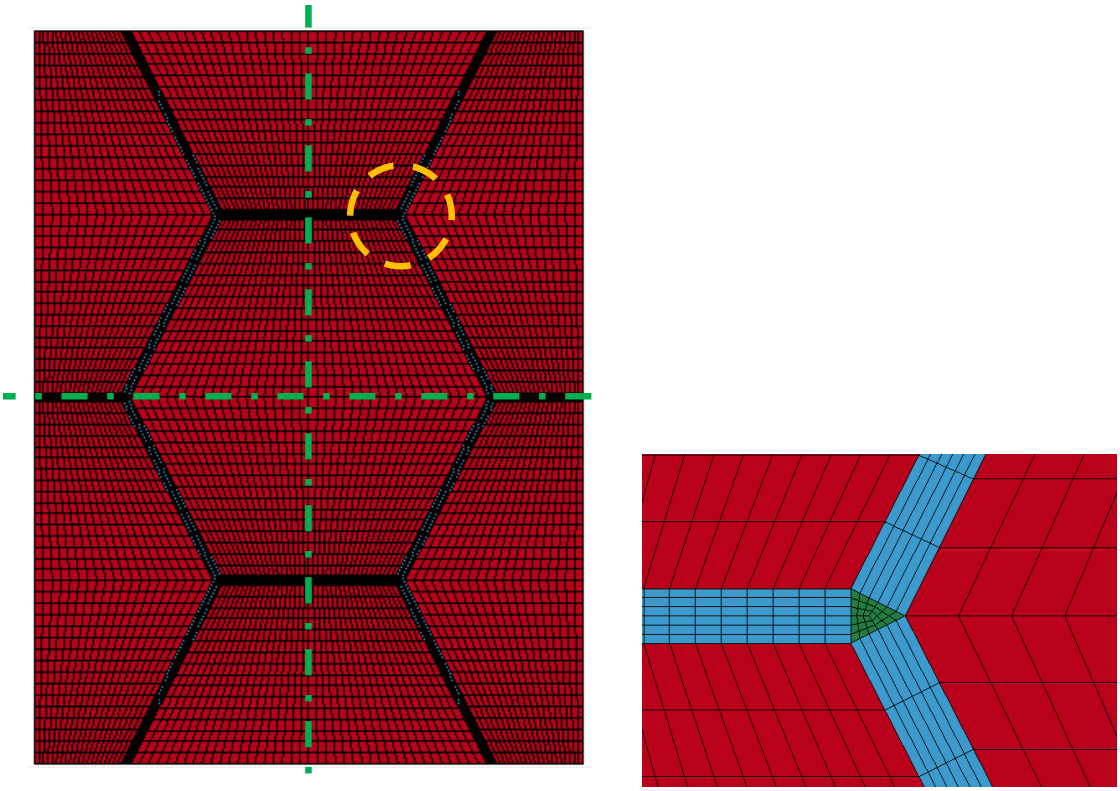

(a) (b)

Figure 6.8: *(a) shows the finite element mesh used in the analysis. Detail (b) shows the finite element mesh in the junction between grain boundaries.*

All the elements are either part of the grain interior or the PFZ and will thereby be given different mechanical properties. In the model using crystal plasticity, the PFZs are divided in two along their longitudinal axis to be able to assign the same unique crystallographic orientation to a given grain and its associated PFZ.

6.5.2 Test of convergence

Validation of the mesh was carried out using isotropic plasticity with benchmark material parameters and uniaxial tension loading conditions. In order to test convergence for the results of interest, simulations with a number of different mesh resolutions were carried out. The maximum effective plastic strain in the grain interior and in the PFZ, as well as the global internal energy was monitored. The upper left quarter of the model shown in figure 6.9 enables to identify the mesh density. The different meshes are named `cube-a-b-c`.

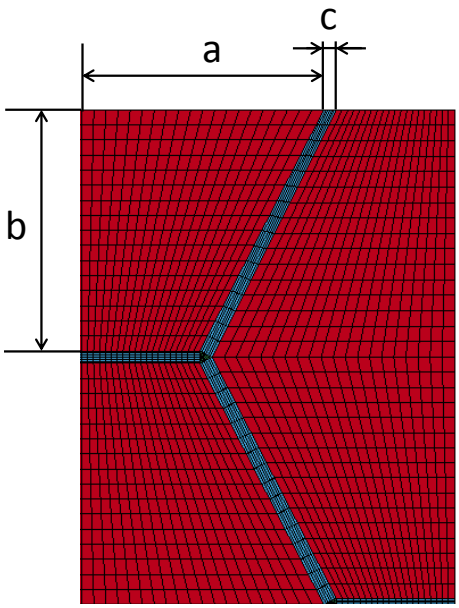

Figure 6.9: *Upper left quarter of the model showing how the mesh is named.*

The maximum effective plastic strain in the grain interior and in the PFZ is given in figure 6.10 and 6.11 respectively.

For the grain interior, the maximum effective plastic strain increases as the mesh becomes more refined. However, the difference between `cube-20-16-10` and `cube-40-32-10` is much less than between `cube-10-8-4` and `cube-20-16-4`.

Below a global average effective plastic strain of 0.7, the spread in maximum effective plastic strain is less in the PFZ than in the grain interior. For the PFZ, the spread in maximum effective plastic strain develop above a global average effective plastic strain of approximately 0.7. This development might be due to distortion of elements. The trend in the PFZ is similar to what was observed in the grain interior. That is, a more refined mesh predicts a higher maximum effective plastic strain. When the mesh is refined, it may capture high gradients in the strain field in a better way. The maximum effective plastic strain should therefore be higher for a more refined mesh.

The internal energy for a small strain interval is shown in figure 6.12. The internal energy for the whole loading history is given in appendix B, figure B-1.

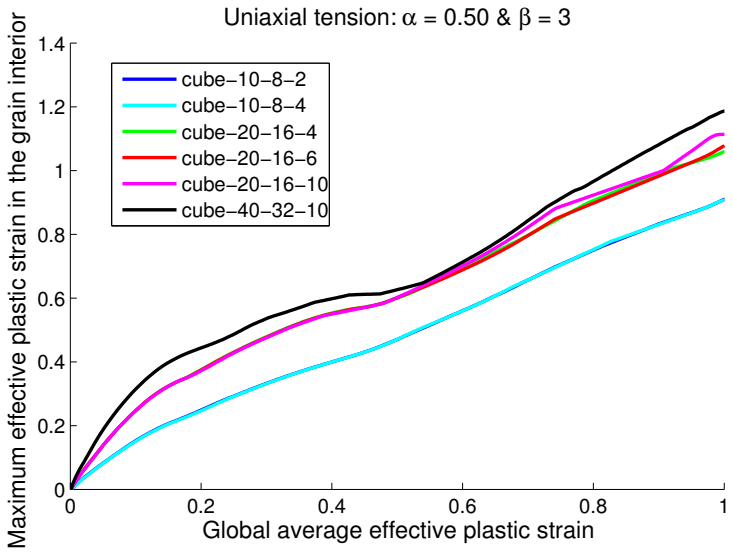

Figure 6.10: *The maximum effective plastic strain in the grain interior for different mesh densities.*

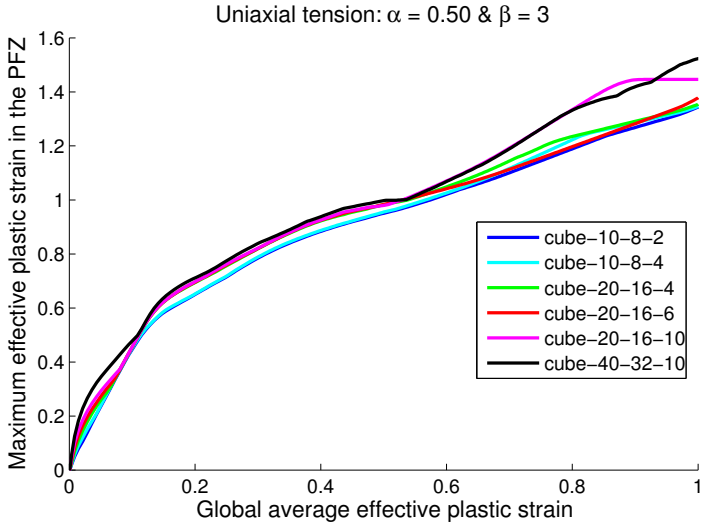

Figure 6.11: *The maximum effective plastic strain in the PFZ for different mesh densities.*

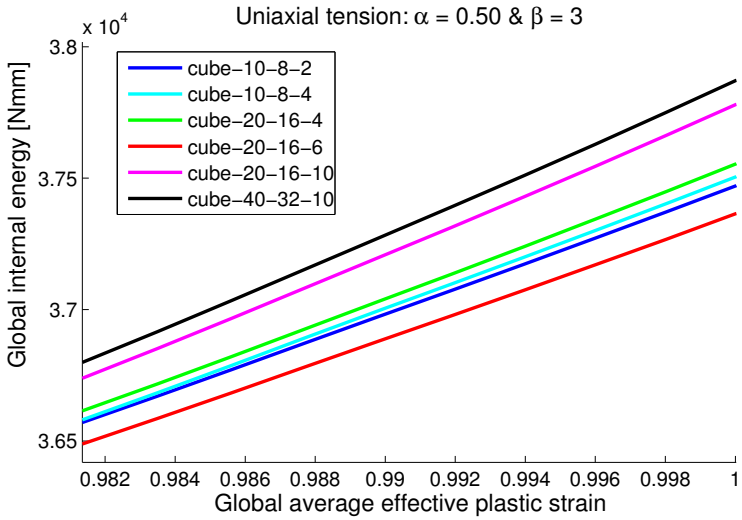

Figure 6.12: *Global internal energy for different mesh resolutions.*

The mesh `cube-20-16-6` has the lowest internal energy. When the internal energy is low, the energy dissipation is at its highest which indicates that the model has a soft response.

It is chosen to use hourglass control nr. 5 which is: *"Flanagan-Belytschko stiffness form with exact volume integration for solid elements"* [57]. The hourglass energy for the model using isotropic plasticity assigned the benchmark material and the mesh `cube-20-16-6` is shown in figure 6.13. The internal energy is in the order of 10^3Nmm (see appendix B figure B-1). The hourglass energy is therefore considered to be sufficiently low.

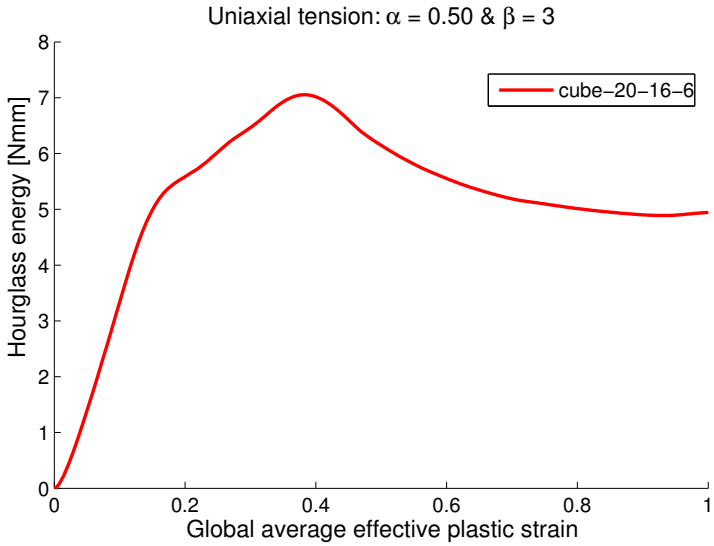

Figure 6.13: *The global hourglass energy for the model using isotropic plasticity loaded in uniaxial tension and assigned the mesh* `cube20-16-6` *and the benchmark material.*

Using a Linux cluster, the mesh `cube-20-16-6` required 1-2 CPU hours, the mesh `cube-20-16-10` required 6 CPU hours and `cube-40-32-10` required 35 CPU hours.

Based on these observations of mesh sensitivity, the mesh `cube-20-16-6` was chosen. This mesh has six elements across the PFZ which means that it is able to capture some gradients within the PFZ. The mesh was only validated for the isotropic material model, due to the high computational time required to run simulations with the crystal plasticity model. One crystal plasticity analysis (using the mesh `cube-20-16-6`), typically lasted for about 150 CPU hours using a Linux cluster (see appendix D for detailed information about the required CPU time). Considering the time limit of a master thesis, a priority was given to study the effect of grain orientation rather than mesh refinement.

6.6 Results and discussion: The isotropic plasticity model

In this section the results from the finite element analyses using isotropic plasticity will be presented. A discussion of how these results influence the competition between intergranular and transgranular fracture will be given in section 6.8.

6.6.1 The maximum and average effective plastic strain

Figure 6.14 show the maximum and average effective plastic strain for the grain interior and in the PFZ when the model is loaded in uniaxial tension. The model is here assigned the benchmark material ($\alpha = 0.50$ & $\beta = 3$).

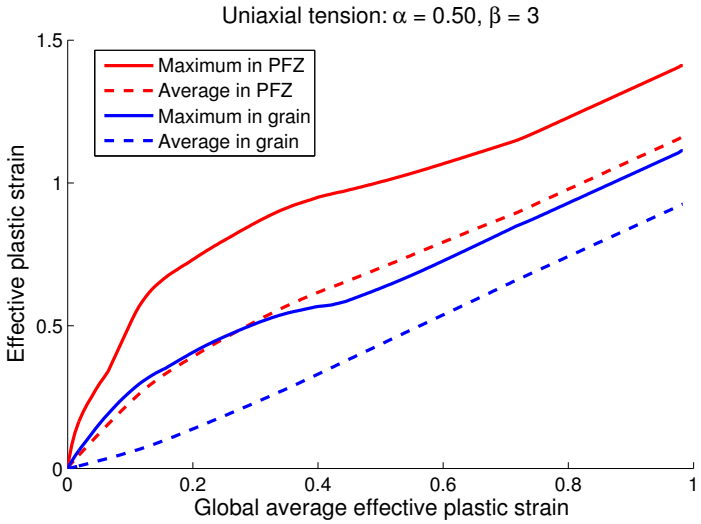

Figure 6.14: *The maximum and average effective plastic strain for the grain interior and the PFZ, when the model is loaded in uniaxial tension. The benchmark material is used.*

The average effective plastic strain for the PFZ is higher than for the grain interior. This is consistent with the results obtains in e.g. the PhD by Scheylvaerts [35]. It can be noticed that the maximum effective plastic strain in the PFZ, is located at the grain boundary which is slanted with respect to the external load. The details in how the effective plastic strain and the stress triaxiality are distributed will be discussed later.

The slope of the average effective plastic strain in the PFZ is decreasing whereas the slope of the average effective plastic strain in the grain interior is increasing. This is probably due to the difference in work hardening rate between the grain interior and the PFZ. The hardening rate in the PFZ is three times what it is in the grain interior. This means that the difference in strength between the zones will decrease as the global strain increase. The PFZ will eventually become the hardest zone. The influence of the hardening rate in the PFZ on the difference in average effective plastic strain between the grain interior and the PFZ will be discussed later.

For both the grain interior and the PFZ, the difference between the maximum and average effective plastic strain reaches a maximum value around a global average effective plastic strain of 0.3. The location of the maximum effective plastic strain will experience a higher hardening than the rest of the material. This means that the concentration of the plastic strain should become less narrow as the global strain increase. The difference between the maximum and average effective plastic strain is approximately equal in the grain interior and in the PFZ respectively.

Figure 6.15 and 6.16 show the maximum and average effective plastic strain in the grain interior and in the PFZ for the shear mode and the biaxial tension mode respectively.

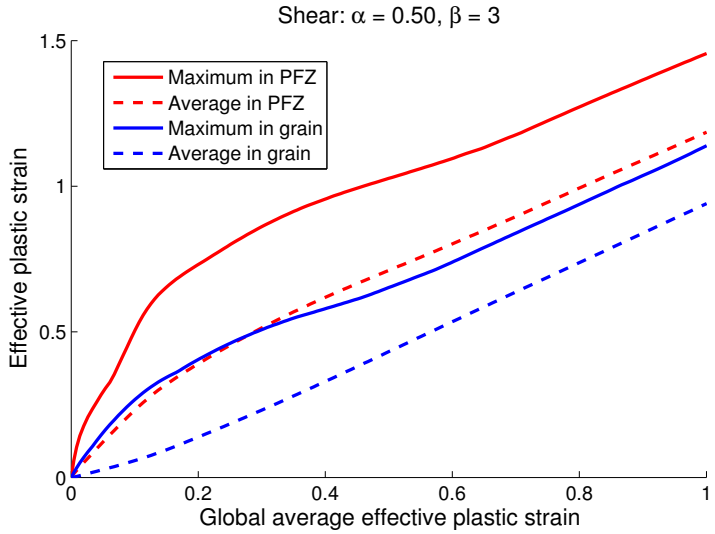

Figure 6.15: *The maximum and average effective plastic strain for the grain interior and the PFZ, when the model is loaded in shear. The benchmark material is used.*

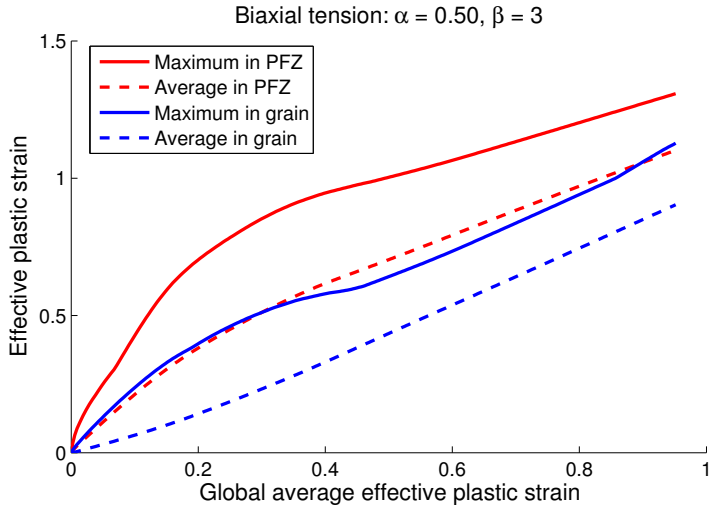

Figure 6.16: *The maximum and average effective plastic strain for the grain interior and for the PFZ, when loaded in biaxial tension. The benchmark material is used.*

Similar conclusions can be drawn for shear and biaxial tension as for uniaxial tension. In

the following, the shear mode will therefore be studied in more details. In section 6.7, the uniaxial tension mode will be used to compare the crystal plasticity model and the isotropic plasticity model.

In figure 6.17, the effect of work hardening rate in the PFZ on the average effective plastic strain in the grain interior and in the PFZ is shown.

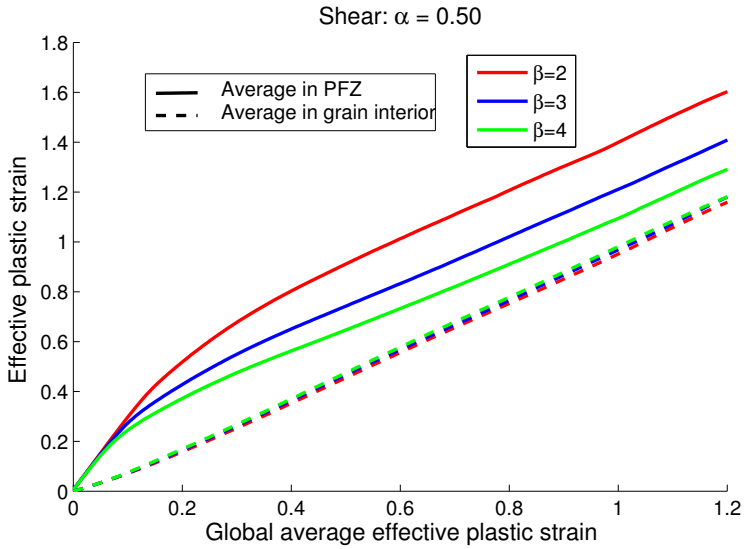

Figure 6.17: *The average effective plastic strain in the PFZ and the grain interior for various values of β.*

When the hardening modulus in the PFZ increase, the average effective plastic strain in this zone decreases. The hardening modulus in the PFZ seems to have less effect on the average effective plastic strain in the grain interior. However, as the hardening modulus in the PFZ increase, the average effective plastic strain in the grain interior increases slightly. The reason why the average strain in the grain interior is less affected by the hardening modulus in the PFZ, is probably that the volume fraction of PFZ is small compared to the grain interior.

In figure 6.18, the effect of work hardening rate on the maximum effective plastic strain in the grain interior and in the PFZ is shown. The ratio between the hardening rate in the PFZ and the grain interior is specified by the parameter $\beta = \frac{E_t^{PFZ}}{E_t^g}$, as discussed in section 6.4.2. It is clear that as the hardening modulus in the PFZ increases, the maximum effective plastic strain in this zone decrease. For high values of β, the maximum effective plastic strain in the PFZ approach the maximum level in the grain interior.

The maximum effective plastic strain in the grain interior also decrease with increasing β. Since the global average effective plastic strain is the same for all the tests, it could be expected that when the maximum level in the PFZ was decreasing, the maximum level in the grain would increase. However, this is clearly not the case. This effect will be further discussed after a more in depth study of the distribution of stresses and strains in the model (see section 6.6.2).

In order to fully understand the interaction between the grain interior and the PFZ it is

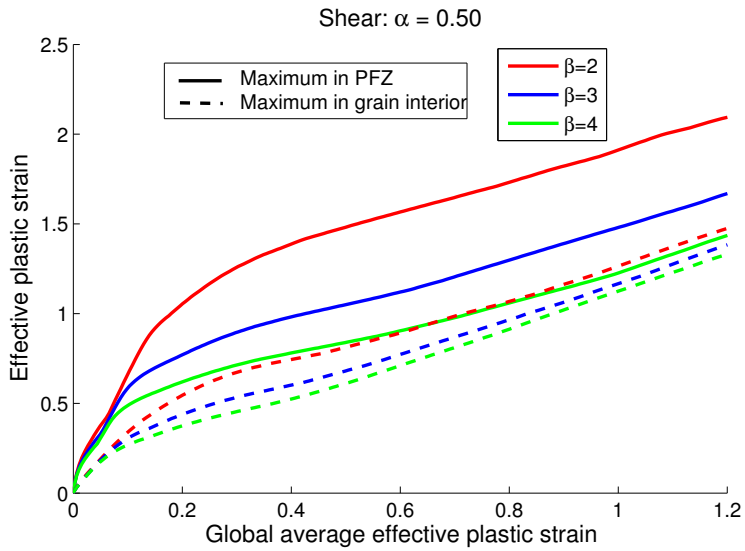

Figure 6.18: *The maximum effective plastic strain in the PFZ and the grain interior for various values of β.*

necessary to study more in depth the distribution of stresses and strains in the model. This is carried out in the subsequent section.

6.6.2 The distribution of plastic strains

To investigate how the plastic strains are distributed, some points of interest have been defined. These points are shown in figure 6.19 and are similar to those used in the PhD thesis of Scheylvaerts [35]. The points 1, 2 and 3 are located at the grain boundary in the center of the PFZ, the points 4, 5 and 6 are located in the grain interior next to the PFZ, and point 7 is located in the center of the grain.

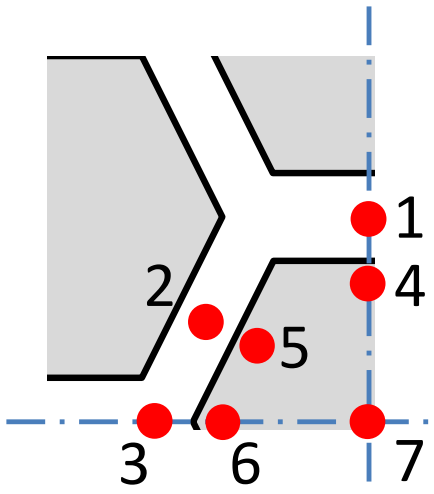

Figure 6.19: *Location of the sampling points.*

In figure 6.20, the effective plastic strains in the three points at the grain boundary are shown.

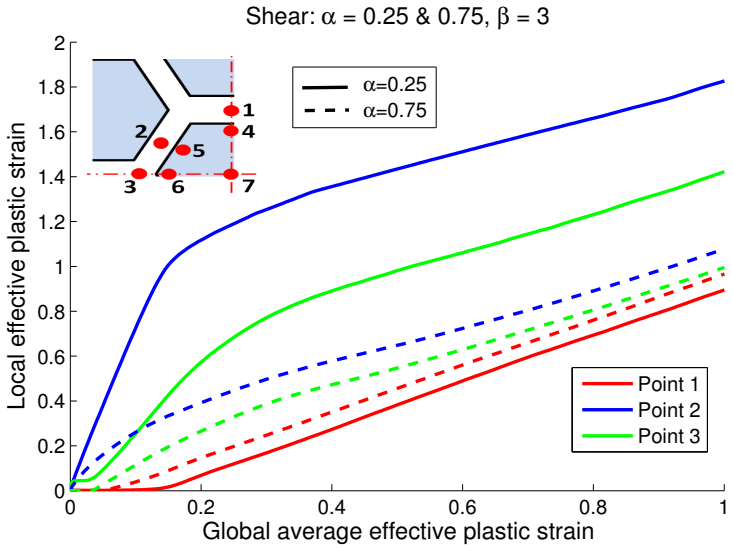

Figure 6.20: *Local effective plastic strain for points at the grain boundary.*

The effective plastic strain in the points 2 and 3 decreases as the yield stress in the PFZ increases (see figure 6.20). However, point 1 show the opposite trend.

The slope of the effective plastic strain curve for points 2 and 3 decreases at a global average plastic strain of about 0.15-0.2. This decrease is consistent with what was observed for the maximum effective plastic strain in the PFZ (see e.g. figure 6.18). Point 1 is located in the horizontal grain boundary and the slope of the maximum effective plastic strain curve for this point increases. The horizontal grain boundary in particular will be treated in the paragraph entitled: "The horizontal grain boundary".

Since point 4 is located in the grain interior next to point 1, it could be expected that the effective plastic strain in this point would be the lowest among the points in the grain interior. In figure 6.21 and 6.22 it is clear that point 4 is not the one to flow the least among the points in the grain interior. Figure 6.22 illustrates that the spread in effective plastic strain among the points in the grain interior is decreasing when the yield stress in the PFZ is increasing. The reduced spread is caused by an increase in the effective plastic strain in the points 4, 5 and 6, while the effective plastic strain in point 7 is almost unchanged.

When the yield stress in the PFZ is low ($\alpha = 0.25$), the center of the grain (point 7) generally have a higher effective plastic strain than the points in the vicinity of the PFZ. At point 7, the effective plastic strain is close to the global average. The plasticity starts to rise close to the PFZ at a global average effective strain of about 0.15-0.2. At the same global strain level the slope of the effective plastic strain in point 2 and 3 was decreasing (see figure 6.20).

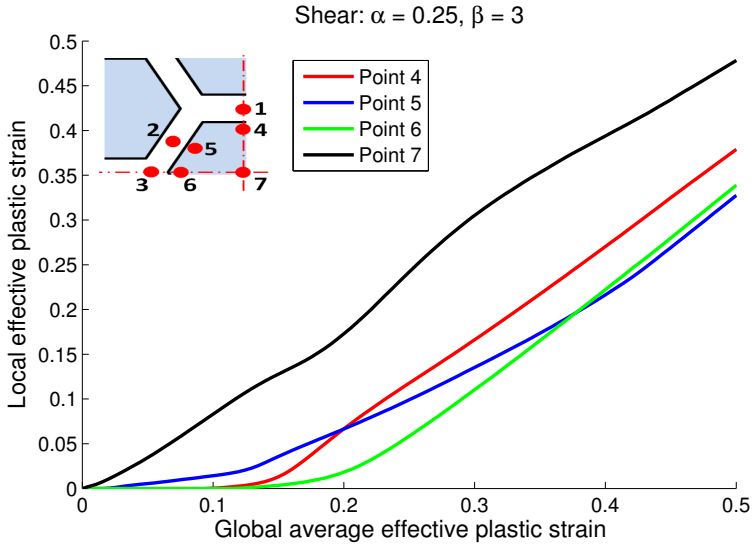

Figure 6.21: *The local effective plastic strain in the grain interior for low alpha value.*

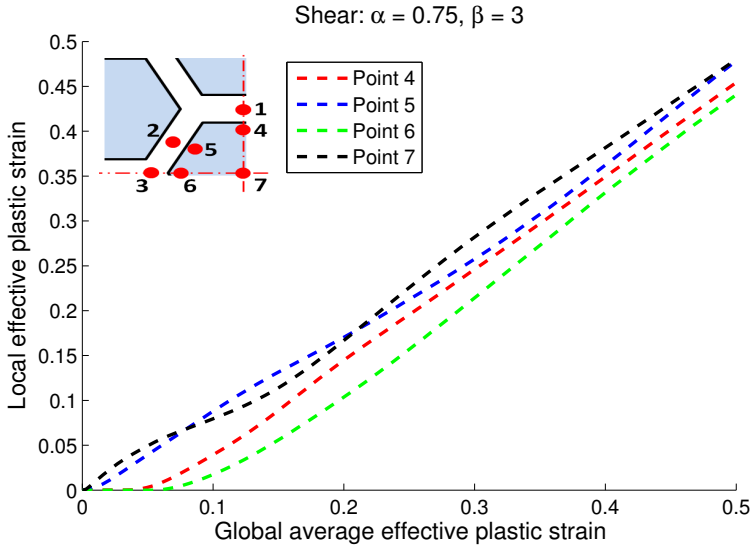

Figure 6.22: *The local effective plastic strain in the grain interior for high alpha value.*

The reason why the effective plastic strain is low near the slanted PFZ might be connected to the orientation of the PFZ combined with the difference in yield stress between the grain interior and the PFZ. Figure 6.23 illustrates the distribution of effective plastic strain for the shear mode. The other modes show a similar distribution (see figure B-2 and B-3 in appendix B).

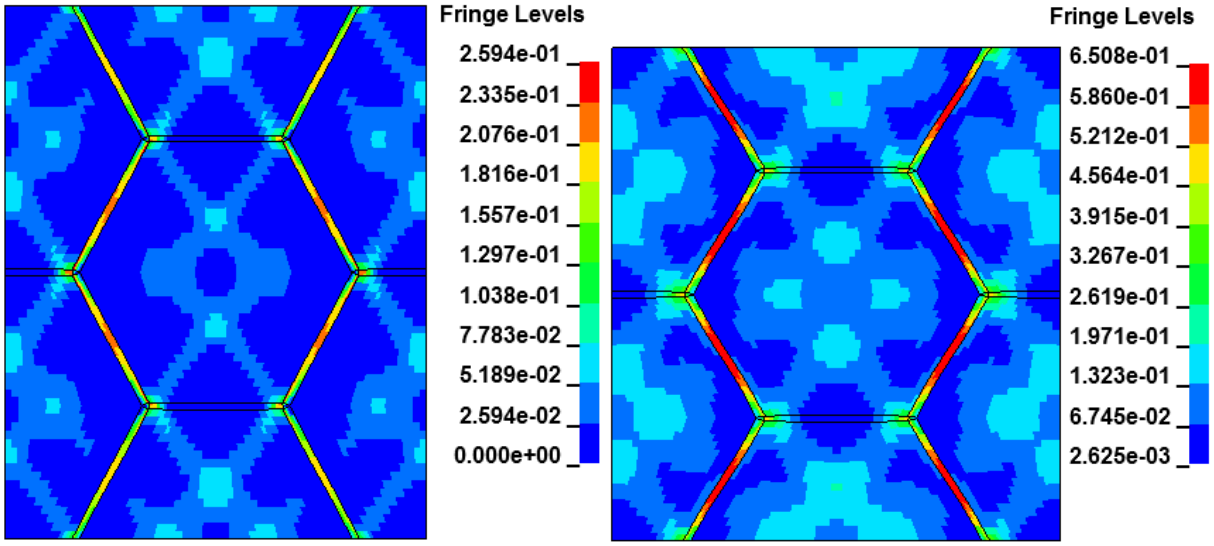

Figure 6.23: *Illustration of the distribution of effective plastic strain for the benchmark material loaded in shear. To the left for a global average effective plastic strain of* 0.04 *and to the right a global average effective plastic strain of* 0.15.

The effective plastic strain is concentrated in bands parallel to the direction of the maximum shear stress oriented at a 45° angle with respect to the global coordinate system. This is almost parallel to the slanted PFZ. For low global strains (left picture in figure 6.23) the yield stress of the PFZ is much lower than in the grain interior and the effective plastic strain is concentrated in the slanted PFZ. For higher global effective plastic strains, the shear band can be observed crossing the slanted PFZ (see the right picture in figure 6.23).

In the grain interior the effective plastic strain is also concentrated along bands oriented at 45° with the global coordinate system. These bands do not go directly through the center of the grain, but pass closely on each side. The plastic strains are concentrated in four points, where these bands intersect. When the global deformation increases, the radius of these high concentration zones increases until eventually the plasticity has spread all over the grain interior. The locations of the bands seem to be closely related to the geometry of the grain and are therefore regular. Introducing random grain shapes could enable to observe a unique localization of plastic strains within each grain.

The local effective plastic strain at the seven sample points for the benchmark material when loaded in uniaxial tension is given in appendix B. The trends are the same for uniaxial tension as for shear.

The horizontal grain boundary

The effective plastic strain near and inside the horizontal grain boundary is plotted against global average effective plastic strain in figure 6.24. The difference between the effective plastic strain in point 1 and 4 seems to be small, regardless of the parameter α. When the yield stress in the PFZ is increased, the local effective plastic strain increases both in point 1 and 4.

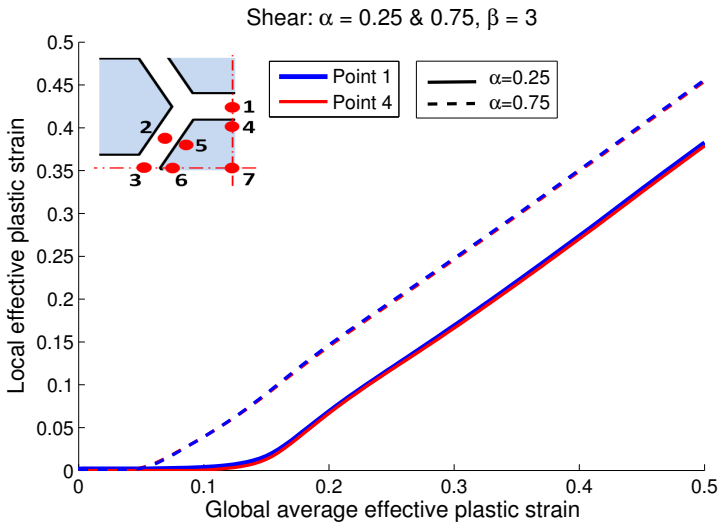

Figure 6.24: *Local effective plastic strain in point 1 and 4 for different values of α.*

The reason why the horizontal PFZ experience low effective plastic strain for the shear mode might be connected to its orientation, and the interaction with the grain interior. Figure 6.25 illustrated a segment of the horizontal PFZ.

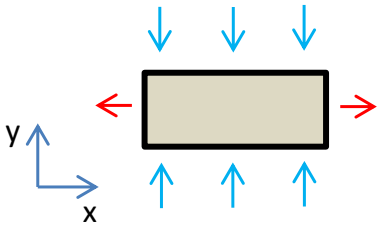

Figure 6.25: *Segment of a horizontal grain boundary. The blue arrows illustrate the compressive stresses due to the imposed displacement in the y-direction. The red arrows illustrate the strain parallel to the length of the horizontal grain boundary.*

The displacement of the top of the model will impose compressive stresses in the y-direction at the horizontal grain boundary. At the horizontal grain boundary, these compressive stresses will cause a negative strain in the y-direction. Due to the Poisson effect, the strain in the y-direction will cause a positive strain in the x-direction. As long as the horizontal grain boundary and grain interior are elastic, the grain interior and the PFZ will experience the same strain field. The grain interior will therefore not restrict deformation of the horizontal grain boundary.

Since the yield stress of the PFZ is lower than in the grain interior, the horizontal PFZ will yield at a lower stress than the grain interior. Once yielding is initiated in the horizontal PFZ, the law of conservation of volume dictate a higher strain in the x-direction than prior to yielding. Since the grain interior is still elastic, it will restrict a higher strain in the x-direction of the horizontal PFZ due to no slip condition at the grain interior PFZ interface. This will result in a lower deviatoric stress at the horizontal grain boundary.

The maximum effective plastic strain in the grain interior

It was observed in figure 6.18 that as the work hardening rate in the PFZ decreases, the maximum effective plastic strain in the grain interior increases. The location of the maximum effective plastic strain in the grain interior is illustrated in figure 6.26. Consider first only the imposed displacement in the x-direction, which is equivalent to the uniaxial tension mode. This displacement will lead to a generally positive strain in the x-direction. As observed earlier, the plastic strain will be concentrated in the slanted PFZ for the uniaxial tension mode. The plastic strain in x-direction in the slanted PFZ, may lead to a concentration of tensile stresses in the x-direction in the grain interior where the maximum effective plastic strain is located (see figure 6.26). If this is true, the stress concentration will increase when the plastic strain in the slanted PFZ increases.

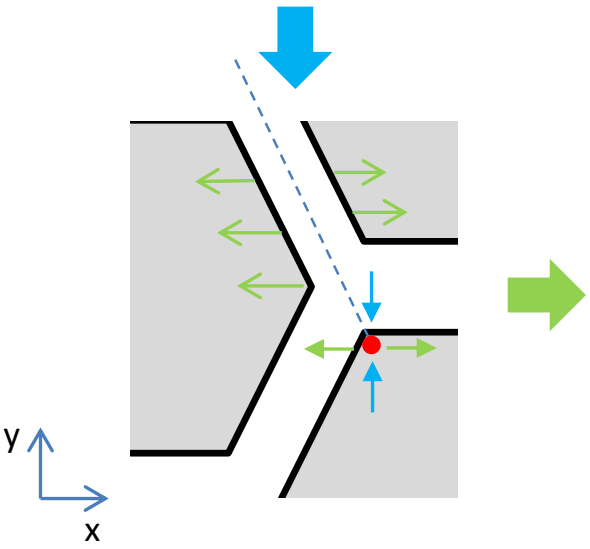

Figure 6.26: *The upper left quarter of the model loaded in shear. The blue arrows represent the displacement of the top leading to compressive forces in the y-direction at the red point. The thin green arrows illustrate the deformation of the slanted PFZ, leading to tensile forces in the x-direction at the red point, contributing to increase the effective plastic strain.*

It was observed that when the yield stress and the work hardening rate of the PFZ are decreased, the plastic strain in the x-direction in the slanted PFZ increases. This should then lead to higher tensile stresses in the x-direction at the point in the grain interior where the maximum effective plastic strain is located.

The displacement in the y-direction for the shear mode will lead to generally compressive stresses in the y-direction all over the model. This means also at the point in the grain interior where the maximum effective plastic strain is located. When both the x and y displacement are applied, the concentration of the plastic strain is still located in the slanted PFZ. This could indicate that a higher plastic strain in the slanted PFZ, also for the shear mode, will contribute to reduce the compressive stresses in the x-direction at the point in the grain interior where the maximum effective plastic strain is located, increasing the deviatoric stress. Hence a higher maximum effective plastic strain in the PFZ will cause a higher maximum effective plastic strain in the grain interior. This is consistent with the results from the simulations.

6.6.3 The distribution of stress triaxiality

The literature study of fracture mechanisms uncovered that the stress triaxiality ratio is an important measure with respect to initiation of ductile fracture (see section 4.1). In this section the distribution of stress triaxiality for the shear mode will be investigated. How the results apply to the initiation of ductile fracture will be discussed in section 6.7.

Figure 6.27 illustrates the evolution of the stress triaxiality ratio in the sampling points at the grain boundary. The stress triaxiality ratio in the sampling points for the entire loading history is given in figure B-6 and B-7 in appendix B. For global average effective plastic strains above 0.2 the stress triaxiality ratio continues to drop in all the sampling points.

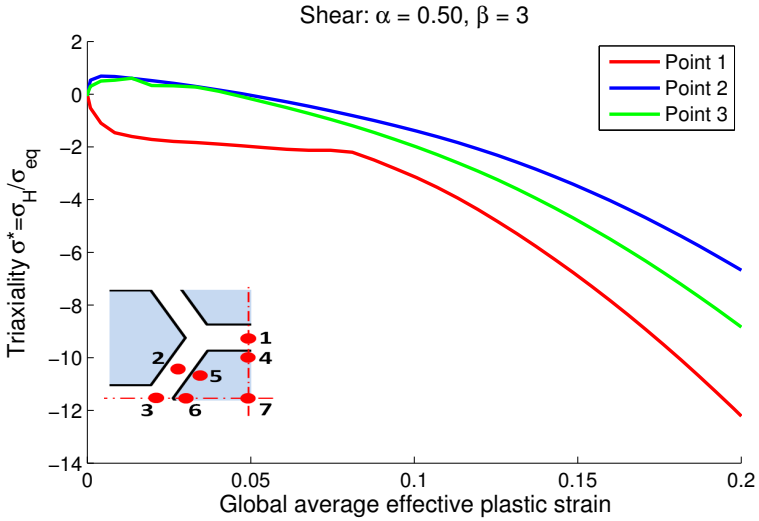

Figure 6.27: *Stress triaxiality ratio in the points at the grain boundary.*

There is a clear tendency that point 1 which is located at the horizontal grain boundary has the most negative stress triaxiality ratio. For global average effective plastic strains above ca. 0.03, point 3 has more negative stress triaxiality ratio than point 2.

The stress triaxiality ratio at the sample points in the grain interior is shown in figure 6.28. The distribution of stress triaxiality within the grain interior has less spread than in the PFZ. The stress triaxiality ratio is slightly more negative near the PFZ than in the center of the grain.

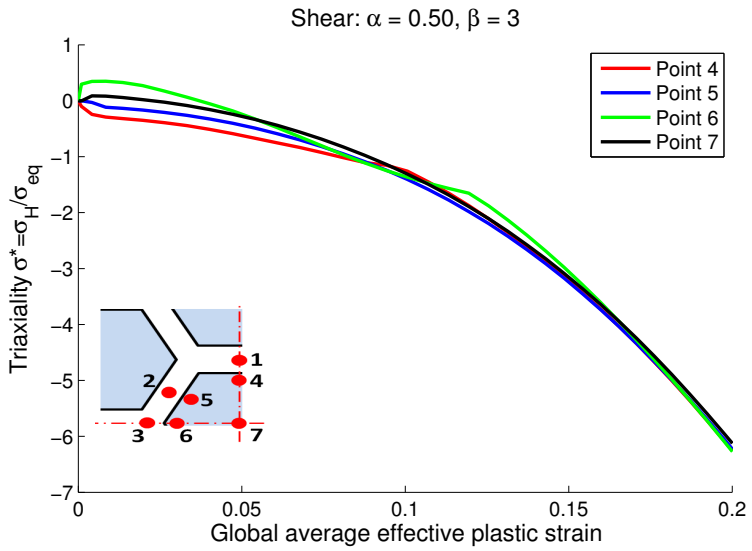

Figure 6.28: *Stress triaxiality ratio for the points in the grain interior.*

The figure shows that the points 4, 5 and 6 have more negative stress triaxiality ratio than the center of the grain (point 7).

Figure 6.29 shows how the stress triaxiality is distributed at a global average effective plastic strain of 0.01.

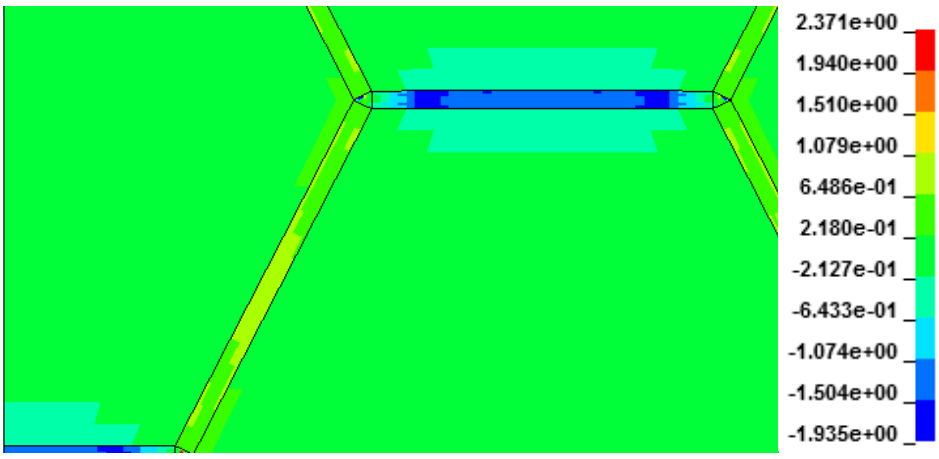

Figure 6.29: *The distribution of stress triaxiality at a global average effective plastic strain of* 0.01.

At this low global strain the stress triaxiality ratio within the grain is of a magnitude $\pm 2 \cdot 10^{-1}$. The stress triaxiality ratio at the horizontal grain boundary is already negative. The reason for the high negative stress triaxiality ratio in the horizontal PFZ for the

shear mode may be connected to the interaction between the horizontal PFZ and the grain interior. A possible reason for why the effective plastic strain in the horizontal PFZ is low was discussed in section 6.6.2 and was connected to the difference in yield stress between the grain interior and the PFZ. The reason for the high negative stress triaxiality in the horizontal PFZ might be connected to the same phenomenon.

The distribution of σ_{xx} and σ_{yy} near and within the horizontal PFZ for a global average effective plastic strain of 0.01 is shown in figure 6.30. At this global strain level, the stress triaxiality ratio in the sample point at the horizontal grain boundary is approximately -1.5 (see figure 6.27). The displacement of the top of the model in the negative y-direction will lead to compressive stresses in the y-direction at the horizontal PFZ (see figure 6.30(b)). The grain interior, opposing the strain along the longitudinal axis of the horizontal PFZ, will impose compressive stresses in the x-direction (see figure 6.30(a)). This might contribute to increase the compressive hydrostatic stress in the horizontal PFZ. For low plastic strains the yield stress in the PFZ is low compared to in the grain interior which means that the von Mises stress in the horizontal PFZ is low. This might result in a high negative stress triaxiality ratio.

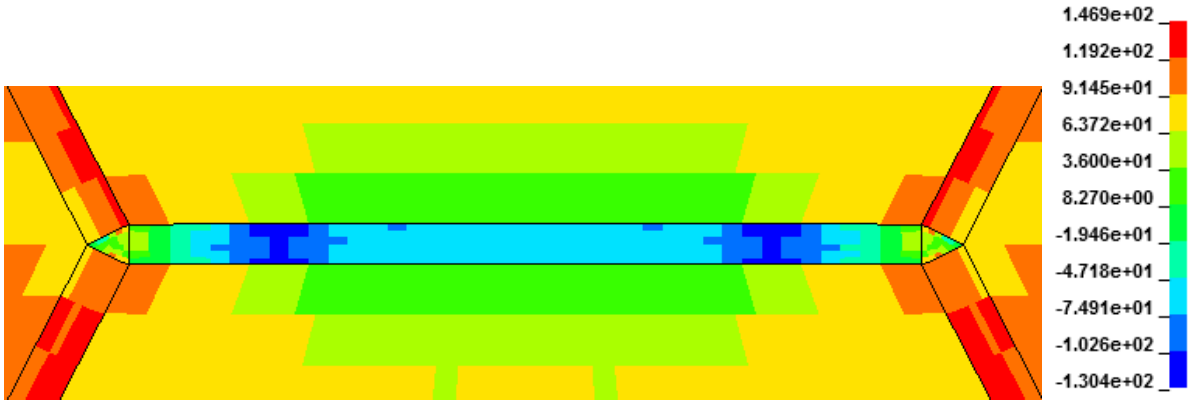

(a)

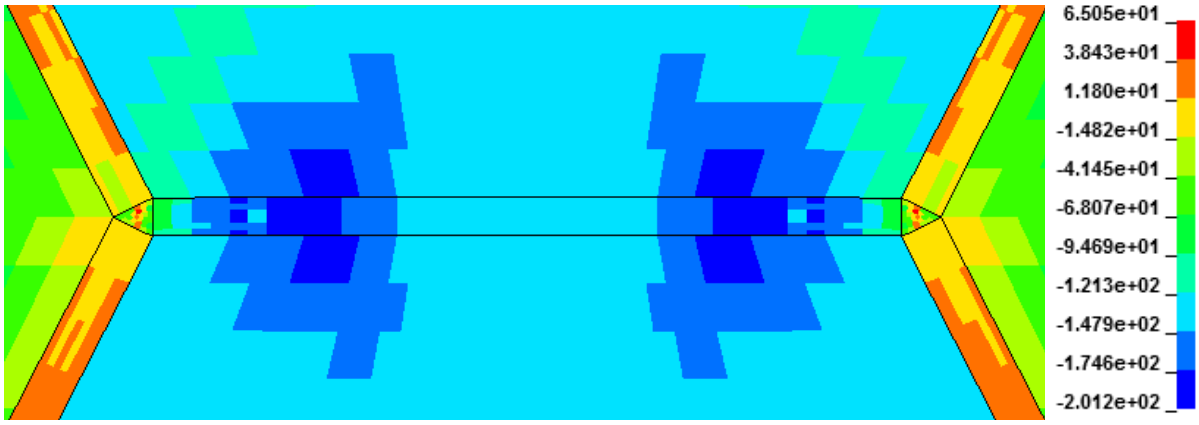

(b)

Figure 6.30: *(a) the σ_{xx} [N] distribution and (b) the σ_{yy} [N] distribution near and within the horizontal PFZ for a global average effective plastic strain of 0.01.*

6.7 Results and discussion: The crystal plasticity model

In this section the results from the crystal plasticity analyses will be presented and compared to the isotropic plasticity analyses.

The maximum and average effective plastic strain in the PFZ for uniaxial tension is plotted in figure 6.31. Using isotropic plasticity, the average effective plastic strain in the PFZ is generally higher then when using crystal plasticity. The crystallographic orientations of the grains seem to have minor influence on the average effective plastic strain. However, the maximum effective plastic strain in the PFZ calculated with crystal plasticity, is influenced more than the average by the grain orientations. This could indicate local activation of certain slip systems giving concentration of plastic strain depending on the crystallographic orientations.

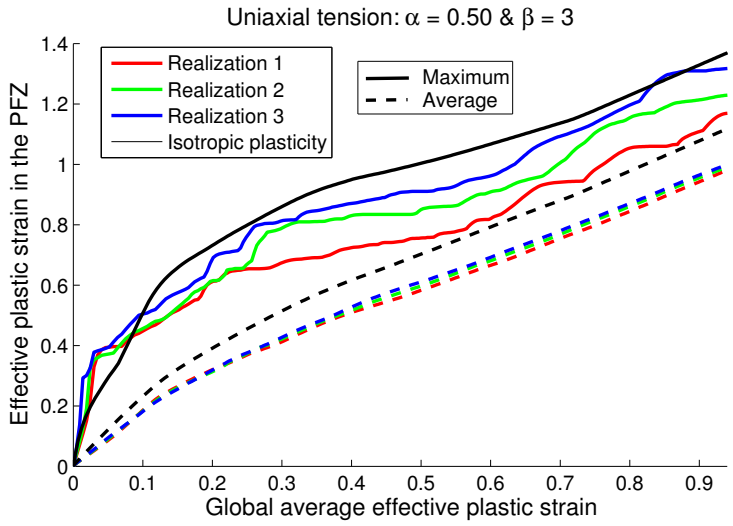

Figure 6.31: *Uniaxial tension. Maximum and average effective plastic strain in the PFZ for crystal and isotropic plasticity.*

For global average effective plastic strains above 0.1, the maximum effective plastic strain in the PFZ is higher when using isotropic plasticity than when using crystal plasticity. The only exception is realization 3, which predicts a higher maximum effective plastic strain than the isotropic plasticity model at a global average effective plastic strain of approximately 0.85. For low global plastic strains (< 0.1), all the crystal plasticity realizations predict a higher maximum effective plastic strain in the PFZ than the isotropic plasticity model. The reason might be that some slip systems are especially susceptible to slip. Also the realizations are drawn from a cube texture with crystallographic orientations within $\pm 15°$. The sharp texture could explain the low spread at low global strains. However, this should have been checked by the calibration of the crystal plasticity model.

Another possibility is that the high concentration of plastic strain in the PFZ, for low

global strains, is due to the interaction between the PFZ and the grain interior. For low global strains, the PFZ is soft compared to the grain interior. Since the grains are anisotropic, deformation within the grain interior occur preferably in certain directions. The same is the case for the PFZ, however since this zone is given lower yield stress than the grain interior, it is the first to deform plastically. The grain interior's superior yield stress for low global strains, combined with its anisotropy, may contribute to increasing the plastic strain in the PFZ. The interaction between a soft and a hard zone was not investigated during the calibration of the crystal plasticity model.

Yet another possibility is related to the number of possible slip directions. The crystallographic orientation is uniform within each grain, whereas multiple crystallographic orientations meet within the PFZ. This could indicate that the PFZ is more free to deform. However, this could also have the opposite effect, since no slip system is continuous through the PFZ. A more extensive study is required before conclusions are drawn.

Figure 6.32 present the maximum and average effective plastic strain for the grain interior when the model is loaded in uniaxial tension. Here the trend is somewhat different than in the PFZ. The maximum effective plastic strain for the crystal plasticity model is lower than for the isotropic model for small global plastic strains (< 0.2). For higher global plastic strains (> 0.2), the maximum effective plastic strain using the isotropic plasticity model is no longer higher than all the realizations of the crystal plasticity model. The spread in the maximum effective plastic strain in the grain interior is similar to what was observed for the PFZ. The high variation of maximum effective plastic strain for different realizations of the grain orientations might be due to local activation of certain slip systems at high global strains. Note that the realization which predicted the highest maximum strain in the PFZ, realization 3, also predict the highest maximum strain in the grain interior.

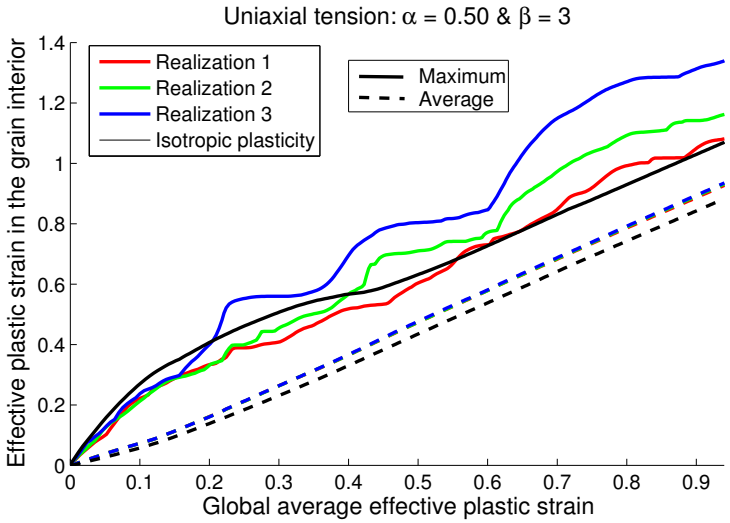

Figure 6.32: *Uniaxial tension. Maximum and average effective plastic strain in the grain interior for crystal and isotropic plasticity.*

The average effective plastic strain in the grain interior for the isotropic model is generally

lower than for the crystal plasticity model. This is opposite of what was seen in the PFZ, which means that the difference between the average effective plastic strain in the grain interior and in the PFZ is lower when using crystal plasticity than when using isotropic plasticity.

For the model using isotropic plasticity, some areas within the grain have zero plastic strain. However, for the crystal plasticity model once plasticity is initiated within the grain there are no areas which remain elastic. This might be the reason why the average effective plastic strain in the grain interior is higher when using crystal plasticity than when using isotropic plasticity. In the PFZ, the average effective plastic strain when using crystal plasticity was lower than when using isotropic plasticity. This might be explained by the same effect. The area of the grain interior is higher than the area of the PFZ. When the average effective plastic strain in the grain interior increase, the effective plastic strain in the PFZ must be reduced because the weighted average have to remain the same.

Another possible reason for the differences observed in the effective plastic strain might be that the calibration of the crystal plasticity model is incorrect. To check if this the case, applied force versus global average effective plastic strain is plotted in figure 6.33. The force displacement curve show the same trend and is given in appendix C figure C-1.

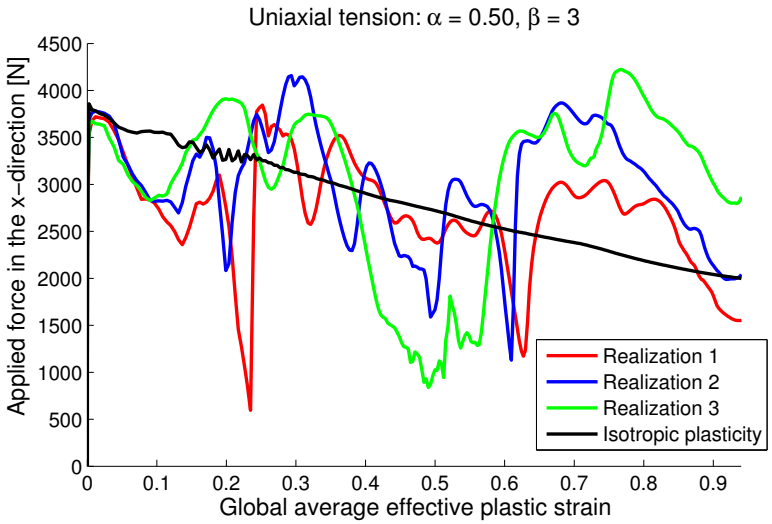

Figure 6.33: *Applied force at right boundary plotted against global average effective plastic strain for uniaxial tension and benchmark material.*

Consider the isotropic plasticity model. Note that the applied force decrease as the global average effective plastic strain increase. The reason might be that necking occurs once plasticity occur in the grain interior. The hardening rate of the grain interior is set to 40 MPa and the yield stress is set to 200 MPa. Considère's criterion for necking gives:

$$\frac{\mathrm{d}\sigma}{\mathrm{d}\varepsilon} = \sigma \tag{6.18}$$

$$\frac{\mathrm{d}\sigma}{\mathrm{d}\varepsilon} = 40\,\mathrm{MPa} < 200\,\mathrm{MPa} = \sigma \tag{6.19}$$

The applied forces using the two material models are approximately equal prior to plasticity, which indicate that the shear and bulk modulus as well as the yield stress in the PFZ are correct. After yielding occur somewhere in the model, the applied force drops faster when using crystal plasticity than when using isotropic plasticity. The slope of the force versus global average effective plastic strain curve for the model using crystal plasticity change at a global average effective plastic strain of about 0.1. This is the same global strain level as when the slope of the maximum effective plastic strain curve for the PFZ was decreasing rapidly (see figure 6.31). For global average effective plastic strains above 0.1, large fluctuations in the applied force can be observed when using crystal plasticity. The magnitudes of the fluctuations are approximately the same regardless of the grain orientations.

The fluctuations observed in figure 6.33 for the model using crystal plasticity, might be due to the high mass density. The mass density was set to $20.00\,\mathrm{kg/mm^3}$ for the isotropic plasticity model and $2.00\,\mathrm{kg/mm^3}$ for the crystal plasticity model. Since kinetic energy is proportional to the mass, the kinetic energy of the model using isotropic plasticity is expected to be ten times the kinetic energy of the model using crystal plasticity (see figure 6.34).

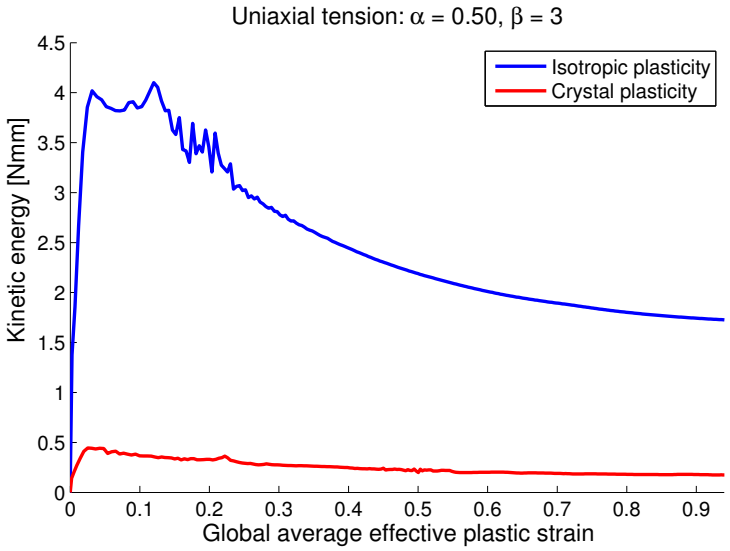

Figure 6.34: *The kinetic energy for the model using isotropic plasticity and the model using crystal plasticity, both loaded in uniaxial tension.*

The model using crystal plasticity do not experience oscillations up until a global average effective plastic strain of 0.94 (see the kinetic energy plotted in figure 6.35 for global average effective plastic strains above 0.94). Hence, the spread in the applied force observed in figure 6.33 is probably not due to the high mass density. The fluctuations

might be due to the activation of slip systems as the material deforms. When the grains deform, their geometry is changed and new slip systems might become active and reduce the required applied force.

For global average effective plastic strains above 0.94, the model using crystal plasticity starts to oscillate and eventually fails (see figure 6.35). Large oscillations in the global kinetic energy are observed. This might be due to limitations of the crystal plasticity material card for such high strains. The different realizations loaded in uniaxial tension failed at the same global strain. The results for global average effective plastic strains above 0.94 were rejected.

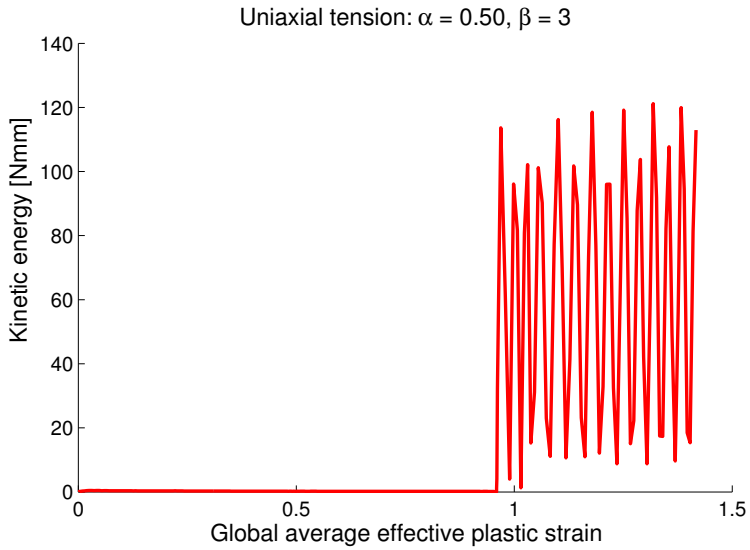

Figure 6.35: *Kinetic energy for realization 1 in uniaxial tension.*

Now consider the shear mode. The maximum and average effective plastic strain in the PFZ and the grain interior, are shown in figure 6.36 and 6.37 respectively. The trends both in the grain interior and in the PFZ are similar to what was observed for uniaxial tension. Note that the shear test is only plotted to a global average effective plastic strain of 0.55, since the analysis failed at this point. A test with a smaller uniform mass density ($2 \cdot 10^{-2}\,\mathrm{kg/mm^3}$, leading to a time step in the order of 10^{-6}), was carried out to see if too large time steps was the cause of failure. However, this had no effect and the analysis failed at the exact same point. No oscillations were observed in the kinetic energy prior to the failure (see figure C-2 in appendix C). At a global average effective plastic strain of 0.55, the pressure in the model is of the order of $-2 \cdot 10^4\,\mathrm{MPa}$. The high magnitude of the pressure might be the cause of the failure.

Now consider the biaxial tension mode. The maximum and average effective plastic strain in the PFZ and in the grain interior are shown in figure 6.38 and 6.39 respectively. The trends observed in these figures are similar to what was observed both for the uniaxial tension and the shear mode. In the following, it is therefore chosen to investigate the uniaxial tension mode more in detail.

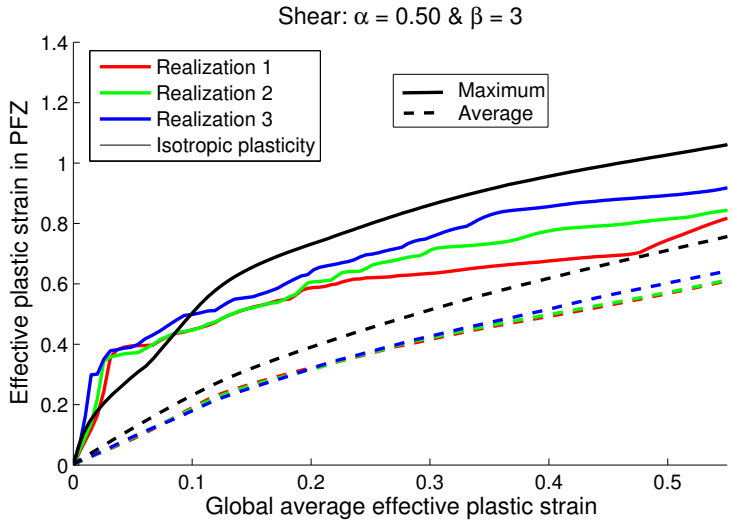

Figure 6.36: *Shear mode. Maximum and average effective plastic strain in the PFZ for crystal and isotropic plasticity.*

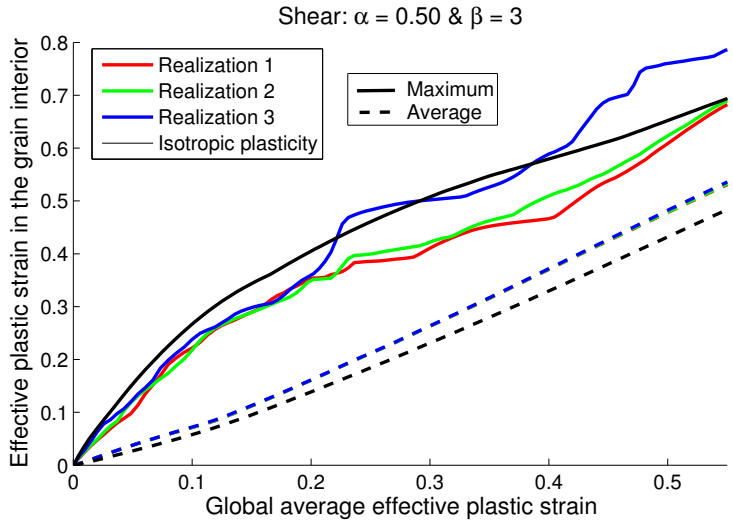

Figure 6.37: *Shear mode. Maximum and average effective plastic strain in the grain interior for crystal and isotropic plasticity.*

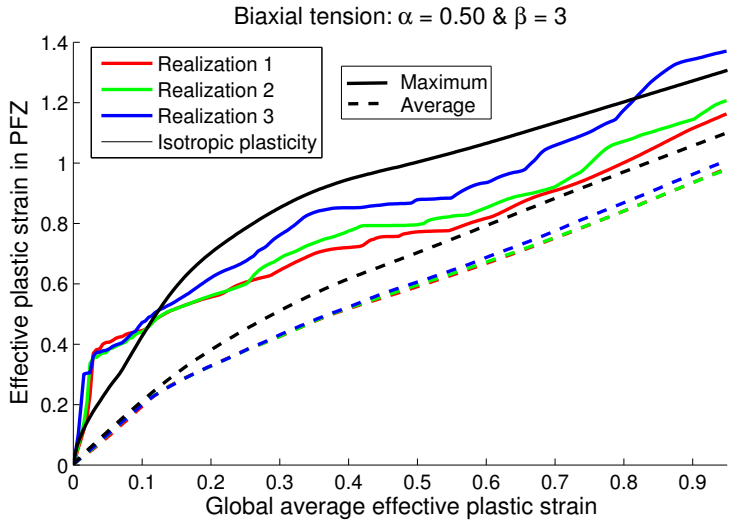

Figure 6.38: *Biaxial tension mode. Maximum and average effective plastic strain in the PFZ for crystal and isotropic plasticity.*

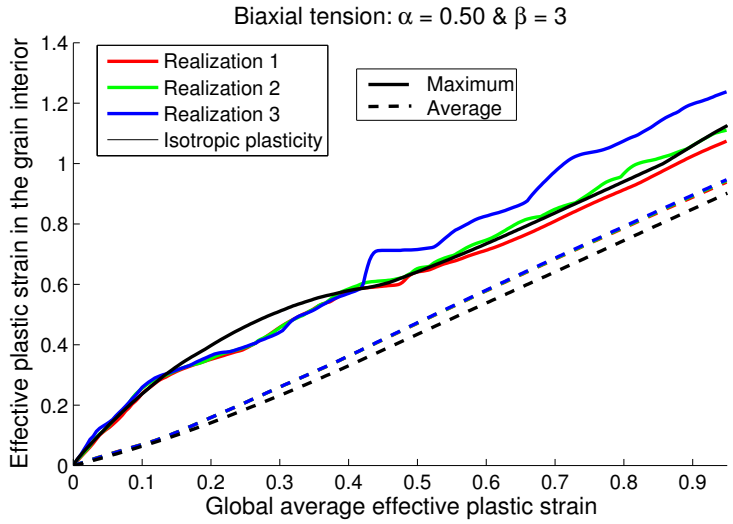

Figure 6.39: *Biaxial tension mode. Maximum and average effective plastic strain in the grain interior for crystal and isotropic plasticity.*

6.7.1 The distribution of stresses and strains

In this section, the distribution of stresses and strains in the model loaded in uniaxial tension is investigated further. The results from the crystal plasticity analyses presented here are limited to realization 1. Results for realization 2 and 3 are available in appendix C. The trends are similar for all the realizations.

Generally, the results from the crystal plasticity model show large fluctuations, which challenge the reliability of the result. A more extensive study with a higher number of realizations of the crystallographic grain orientations should be carried out, before conclusions are drawn regarding whether the trends observed here are consistent.

In figure 6.40, the effective plastic strains in the three points at the grain boundary are plotted for both the crystal and the isotropic plasticity model. At a global average effective plastic strain of about 0.1-0.15, point 3 experiences higher effective plastic strain when using crystal plasticity than when using isotropic plasticity. Whether the magnitude of the effective plastic strain in point 3 at this stage is critical with respect to fracture will be discussed in section 6.8. In point 2, the isotropic plasticity model generally predicts a higher effective plastic strain than the crystal plasticity model. Which is consistent with the observation for the average effective plastic strain in the PFZ (see figure 6.31).

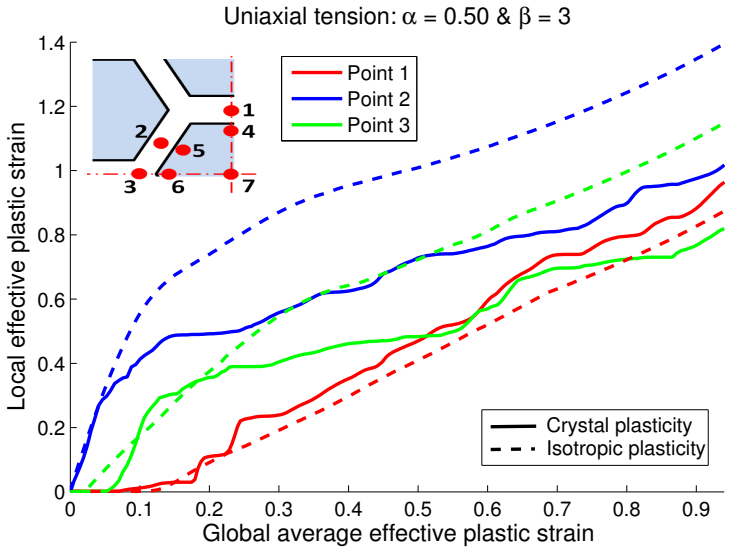

Figure 6.40: *Comparison between the effective plastic strain in points at grain boundary for crystal plasticity realization 1 and isotropic plasticity.*

In point 1 which is located at the horizontal grain boundary, the trend is opposite from what was observed in point 2 and 3. The reason might be that the horizontal PFZ is restricted against deformation by the grain interior or it might be that the grain interior carries most of the load. As observed in figure 6.32 the average effective plastic strain in the grain interior is generally higher using crystal plasticity than when using isotropic plasticity. The horizontal PFZ may therefore experience a higher plastic strain even if it is restricted by the grain interior.

Using isotropic plasticity, it was found that the effective plastic strain in the grain interior near the slanted PFZ was increasing when the effective plastic strain in the PFZ was decreasing. The decrease in effective plastic strain in the PFZ was due to higher yield stress and work hardening rate. If the same apply when using crystal plasticity, it is to be expected that the effective plastic strain in point 5 and 6 is higher when using crystal plasticity than when using isotropic plasticity. A comparison between the effective plastic strain in the points 4, 5, 6 and 7 when using isotropic plasticity and when using crystal plasticity is given in figure 6.41 and 6.42.

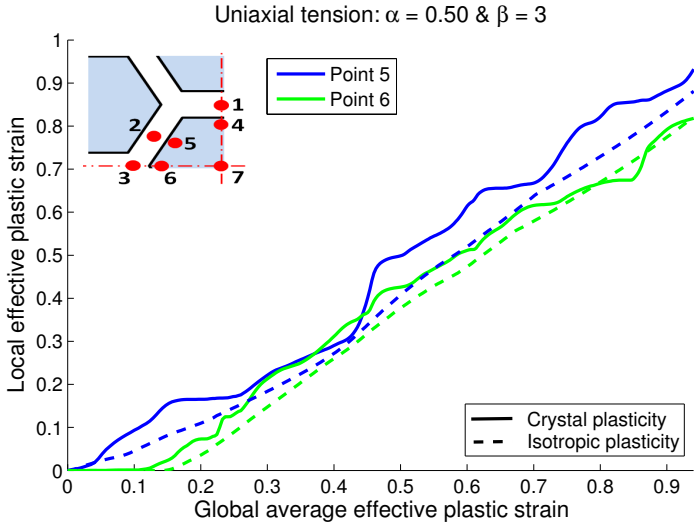

Figure 6.41: *Comparison between the effective plastic strain at point 5 and 6 for crystal and isotropic plasticity.*

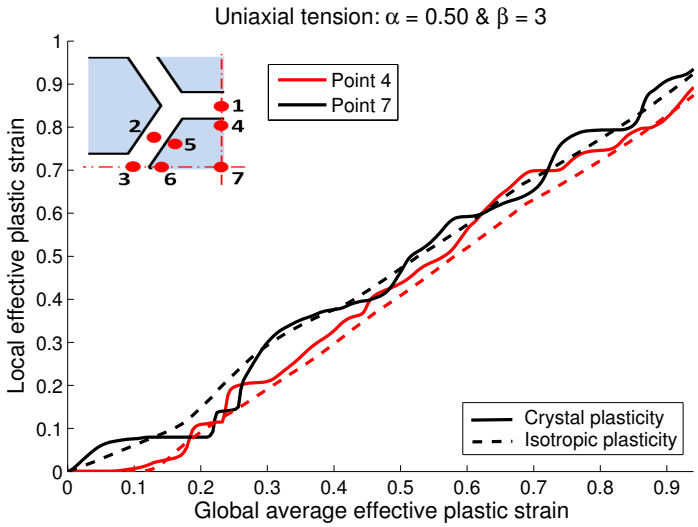

Figure 6.42: *Comparison between the effective plastic strain at point 4 and 7 for crystal and isotropic plasticity.*

In figure 6.41, the effective plastic strain in both point 5 and 6 when using crystal plasticity are for the most part higher than when using isotropic plasticity. This is consistent with

what was expected based on the results for the isotropic plasticity analysis.

The effective plastic strain in points 4 and 7 experience large fluctuations (see figure 6.42). The effective plastic strain in these points for realization 2 and 3 fluctuate even more (see appendix C). For that reason it is difficult to determine how the effective plastic strain in the points 4 and 7 is influenced by crystal plasticity.

When using isotropic plasticity a clear trend was observed with respect to the distribution of effective plastic strain in the points in the grain interior (see figure 6.21 and 6.22). In order to see if the same can be observed using crystal plasticity, the effective plastic strain for the four points in the grain interior is plotted in figure 6.43. The trend is not as clear when using crystal plasticity as when using isotropic plasticity.

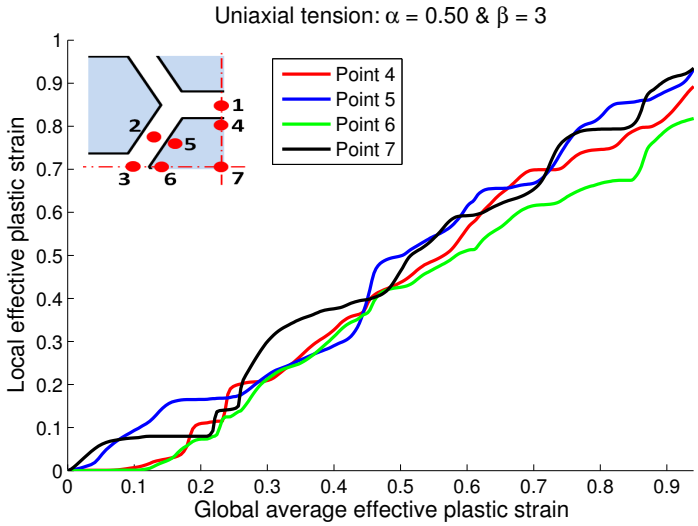

Figure 6.43: *The effective plastic strain for the points in the grain interior using crystal plasticity realization 1. The benchmark material parameters are used.*

For the uniaxial tension mode, the stress triaxiality ratio in the sampling points when using isotropic plasticity is shown in figure 6.44. Some oscillations are observed for a global average effective plastic strain of about 0.15-0.25. The kinetic energy did show some oscillations in this global strain region (see figure 6.35). However, the oscillations in kinetic energy where decaying for higher global strains.

The stress triaxiality ratio in all the points using isotropic plasticity approach ca. 0.6 for high global strains (see figure 6.44). It was expected that the global stress triaxiality ratio of the plane strain uniaxial tension mode should be higher than for pure uniaxial tension, which has a stress triaxiality ratio of 1/3 [41]. The stress triaxiality ratio is positive which means that it could lead to void growth. For the shear mode, the stress triaxiality ratio was generally negative when using isotropic plasticity. A negative stress triaxiality ratio will decreased the risk of void growth. Note especially that the stress triaxiality ratio in the horizontal grain boundary is positive for the uniaxial tension mode. This means that even if the effective plastic strain at this location was low, it might still be a candidate for initiation of ductile fracture. When the model was loaded in shear, the horizontal grain boundary was restricted against large plastic strains and experienced a

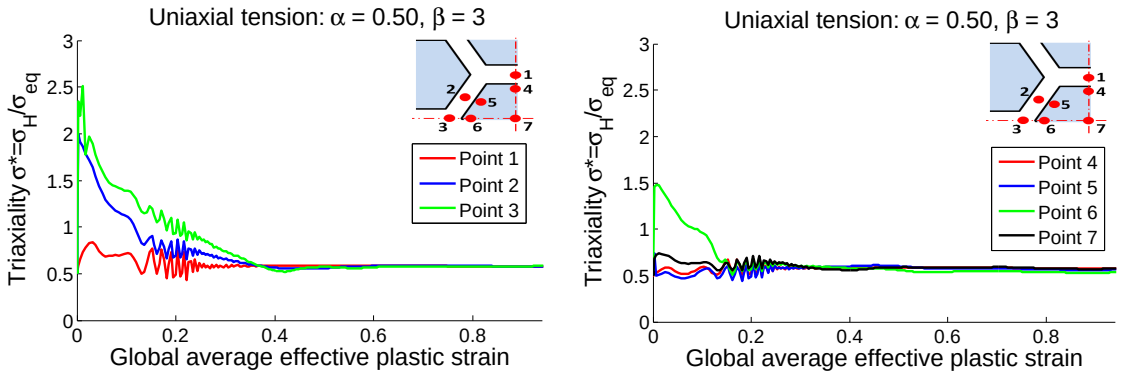

(a) (b)

Figure 6.44: *The stress triaxiality ratio in the sampling points when using isotropic plasticity.*

high negative stress triaxiality ratio. In this case initiation of ductile fracture is unlikely in the horizontal grain boundary.

The stress triaxiality ratio in the sampling points for realization 1 of the crystal plasticity model is shown in figure 6.45. The fluctuations in the result prevent any clear conclusion. However, the stress triaxiality ratio in the points 2 and 3 seems to be higher than the points in the grain interior for low global strains, which is consistent with the results from the isotropic plasticity analyses. The stress triaxiality ratio decreases at global average effective plastic strains of about 0.5-0.15 in the points 2 and 3 and settles at about 0.5-1.5 for higher global average effective plastic strains (> 0.2). This is consistent with what was observed for the isotropic plasticity analyses.

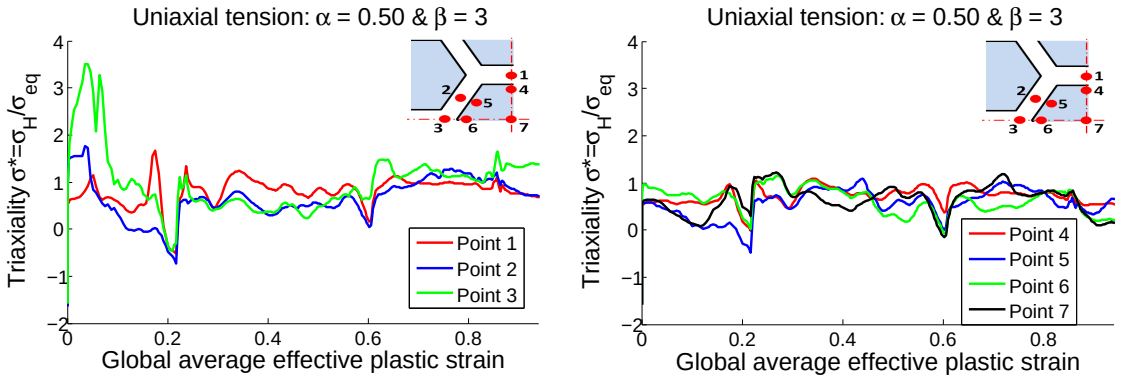

(a) (b)

Figure 6.45: *The stress triaxiality ratio for realization 1 for the model using crystal plasticity.*

6.8 Intergranular versus transgranular fracture

The competition between intergranular and transgranular fracture is dependent on a number of factors. The effect of certain material parameters on the distribution of stresses and strains in a heterogeneous microstructure was investigated in this thesis. In this section, the application of the results from the finite element analysis to the competition between intergranular and transgranular fracture will be discussed.

In this thesis, a simplified model of a microstructure was used to investigate the distribution of stresses and strains. Based on the literature study of the microstructure of aluminium as well as fracture mechanisms, the most important parameters were found to be the effective plastic strain and the stress triaxiality ratio. Three different areas were investigated, namely the effect of yield stress and work hardening rate in the PFZ relative to the grain interior, the effect of global stress triaxiality ratio, and the effect of crystal plasticity.

Failure criterion for intergranular fracture

A model which predicts the failure strain for intergranular fracture based on the area fraction of grain boundary precipitates was developed by Embury *et al.* (1974) [70]. When the area fraction of second phase particles at the grain boundary is low, the plastic strain needed for coalescence of voids initiated from these particles is high. In such cases, the width of the PFZ will influence the strain to failure [70]. When the area fraction of grain boundary precipitates is high, the required plasticity for void coalescence is low and the influence of the width of the PFZ is less [70]. The shear strain to failure was given by:

$$\gamma_f = \frac{1}{2}(f_a^{-1/2} - 1), \tag{6.20}$$

where f_a is the area fraction of grain boundary precipitates. Intergranular fracture will occur by coalescence of the voids initiated from the grain boundary precipitates when the shear strain γ_f reaches a critical value. Although this criterion for fracture is based on the shear strain, it will give a prediction of the critical magnitude of the effective plastic strain. This assumption is based on the fact that both the effective plastic strain and the total shear strain are calculated from the deviatoric part of the stress tensor. Whether this criterion used on effective plastic strain is conservative depends on the stress state.

The relation between the strain to failure at the grain boundary and the area fraction of grain boundary precipitates, is illustrated in figure 6.46.

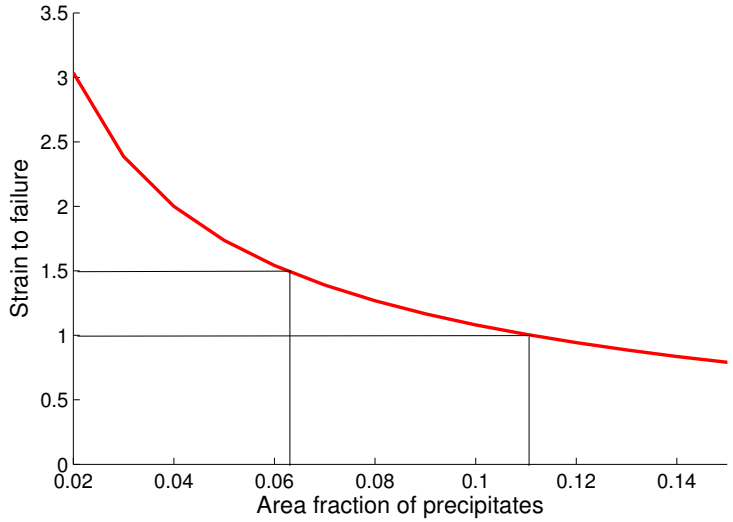

Figure 6.46: *The strain to failure as a function of the area fraction of grain boundary precipitates.*

The effect of yield stress and work hardening rate in the PFZ

The effect of some mechanical properties was investigated through a parameter study, namely the yield stress and the work hardening rate of the PFZ.

The ratio between the yield stress in the PFZ and the grain interior has great influence on the distribution of plastic strains in the model. As the yield stress in the PFZ is increased, the difference between the maximum effective plastic strain in the grain interior and the PFZ decreases. This will favor transgranular fracture, given that the strain to failure in the PFZ is independent of the yield stress. This last assumption is probably not completely true. The strain to failure will probably be reduced when the yield stress is increased, which will favor intergranular fracture. A low yield stress in the PFZ was found to increase the concentration of plastic strain in this zone and make intergranular fracture more likely. This is consistent with the findings of e.g. Embury *et al.* [70], Pardoen *et al.* [3] and Scheyvaerts [35].

For a low yield stress in the PFZ, the center of the grain interior (point 7) experience higher effective plastic strains than the vicinity of the PFZ (points 4, 5 and 6). Investigation of the distribution of effective plastic strain within the grain interior, uncovered that the plastic strain was concentrated along bands oriented at 45° with respect to the external load (see figure 6.23). Since the spread in stress triaxiality ratio within the grain interior is low (see e.g. figure B-7 in appendix B), it is reasonable to assume that transgranular fracture is most likely to occur along the these bands.

Again, assuming that the strain to failure in the PFZ is independent of the yield stress in this zone and due to the high work hardening rate of the PFZ, the material is likely to fail by transgranular fracture when the difference in yield stress in the PFZ and in the grain interior decrease.

When the ratio between the yield stresses (α) is held constant, a low work hardening rate in the PFZ will increase the concentration of plastic strain in this zone, making it more susceptible to void growth. A decreased work hardening rate in the PFZ was also found to increase the maximum effective plastic strain in the grain interior. However, the magnitude of the increase in the grain interior was low compared to the increase in the PFZ. This indicates that intergranular fracture is promoted when the work hardening rate in the PFZ is decreased.

Also, when the work hardening rate in the PFZ was decreased, the average effective plastic strain in this zone increase while the average effective plastic strain in the grain interior experienced a slight decrease (see figure 6.17). The increased average effective plastic strain in the PFZ will make void growth more likely in this zone.

If the properties of the PFZ and the global triaxiality is such that yielding occur in the grain interior before void growth in the PFZ, transgranular fracture is the most likely failure mechanism [3]. This is due to the rapid void growth rate in the age hardened grain interior [35]. Void growth in the PFZ is most likely before the grain interior starts to yield, due to the drop in the stress triaxiality in the PFZ subsequent to yielding in the grain interior [3].

The effect of global stress triaxiality ratio

Figure 6.47 illustrates the effect of the global stress triaxiality on the stress triaxiality distribution within the model. The maximum effective plastic strain in the PFZ at this stage is 0.9 which, using the model of Embury *et al.*, is assumed to be critical for an area fraction of grain boundary precipitates of approximately 1/8.

For the uniaxial tension mode, the stress triaxiality ratio is generally positive (see figure 6.47). The maximum stress triaxiality ratio is located in the slanted PFZ which is also the location of the maximum effective plastic strain. This means that intergranular fracture is most likely to initiate in the slanted PFZ for the uniaxial tension mode.

The stress triaxiality ratio for the biaxial tension mode is generally higher than for the uniaxial tension mode (see figure 6.47). The maximum stress triaxiality ratio is located in the horizontal PFZ. The distribution of effective plastic strain for the biaxial tension mode is similar to the uniaxial tension mode. Then, intergranular fracture may both initiate in the horizontal and in the slanted PFZ for the biaxial tension mode.

The shear mode have generally a negative stress triaxiality ratio which will prevent void growth (see figure 6.47). This is not true for shear in general, but the way it is imposed here will result in negative hydrostatic stress. The magnitude of the stress triaxiality distribution has its peak in the horizontal PFZ, which means that void growth in this PFZ is unlikely.

Pardoen *et al.* [3] argue that a low global stress triaxiality ratio will favor transgranular fracture, as it will allow plasticity to occur in the grain interior before the PFZ fail by void coalescence. This is consistent with the finding in this thesis. For instance, the global stress triaxiality ratio for the uniaxial tension mode is lower than for the biaxial

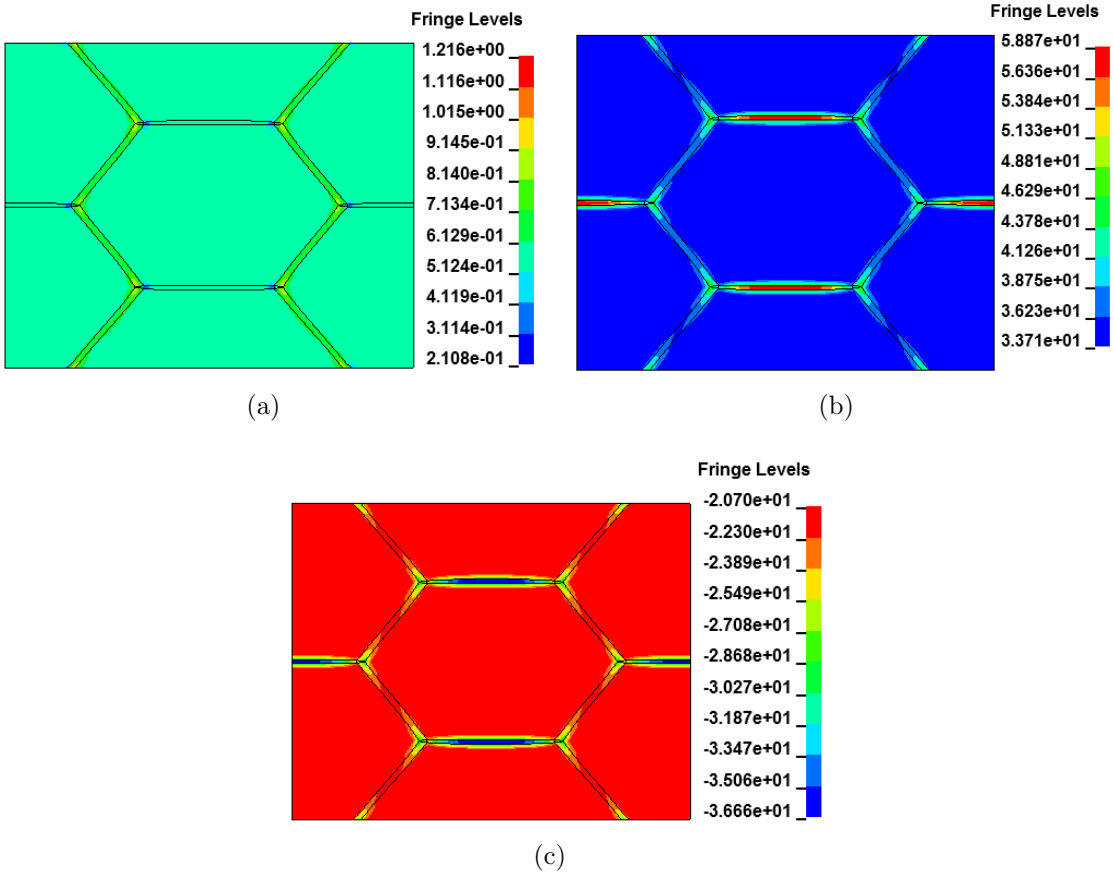

Figure 6.47: *Illustration of the distribution of stress triaxiality ratio for (a) the uniaxial tension mode, (b) the biaxial tension mode and (c) the shear mode. The global average effective plastic strain is 0.35. At this point the maximum effective plastic strain in the PFZ is 0.9. The benchmark material was used.*

tension mode. The stress triaxiality ratio in the PFZ, for the uniaxial tension mode, is generally lower than for the biaxial tension mode (see figure 6.47). At the same time the maximum effective plastic strain in the PFZ was approximately equal for the uniaxial and the biaxial tension mode (see figure 6.14 and 6.16). This means that when loaded in biaxial tension, void growth is more likely to happen in the PFZ before plasticity occur in the grain interior.

The effect of crystal plasticity

Due to the long computational time required to run simulations with the crystal plasticity model, it is of interest to run the simulations with a simpler material model. Isotropic plasticity as presented in this thesis is such a model.

When using isotropic plasticity and crystal plasticity the distributions of stresses and strains were similar. However, due to fluctuations in the some of the results, the validity is uncertain. A more extensive study using a higher number of realizations of the crystal

plasticity model should be carried out in order to validate the results obtained in this thesis.

The stress triaxiality ratio influences the initiation of ductile fracture (see section 4.1) and analysis of the uniaxial tension mode indicated that the stress triaxiality ratio in the sampling points were similar for the two material models. Emphasis will be put on discussing the effective plastic strain, assuming that the distribution of stress triaxiality is approximately equal using both material models. Further, it is assumed in this discussion that the strain to failure is equal regardless of the material model.

With crystal plasticity, the difference between the average effective plastic strain in the grain interior and in the PFZ was generally lower than with isotropic plasticity. This indicates that the isotropic plasticity model will predict intergranular fracture before the crystal plasticity model. However, the literature study of fracture mechanisms uncovered that ductile fracture will initiate at the location where the sum of the hydrostatic stress and the von Mises equivalent stress is highest. As mentioned earlier, the hydrostatic stress is related to the stress triaxiality ratio and the von Mises stress is related to the plastic strain through the associated flow rule. The maximum effective plastic strain is therefore a prediction of initiation of ductile fracture.

For global average effective plastic strains above approximately 0.1, the isotropic plasticity model gave a higher maximum effective plastic strain in the PFZ than the crystal plasticity model. At the same global strain level, the isotropic plasticity model gave a lower maximum effective plastic strain in the grain interior. The maximum effective plastic strain in the PFZ at a global average effective plastic strain of 0.1 is approximately 0.5 regardless of the loading mode. Using the criterion by Embury *et al.* [70] on effective plastic strain, the required area fraction of grain boundary precipitates for initiation of intergranular fracture is approximately 0.7. If the area fraction of grain boundary precipitates is below 0.7, the strain to failure in the PFZ will be higher than 0.5. Assuming that the distribution of stress triaxiality is equal for both material models, the isotropic plasticity model will predict intergranular fracture before the crystal plasticity model, when strain to failure in the PFZ is above 0.5.

For global average effective plastic strains below approximately 0.1, the isotropic plasticity model gave a lower maximum effective plastic strain in the PFZ then the crystal plasticity model. For this low global strain, the maximum effective plastic strain in the grain interior was higher using isotropic plasticity than when using crystal plasticity. With a strain to failure in the PFZ lower than 0.5, the crystal plasticity model will predict intergranular fracture before the isotropic plasticity model.

Several authors have suggested that intergranular fracture is most likely for low plastic strains in the grain interior since the void growth rate is more rapid within the grains (see e.g. Pardoen *et al.* [3] or Scheyvaerts [35]). This means that intergranular fracture is most likely to occur for low global strains. The results obtained in this thesis show that for low global strains, the crystal plasticity model will predict intergranular fracture before the isotropic plasticity model. A more accurate calibration of the crystal plasticity model may influence the results obtained in this thesis.

6.9 Sources of error

The sources of error which are considered to have the most influence on the result are discussed in this section.

For simplicity, both the PFZ and the grain interior were assumed to have an elastic linear plastic material response. The work hardening rate of the PFZ is believed to be higher than of the grain interior, due to pile up of dislocations towards the grain boundary and the PFZ matrix interface. The pile up may be resolved if the stress is sufficient, which indicate that the hardening will saturate quickly compared to the grain interior [39]. Also the density of dislocations in the PFZ will be very high which will increase the annihilation rate, as discussed in section 2.3.8. This means that the assumption of linear plastic response from both the grain interior and the PFZ is probably not physical. A hardening law with a decaying slope might be a better choice. A hardening law accounting for stress saturation in the PFZ would increase the risk of intergranular fracture.

The mesh used in the analyses in this thesis had a uniform element size inside the grain interior. The verification of the mesh did show convergence for the maximum effective plastic strain in the grain interior. However, it would still be interesting to modify the mesh with locally higher density towards the PFZ, in order to capture gradients in a better way.

The material parameters used in this thesis were not calibrated to match any specific alloy. The geometrical dimensions are also not physical. For instance, the width of the PFZ was chosen to be 0.2 mm, although experiments by e.g. Abe *et al.* [39] suggests that the width of the PFZ range from $0.1 - 1$ micron. Whether the PFZ width is important to the distribution of stresses and strains should be investigated. However, some researchers even suggest that the width of the PFZ have minor influence on the fracture toughness (see e.g. Vasudévan *et al.* [71]).

The calibration of the crystal plasticity model was carried out using a single element loaded in uniaxial tension. The results from the crystal plasticity analyses seem to be consistent with the results from the isotropic plasticity analyses. Nonetheless, whether the single element can be regarded representative for the effective properties of multiple elements is uncertain. The sensitivity of the crystal plasticity model to the input parameters should be investigated in order to verify the calibration of this model.

Due to high computational time, only few realizations of the grain orientations were used during the crystal plasticity analyses in this thesis. The number of realizations cannot be considered statistically significant. The distribution of stresses and strains was found to be dependent on the grain orientations. This uncertainty could be resolved by a more extensive study using a higher number of realizations of the crystal plasticity model. Also, the model used in this thesis cannot be considered a representative volume element. In order to be representative for a specific aluminium alloy, the number of grains needs to be higher. Incorporating periodic boundary conditions will make the model more representative.

6.10 Conclusion

Numerical simulations were carried out using a simplified model of a microstructure. A parameter study using an isotropic plasticity material model has been performed. The yield stress and work hardening rate of the PFZ as well as the global stress triaxiality were all variables in the parameter study. The plastic strain within the grains was found to be concentrated in bands at a 45° angle with respect to the external load.

Three different loading modes were tested to see the effect of the global stress triaxiality on the distribution of stresses and strains. The shear mode led to a generally negative stress triaxiality ratio, which counteracts void growth. The uniaxial tension mode gave positive stress triaxiality in the slanted PFZ, which was also the location of the maximum effective plastic strain. This indicates that under uniaxial tension, the slanted PFZ is the most likely location for initiation of intergranular fracture. The biaxial tension mode resulted in higher positive stress triaxiality in the horizontal PFZ than for the uniaxial tension mode. This suggests that under biaxial tension, the horizontal PFZ as well as the slanted PFZ might be candidates for ductile fracture initiation.

When the yield stress and the work hardening rate of the PFZ were increased, the average effective plastic strain decreased in the PFZ and increased in the grain interior. Also, the maximum effective plastic strain in both PFZ and grain interior was found to decrease. The yield stress and the work hardening rate of the PFZ were found to influence the grain interior less than the PFZ. This indicates that increasing the yield stress and the work hardening rate of the PFZ will favor transgranular fracture.

The effect of crystal plasticity on the distribution of stresses and strains was investigated. The results obtained using the current calibration of the crystal plasticity model were found not to contradict the results from the isotropic plasticity model as far as concentration of plastic strain in the PFZ is concerned. However, the crystallographic orientations were found to influence the maximum effective plastic strain both in the PFZ and the grain interior. Using crystal plasticity, the difference in average effective plastic strain between the grain interior and the PFZ was less than when using isotropic plasticity. For global average effective plastic strains below 0.1, the crystal plasticity model gave a larger difference between the maximum effective plastic strain in the grain interior and in the PFZ than the isotropic plasticity model. For global average effective plastic strains above 0.1, the difference in maximum effective plastic strain between the grain interior and the PFZ was lower using crystal plasticity than when using isotropic plasticity.

Fluctuations in the stress triaxiality ratio made it difficult to determine whether the crystal plasticity model influenced the distribution of stress triaxiality. Assuming the distribution of stress triaxiality is equal regardless of the material model, the crystal plasticity model would predict intergranular failure before the isotropic plasticity model for global average effective plastic strains below 0.1. For global average effective plastic strains above 0.1, the crystal plasticity model would favor transgranular fracture compared to the isotropic plasticity model.

Chapter 7

Further work

In this thesis, the distribution of stresses and strains in a heterogeneous microstructure was investigated using fictive material parameters and an idealized geometry. To eliminate the uncertainty regarding the material parameters, a material model should be calibrated against results from experiment. As suggested in section 6.9, the assumption of linear hardening in the PFZ made in this thesis might lead to inaccurate results.

The width of the PFZ used in this thesis was several orders of magnitude wider than what can be observed in a real microstructure using a transition electron microscope. Whether the width of the PFZ is important to the fracture toughness of the material is a topic of discussion. A parameter study of the PFZ width within the range of what is to be expected for an aluminium alloy should be carried out in order to determine whether the PFZ width is important to the fracture behavior.

In an aluminium microstructure, the presence of second phase particles is thought to influence the toughness of the material. In this thesis, the simulations where carried out on a simplified model, including only the age hardened grain interior and the precipitate free zone near the grain boundary. In order to investigate the effect of material faults, a more advanced model should be developed incorporating second phase particles with properties different from the surrounding matrix.

In order to investigate how the material will respond during crack propagation, some form of fracture criterion should be implemented. The cohesive element model and element erosion might be suitable candidates to model ductile fracture in aluminium. It would also be of interest to compare the performance of these two models against experiments.

Bibliography

[1] LS-DYNA Version 971.
Livermore Software Technology Corporation (LSTC) 2011.

[2] LS-INGRID: A Pre-Processor and Three-Dimentional Mesh Generator for the Programs LS-DYNA, LS-NIKE3D and TORAZ3D.
Livermore Software Technology Corporation (LSTC) 1998; Version 3.5.

[3] T. Pardoen, D. Dumont, A. Deschamps and Y. Brechet.
Grain boundary versus transgranular ductile failure.
Journal of the Mechanics and Physics of Solids 2003; Vol. 51: 637-665.

[4] George Ellwood Dieter.
Mechanical Metallurgy, SI Metric Edition.
McGraw-Hill Book Company 1988.

[5] ASM International, Cited 19.05.2012.
`http://www.asminternational.org/content/SubjectGuides/sg˙crystal˙structure˙f04.jpg`

[6] William F. Hosford.
Mechanical behavior of materials.
Cambridge University Press 2005; ISBN-13 978-0-521-84670-7.

[7] Aluminium 1050-O, matweb.com. Cited 10.04.2012.
`http://matweb.com/search/DataSheet.aspx?MatGUID=273c1ffbdc134a8292c704da3ee2ff35&ckck=1`

[8] M. Peach and J.S. Koehler.
The forces exerted on dislocations and the stress fields produced by them.
Physical Review 1950; Vol. 80: 436-439.

[9] Christian-Albrechts-Universität zu Kiel, web page cited 15.05.2012
`http://www.tf.uni-kiel.de/matwis/amat/def˙en/kap˙5/backbone/r5˙2˙5.html`

[10] ASM International, cited 19.05.2012
`http://www.asminternational.org/content/SubjectGuides/sg˙crystal˙structure˙f05.jpg`

[11] R.D. Law, S.M. Schmid and J. Wheeler.
Simple shear deformation and quartz crystallographic fabrics: a possible natural

example from the Torridon area of NW Scotland.
Journal of Structural Geology 1990; Vol. 12: 29-45.

[12] A. Deschamps and Y. Bréchet.
Influence of predeformation on ageing in an Al-Zn-Mg alloy. II. Modelling of precipitation kinetics and yield stress.
Acta Materialia 1999; Vol. 47, No. 1: 293-305.

[13] O. R. Myhr, Ø. Grong and S. J. Andersen.
Modelling of the age hardening behavior of Al-Mg-Si alloys.
Acta Materialia 2001; Vol. 49: 65-75.

[14] F.C. Frank and W.T. Read, Jr.
Multiplication processes for slow moving dislocations.
Physical Review 1950; Vol. 79: 722-723.

[15] A.N. Stroh.
The formation of cracks as a result of plastic flow.
Proceedings of the Royal Society of London A 1953; Vol. 223: 404-414.

[16] Odd Sture Hopperstad.
Lecture notes TKT4135 Mechanics of materials.
NTNU 2011.

[17] HSUN HU.
Texture of metals.
Texture 1974; Vol. 1: 233-258.

[18] J.E. Burke and D. Turnbull.
Recrystallization and grain growth.
Progress in Metal Physics 1952; Vol. 3: 220-244.

[19] E. Hornbogen.
Combined reactions.
Metallurgical and Materials Transactions A 1979; Vol. 10: 947-972.

[20] U.F. Kocks, C.N. Tomé and H.R. Wenk.
Texture and anisotropy: preferred orientations in polycrystals and their effect on materials properties.
Cambridge University Press 1998; ISBN 0 521 46516 8.

[21] I.M. Lifshitz and V.V. Slyozov.
The kinetics of precipitation from supersaturated solid solutions.
Journal of Physics and Chemistry of Solids 1961; Vol. 19: 35-50.

[22] E.O. Hall.
Yield point phenomena in metals and alloys.
Plenum Press, New York 1970.

[23] aluMATTER, cited 04.04.2012.
`http://www.aluminium.matter.org.uk/`

[24] J. Friedel.
Dislocations.
Pergamon Press, Oxford 1964; Vol. 3.

[25] L.P. Kubin, Y. Estrin and C. Perrier.
On static strain ageing.
Acta Metallurgica et Materialia 1992; Vol. 40: 1037-1044.

[26] A.H. Cottrell and B.A. Bilby.
Dislocation theory of yielding and strain ageing of iron.
Proceedings of the Physical society A 1949; Vol. 62: 49-61.

[27] L.P. Kubin and Y. Estrin.
Dynamic strain ageing and the mechanical responce of alloys.
Journal de Physique III 1991; Vol. 1: 929-943.

[28] G. Ananthakrishna.
Current theoretical approaches to collective behavior of dislocations.
Physics Reports 2007; Vol. 440: 113-259.

[29] P.G. McCormigk.
A model for the Portevin-Le Chatelier effect in substitutional alloys.
Acta Metallurgica 1972; Vol. 20, Issue 3: 351-354.

[30] G.R. Love.
Dislocation pipe diffusion.
Acta Metallurgica 1963; Vol. 12: 731-737.

[31] R.C. Picu and D. Zhang.
Atomistic study of pipe diffusion in Al-Mg alloys.
Acta Materialia 2004; Vol. 52, Issue 1: 161-171.

[32] Metal Pass, web page cited 26.05.2012.
`http://www.metalpass.com/metaldoc/paper.aspx?docID=62`

[33] E.F. Morris.
Precipitation hardening of aluminium alloys.
Metallurgical Transactions A 1975; Vol. 6: 625-630.

[34] P.N.T. Unwin, G.W. Lorimer and R.B. Nicholson.
The origin of the grain boundary precipitate free zone.
Acta Metallurgica 1969; Vol. 17: 1379-1393.

[35] Florence Scheyvaerts.
Multiscale modelling of ductile fracture in heterogeneous metallic alloys.
PhD thesis. UCL - FSA/MAPR - Département des sciences des matériaux et des procédés 2009.

[36] Erhard Hornbogen and Michael Gräf.
Fracture toughness of precipitation hardened alloys containing narrow soft zones at grain boundaries.
Acta Metallurgica 1977; Vol. 25: 877-881.

[37] A. Deschamps, S. Esmaeili, W.J. Poole and M. Militzer.
Strain hardening rate in relation to microstructure in precipitation hardening materials.
Journal of physics 2000; Vol. 10: 151-156.

[38] L.M. Cheng, W.J. Poole, J.D. Embury and D.J. Lloyd.
The influence of precipitation on the work-hardening behavior of the aluminium alloys AA6111 and AA7030.
Metallurgical and Materials Transactions A 2003; Vol. 34: 2473-2481.

[39] M. Abe, K. Asano and A. Fujiwara.
Influence of the Precipitate-Free Zone Width on the Tensile Properties of an AI-6 Wt Pct Zn-l.2 Wt Pct Mg Alloy.
Metallurgical Transactions 1973; Vol. 4: 1499-1505.

[40] Ted L. Anderson.
Fracture Mechanics: Fundamentals and Applications, Third Edition.
Taylor & Francis 2005.

[41] Robert D. Cook, David S. Malkus, Michael E. Plesha and Robert J. Witt.
Concepts and applications of finite element analysis.
John Wiley & Sons, Inc. 2001; 4th ed. ISBN 978-0-471-35605-9.

[42] A.S. Argon, J. Im and R. Safoglu.
Cavity formation from inclusions in ductile fracture.
Metallurgical Transactions A 1975; Vol. 6: 825-837.

[43] C. Ruggieti.
Numerical investigation of constraint effects on ductile fracture in tensile specimens.
Journal of the Brazilian Society of Mechanical Sciences and Engineering 2004: Vol. 26: 190-199.

[44] R.H. Van Stone, T.B. Cox, J.R. Low Jr. and J.A. Psioda.
Micostructural aspects of fracture by dimpled rupture.
International Metals Reviews 1985; Vol. 30: 157-179.

[45] F.M. Beremin.
Cavity formation from inclusions in ductile fracture of A508 steel.
Metallurgical Transactions A 1981; Vol. 12: 723-731.

[46] S.H. Goods and L.M. Brown.
The nucleation of cavities by plastic deformation.
Acta Metallurgica 1979; Vol. 27: 1-15.

[47] Nicolas Moës, John Dolbow and Ted Belytschko.
A Finite Element Method for Crack Growth Without Remeshing.
International Journal for Numerical Methods in Engineering 1999; 46:131-150.

[48] Thomas-Peter Fries and Ted Belytschko.
The extended/generalized finite element method: An overview of the method

and its applications.
International Journal for Numerical Methods in Engineering 2010; 84:253-304.

[49] D. S. Dugdale.
Yielding of steel sheets containing slits.
Journal of the Mechanics and Physics of Solids 1960; Vol. 8: 100-104.

[50] A. Hilleborg, M. Modéer and P.E. Petersson.
Analysis of crack formation and crack growth in concrete by means of fracture mechanics and finite elements.
Cement and concrete research 1976; Vol. 6: 773-782.

[51] René de Borst.
Encyclopedia of Computational Mechanics: Damage, Material Instabilities, and Failure.
John Wiley & Sons, Ltd. 2004; ISBN: 0-470-84699-2.

[52] LS-DYNA Support webpage.
`http://www.dynasupport.com/howtos/element/cohesive-element-formulation`

[53] Viggo Tvergaard and John W. Hutchinson.
The relation between crack growth resistance and fracture process parameters in elastic-plastic solids.
Journal of Physics and Chemistry of Solids 1992; Vol. 40: 1377-1397.

[54] Viggo Tvergaard and John W. Hutchinson.
The influence of plasticity on mixed mode interface toughness.
Journal of Physics and Chemistry of Solids 1993; Vol. 41: 1119-1135.

[55] Viggo Tvergaard and John M. Hutchinson.
Toughness of an interface along a thin ductile layer joining elastic solids.
Philosophical Magazine 1994; Vol. 70: 641-656.

[56] Viggo Tvergaard and John W. Hutchinson.
On the toughness of ductile adhesive joints.
Journal of Physics and Chemistry of Solids 1996; Vol. 44: 789-800.

[57] LS-DYNA manual.
LS-DYNA, Keyword user's manual.
Livermore Software Technology Corporation (LSTC) 2007; Version 971: ISBN 0-9778540-2-7.

[58] S. Roy Chowdhury and R. Narasimhan.
A cohesive finite element formulation for modelling fracture and delamination in solids.
Sadhana 2000; Vol. 25, Part 6: 561-587.

[59] M. Elices, G.V. Guinea, J. Gómez and J- Planas.
The cohesive zone model: advantages, limitations and challenges.
Engineering Fracture Mechanics 2002; Vol. 69: 137-163.

[60] G.T. Camacho and M. Ortiz.
Computational modelling of impact damage in brittle materials.
International Journal of Solids and Structures 1996; Vol. 33: 2899-2938.

[61] K.L. Roe and T. Siegmund.
An irreversible cohesive zone model for interface fatigue crack growth simulations.
Engineering Fracture Mechanics 2003; Vol. 70: 209-232.

[62] I. Scheider and W. Brocks.
Simulation of cup-cone fracture using the cohesive model.
Engineering Fracture Mechanics 2003; Vol. 70: 1943-1961.

[63] J.F. Molinari, G. Gazonas, R. Raghupathy, A. Rusinek and F. Zhou.
The cohesive element approach to dynamic fragmentation: The question of energy convergence.
International Journal for Numerical Methods in Engineering 2007; Vol. 69: 484-503.

[64] I.M. Gitman, H. Askes and L.J. Sluys.
Representative volume: Existance and size determination.
Engineering Fracture Meachanics 2007; Vol. 74: 2518-2534.

[65] T. Kanit, S. Forest, I. Galliet, V. Mounoury and D. Jeulin.
Determination of the size of the representative volume element for random composites: statistical and numerical approach.
International Journal of Solids and Structures 2003; Vol. 40: 3647-3679.

[66] Aluminium 2036-T4, matweb.com. Cited 10.04.2012.
`http://matweb.com/search/DataSheet.aspx?MatGUID=c5e76ddf336e46d8b17ec41d5690f7e5`

[67] S. Dumoulin, O.S. Hopperstad and T. Berstad.
Investigation of integration algorithms for rate-dependent crystal plasticity using explicit finite element codes.
Computational Materials Sience 2009; Vol. 46: 785-799.

[68] J.F. Thomas, Jr.
Third-order elastic constants of aluminium.
Physical Review 1968; Vol. 175: 955-962.

[69] LS-DYNA support webpage, cited 31.05.2012.
`http://www.dynasupport.com/howtos/general/effective-plastic-strain`

[70] J.D. Embury and E. Nes.
On the tensile fracture of aluminium alloys.
Zeitschrift für Metallkunde 1974; Vol. 64: 45-55.

[71] A.K. Vasudévan and R.D. Doherty.
Grain boundary ductile fracture in precipitation hardened aluminium alloys.
Acta Metallurgica 1987; Vol. 35: 1193-1219.

Appendices

Appendix A

Geometry

The geometrical dimensions of the model is given in figure A-1. The dimensions are given in [mm].

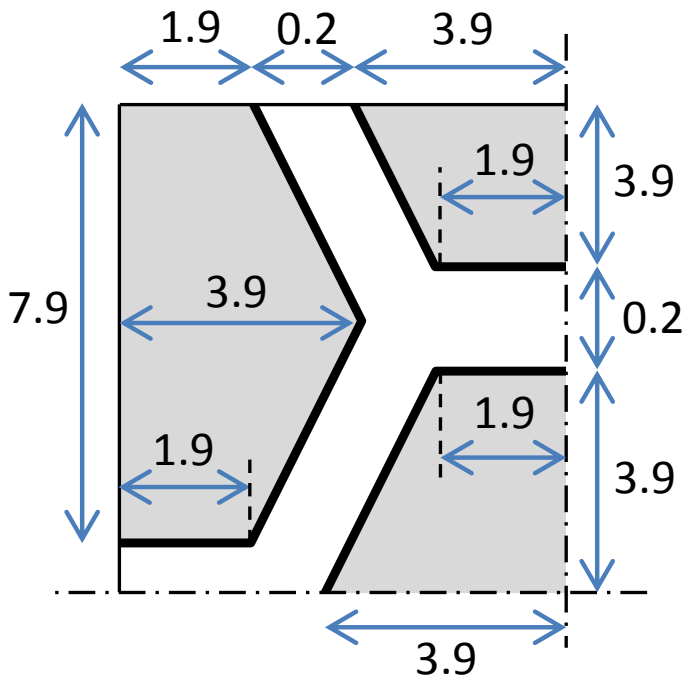

Figure A-1: *The geometrical dimensions of the model. Due to symmetry, only the upper right quarter of the model is shown. The dimensions are given in [mm].*

Appendix B

Results isotropic plasticity, benchmark material

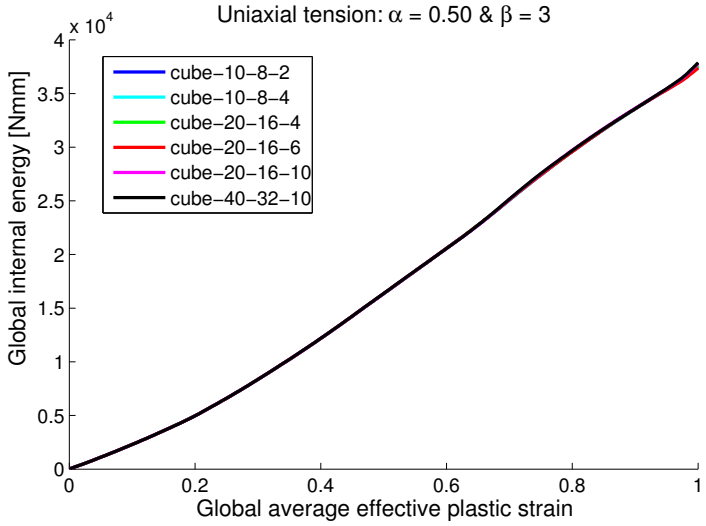

Figure B-1: *Internal energy for the model using isotropic plasticity assigned different meshes. The benchmark material was used and the model was loaded in uniaxial tension.*

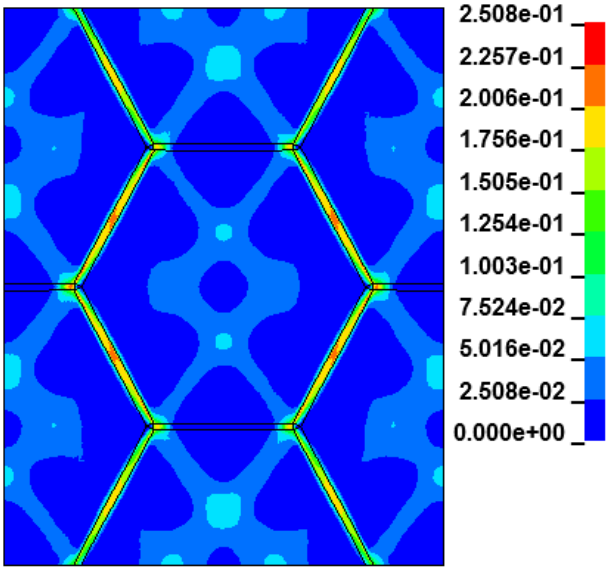

Figure B-2: *Effective plastic strain distribution for the benchmark material loaded in uniaxial tension at a global average effective plastic strain of* 0.04.

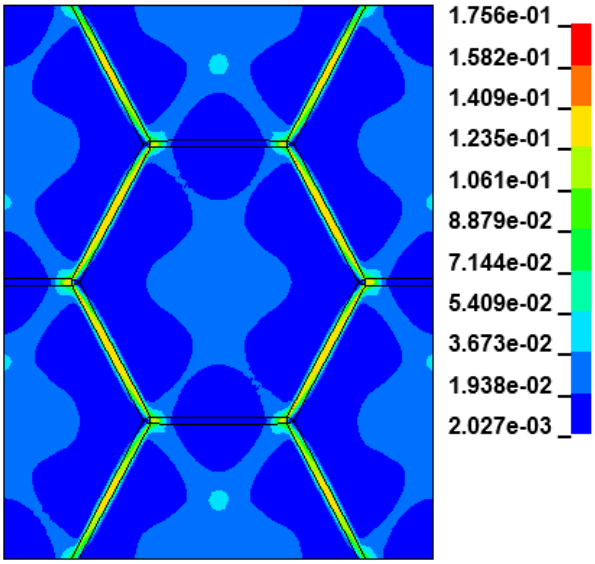

Figure B-3: *Effective plastic strain distribution for the benchmark material loaded in biaxial tension at a global average effective plastic strain of* 0.04.

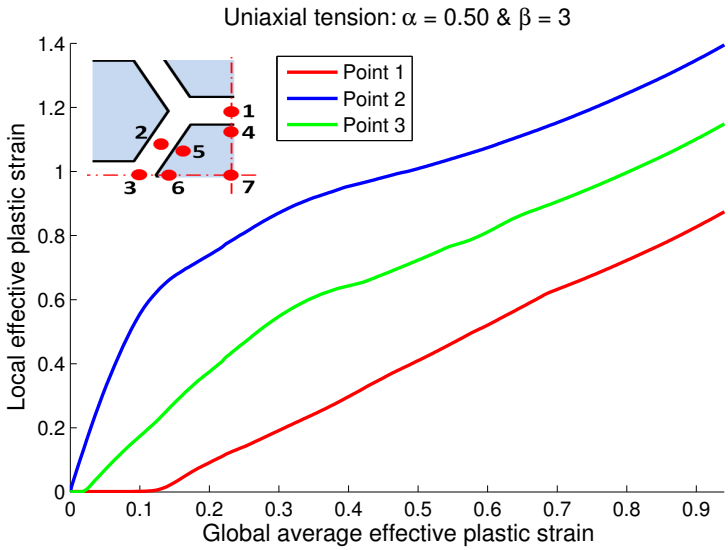

Figure B-4: *Effective plastic strain in points at the grain boundary for the isotropic plasticity model with benchmark material loaded in uniaxial tension.*

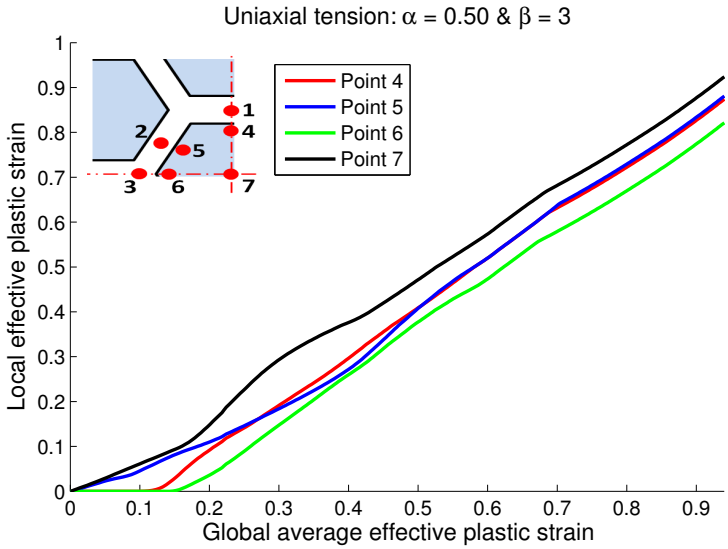

Figure B-5: *Effective plastic strain at points in the grain interior for the isotropic plasticity model with benchmark material loaded in uniaxial tension.*

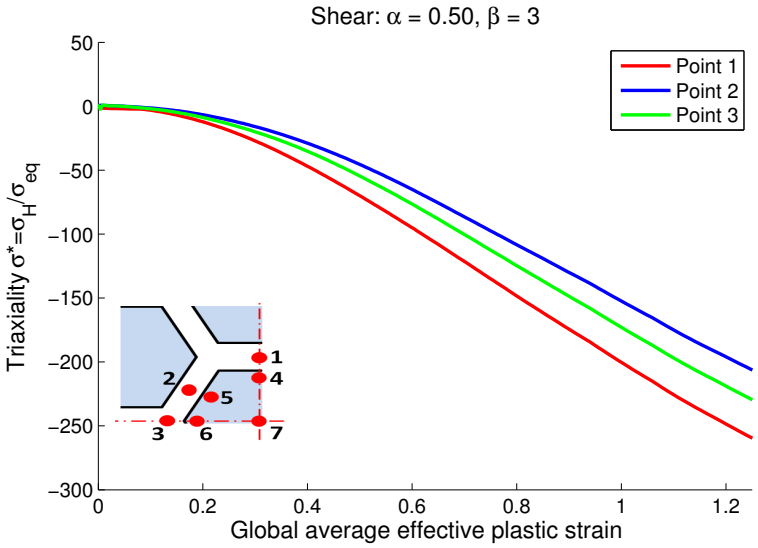

Figure B-6: *The stress triaxiality ratio in the sampling points at the grain boundary. The benchmark material is used and the model is loaded in shear.*

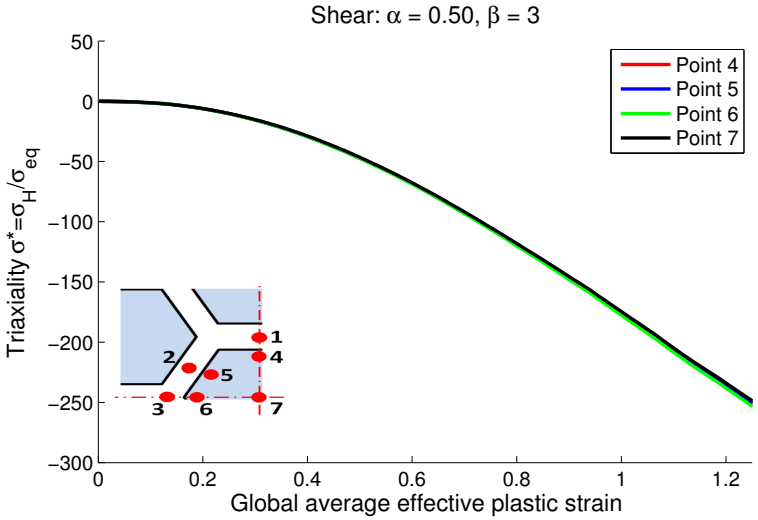

Figure B-7: *The stress triaxiality ratio in the sampling points in the grain interior. The benchmark material is used and the model is loaded in shear.*

Appendix C

Results crystal plasticity

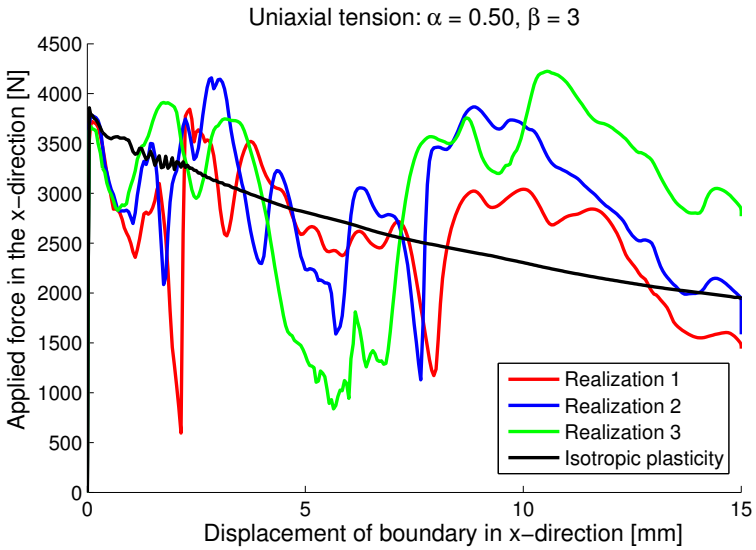

Figure C-1: *Force displacement curve for uniaxial tension and benchmark material. Comparison between the isotropic plasticity model and the crystal plasticity model.*

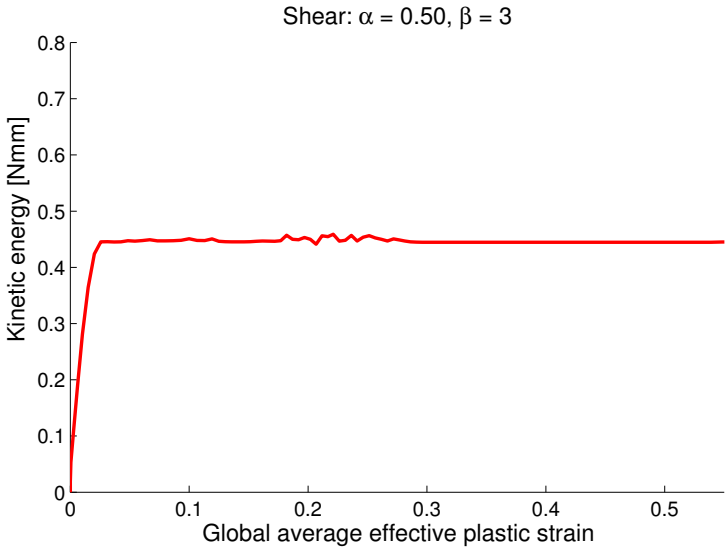

Figure C-2: *Kinetic energy for realization 1 of the model using crystal plasticity loaded in shear. Little to no oscillations is observed before the analysis fail at a global average effective plastic strain of 0.55. The reason for the failure might be the high pressure which is in the order of* $-2 \cdot 10^4 MPa$.

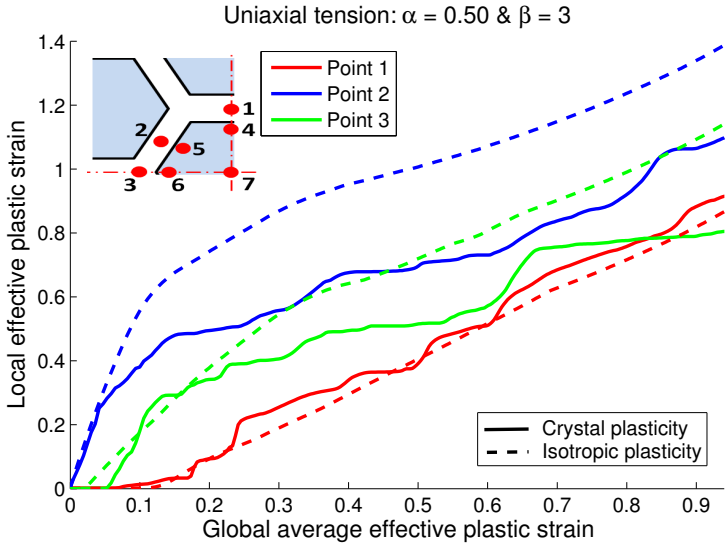

Figure C-3: *Comparison between the effective plastic strain in points at grain boundary for crystal plasticity realization 2 and isotropic plasticity.*

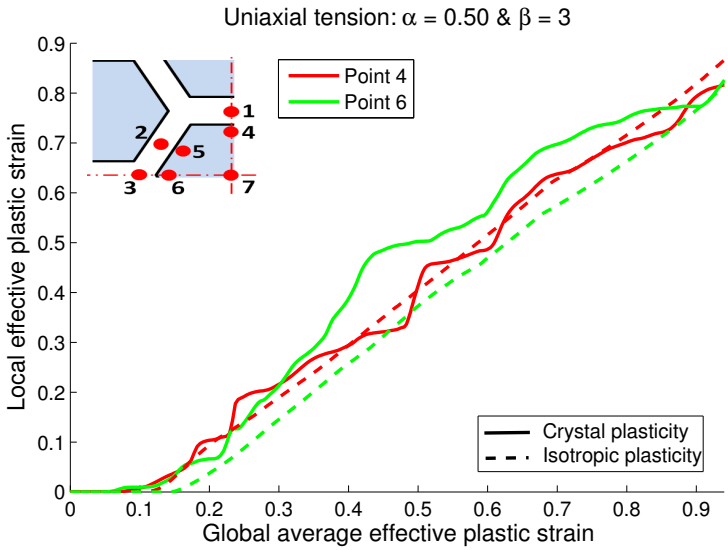

Figure C-4: *Comparison between the effective plastic strain at point 4 and 6 for crystal plasticity realization 2 and isotropic plasticity.*

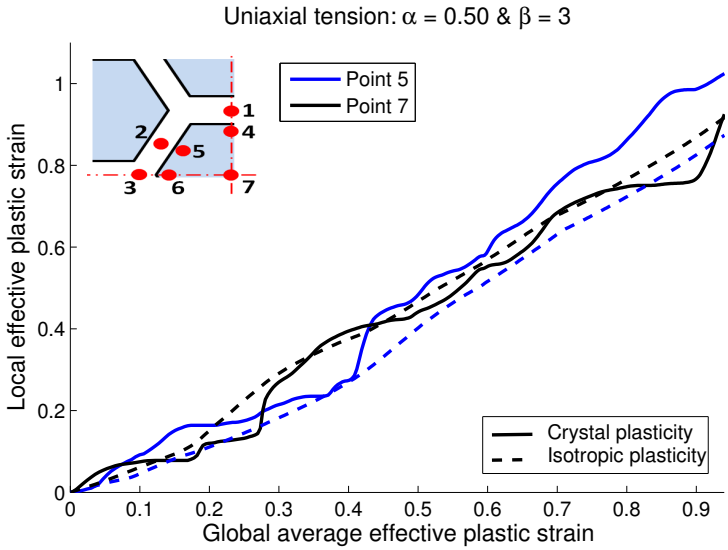

Figure C-5: *Comparison between the effective plastic strain at point 5 and 7 for crystal plasticity realization 2 and isotropic plasticity.*

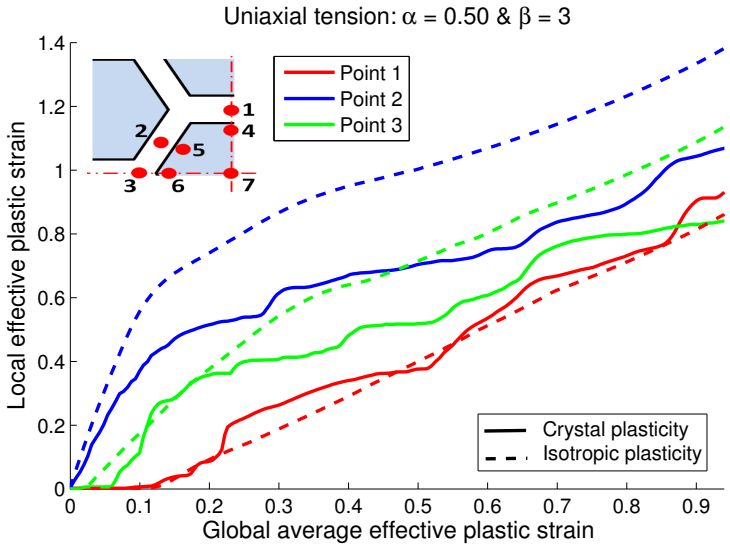

Figure C-6: *Comparison between the effective plastic strain in points at grain boundary for crystal plasticity realization 3 and isotropic plasticity.*

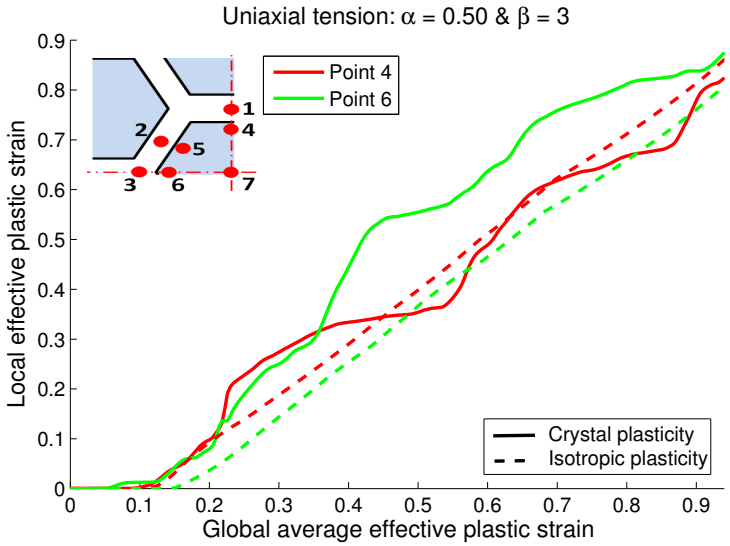

Figure C-7: *Comparison between the effective plastic strain at point 4 and 6 for crystal plasticity realization 3 and isotropic plasticity.*

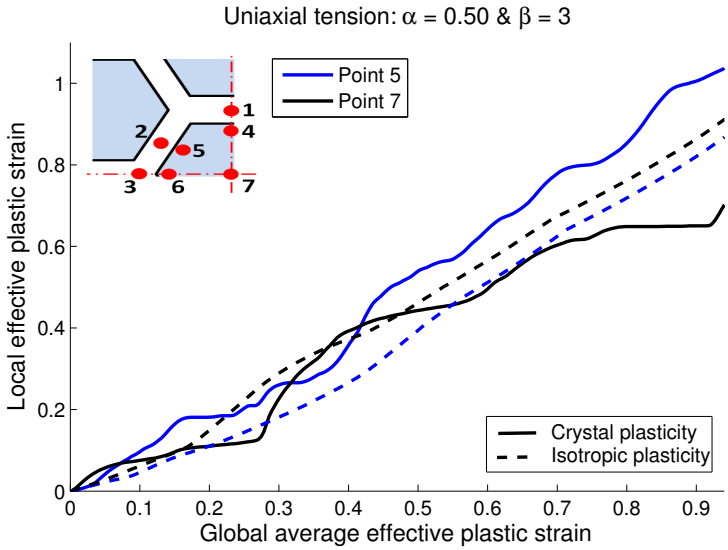

Figure C-8: *Comparison between the effective plastic strain at point 5 and 7 for crystal plasticity realization 3 and isotropic plasticity.*

Appendix D

Time consumtion

Information about the required CPU time for uniaxial tension mode using the mesh `cube-20-16-6` and isotropic plasticity is shown below. Note that total CPU time is 1 hour 44 minutes 29 seconds.

```
Timing information
                        CPU(seconds)    %CPU   Clock(seconds) %Clock
 ------------------------------------------------------------------------
 Initialization ....... 1.2051E-01     0.00      1.9604E-01     0.00
 Element processing ... 6.2228E+03    99.27      7.2591E+03    99.13
 Binary databases ..... 6.0394E+00     0.10      1.2687E+01     0.17
 ASCII database ....... 5.1241E+00     0.08      5.1336E+00     0.07
 Contact algorithm .... 2.2140E+01     0.35      3.2158E+01     0.44
 Contact entities ..... 0.0000E+00     0.00      0.0000E+00     0.00
 Rigid bodies ......... 1.2308E+01     0.20      1.3750E+01     0.19
 Implicit Nonlinear ... 0.0000E+00     0.00      0.0000E+00     0.00
 Implicit Lin. Alg. ... 0.0000E+00     0.00      0.0000E+00     0.00
 ------------------------------------------------------------------------
 Totals                 6.2685E+03   100.00      7.3230E+03   100.00

 Problem time       =    3.2000E+02
 Problem cycle      =   5281147
 Total CPU time     =      6269 seconds (   1 hours 44 minutes 29 seconds)
CPU time per zone cycle  =       175 nanoseconds
 Clock time per zone cycle=       204 nanoseconds

 Number of CPU's     1
 NLQ used/max      384/  384
 Start time    04/25/2012 13:18:26
 End time      04/25/2012 15:25:50
 Elapsed time    7644 seconds( 2 hours  7 min. 24 sec.) for 5281147 cycles

 Normal    termination
```

Information about the required CPU time for uniaxial tension using the mesh `cube-20-16-6` and crystal plasticity plasticity is shown below. Note that the total CPU time is 151 hours 45 minutes 27 seconds.

```
Timing information
                        CPU(seconds)    %CPU  Clock(seconds) %Clock
 ------------------------------------------------------------------
 Initialization ....... 5.2000E-01     0.00     1.7063E-01     0.00
 Element processing ... 5.4528E+05    99.81     1.3634E+05    99.81
 Binary databases ..... 1.2569E+02     0.02     3.2913E+01     0.02
 ASCII database ....... 7.4803E+01     0.01     1.9136E+01     0.01
 Contact algorithm .... 3.6721E+02     0.07     9.2371E+01     0.07
 Contact entities ..... 0.0000E+00     0.00     0.0000E+00     0.00
 Rigid bodies ......... 4.8018E+02     0.09     1.2097E+02     0.09
 Implicit Nonlinear ... 0.0000E+00     0.00     0.0000E+00     0.00
 Implicit Lin. Alg. ... 0.0000E+00     0.00     0.0000E+00     0.00
 ------------------------------------------------------------------
 Totals                 5.4633E+05   100.00     1.3661E+05   100.00

 Problem time       =    3.8000E+02
 Problem cycle      =  18995149
 Total CPU time     =    546327 seconds ( 151 hours 45 minutes 27 seconds)
CPU time per zone cycle  =      4248 nanoseconds
 Clock time per zone cycle=      1062 nanoseconds

 Number of CPU's    4
 NLQ used/max     136/  136
 Start time   05/08/2012 14:50:11
 End time     05/10/2012 04:47:00
 Elapsed time 136609 seconds(37 hours 56 min. 49 sec.) for18995149 cycles

 Normal    termination
```